Basal thermal state of the Greenland Ice Sheet

Soroush Rezvanbehbahani

B.S. Civil Engineering, Sharif University of Technology, Tehran, Iran, 2010

M.S. Geology, The State University of New York at Buffalo, 2013

Submitted to the graduate degree program in Department of Geology and the Graduate Faculty of the University of Kansas in partial fulfillment of the requirements for the degree of Doctor of Philosophy.

Committee members

Leigh A Stearns, Chair

CJ van der Veen, Co-Chair

Randy Stotler

George Tsoflias

J Douglas Walker

Nathaniel Brunsell

Date defended: December 3rd, 2018

The Dissertation Committee for Soroush Rezvanbehbahani
certifies
that this is the approved version of the following dissertation :

Basal thermal state of the Greenland Ice Sheet

Leigh A Stearns, Chair

Date approved: December 3rd, 2018

Abstract

Understanding the basal thermal state of the Greenland Ice Sheet (GrIS) has important implications for modeling its ongoing contribution to global sea level. Apart from removing paleoclimate information from basal layers, basal melt affects the friction at the ice-bedrock interface which has important consequences in terms of ice discharge to the surrounding oceans. The basal thermal state of the GrIS, however, is poorly constrained by observations. The paucity of information is mostly due to expensive and logistically complicated deep-ice drilling campaigns. As a result, only a handful of deep ice cores are available in the entire GrIS. Because of the significance of the basal thermal condition of the GrIS and the difficulties associated with obtaining direct observations from the bed, there is a need for reliable numerical modeling studies, as well as remote sensing techniques.

Perhaps the most important, yet least-known, thermal boundary condition for modeling the basal temperature of the GrIS is the spatial distribution of geothermal heat flux (GHF) beneath the ice. Several models have aimed at estimating the GHF distribution in Greenland. However, the majority of these GHF models sharply contradict each other and cannot reproduce the temperature measurements at ice cores, when implemented in numerical ice sheet models.

This research improves our understanding of the basal thermal condition of the GrIS from three perspectives. First, it reveals the shortcomings of an analytical temperature solution for ice sheets that has been frequently used since the 1950s, and proposes a new solution to resolve the old solution's shortcomings. Second, in contrast with other GHF maps, this study derives a new GHF map for Greenland that honors

geologic and geophysical properties, as well as ice core information. And finally, this study aims at reconciling remotely-sensed observations of basal water with the current GHF models in Greenland.

To Ali-Kazem Behbahani (1925-2017).

The greatest source of inspiration and a mentor who never stopped learning.

Acknowledgements

It is natural that after about six years, some key acknowledgements may elude me. This section acknowledges a small subset of all who have helped me grow as a scientist, as well as a person, over the course of this dissertation.

First and foremost, I could not have asked for a better advisor than Leigh Stearns; She gave me the freedom and courage to explore different directions and approaches in glaciology, and was always equipped with thoughtful criticism, mentorship, and guidance. Yet, she was always there to re-direct and guide me at my times of confusion. Coming from an engineering background, I did struggle with geologic thinking and 'asking the right questions'. She taught me how to think like a scientist, how to hypothesize, and how to be question-driven in my research.

I cannot thank my co-advisor Kees van der Veen enough. With his unquestionable dominance in the field of glaciology, as well as his brutal scientific integrity and intellect, Kees and his 'Bible' (*Fundamentals of Glacier Dynamics*) kept me sincere, responsible, yet excited about problem-solving. I never left Kees's office without learning something new. Both Leigh and Kees have been, and will continue to be great friends from whom I will always learn new things.

I am grateful to Doug Walker who was always there to help me with my general novice geology questions. My other committee members, George Tsoflias, Randy Stotler, and Nate Brunsell were a great asset during my PhD at KU. Their comments and criticism as scientists 'outside' glaciology helped me expand the general implications and usefulness of my research. I also would like to thank Ross Black who walked me through basic steps of inverse modeling in the beginning of my PhD.

Outside the Geology Department at KU, Gordon Oswald from University of Maine helped me understand radar systems, and Ralf Greve from Hokkaido University in Japan got me started on the numerical ice sheet modeling. I am thankful for all the time and energy they spent reading my long emails or Skyping with me.

I greatly benefited from "a mathematician's perspective" by talking to Amir Kadivar from McGill University, and anytime I needed guidance on computational problems, Ramiar Sadegh-Vaziri's simplistic approach (at KTH in Sweden) helped me tackle the problems much more efficiently. I would like to thank my friends at KU, Ben, Jason, Trevor, Ashley, Clay, Brock, Mackenzie, Alexa, Matt, Ty, and Andy (to name a few) who created a pleasant and fun atmosphere throughout the years. Special thanks to my officemates, Sid, Sarah, Logan, Steve, and Konstantinos who tolerated me in my grumpy days.

I cannot pay enough gratitude to my family; my late grandfather Ali-Kazem, my parents Ardeshir and Azadeh, and my brother Siavosh, who were there to support me throughout my entire life, and under all circumstances. At times of relative stability and peace, it is hard to fathom what my parents' generation in Iran endured during the eight-year long war, to keep us safe and provide the necessary needs to learn and grow.

And it goes without saying that all this work wouldn't have been possible without a never-ending and unconditional support from my partner and best friend, Rana. I am aware that I can be unbearable when I am trying to focus or code or read; her patience and support for me is truly admirable and I genuinely appreciate it. She has been, and continues to be, a great source of love and passion and an incredible inspiration for courage and hard work. I cannot be more thankful for having her in my life.

This last one is somewhat odd. Sadly he has been long dead, but Marcel Proust's never-ending novel, *In Search of Lost Time*, has been an unusual source of encouragement. With his meticulous and sometimes annoyingly pedantic vision, Proust revered

the smallest, and perhaps most elusive beauties of life, which would have otherwise been obscured to me.

Finally, acknowledgements for every chapter are as follows:

Chapter 2: An improved analytical solution for the temperature profile of ice sheets

S.R. acknowledges the support by the NSF grant ANT1255488, C.J.V. was supported by the NSF grant ANT1543530, and L.A.S. was supported by the NSF grant ANT1255488. We acknowledge the comments by editor in chief Brynn Hubbard and two anonymous reviewers who substantially criticized and improved the manuscript. All the codes developed for this study are available at `https://bitbucket.org/soroushr/robin_solution`.

Chapter 3: Predicting the geothermal heat flux in Greenland: a Machine Learning approach

This work benefited from numerous discussions with Siavosh R. Behbahani. The published article is co-authored with Amir Kadivar and Douglas J Walker. The codes and data used in this study are publicly available through `https://github.com/amirkdv/ghf-greenland-gbrt`.

Chapter 4: Constraining the geothermal heat flux in Greenland: comparing ice cores, radar observation, and numerical models

Thomas Jordan generously provided the data for basal thaw detection. We thank Michiel van den Broeke for the RACMO2 dataset. S.R. was supported by the NSF grant ANT0424589, L.A.S. was supported by the NASA grant NNX10AP05G, and C.J.V. was supported by the NSF grant ARC0909422. This manuscript is co-authored with Gordon Oswald and Ralf Greve.

Contents

1 Introduction **1**

1.1 Greenland Ice Sheet and sea level 1

1.2 Greenland mass loss components 2

1.3 Significance of ice temperature 3

1.4 Significance of geothermal heat flux (GHF) 4

1.5 Dissertation objectives 5

1.6 Dissertation outline 5

1.6.1 **Chapter 2: An improved analytical solution for the temperature profile of ice sheets** 6

1.6.2 **Chapter 3: Predicting the geothermal heat flux in Greenland: a Machine Learning approach** 6

1.6.3 **Chapter 4: Constraining the geothermal heat flux in Greenland: comparing ice cores, radar observation, and numerical models** 7

1.6.4 **Chapter 5: Summary and conclusion** 7

1.6.5 **Appendix A: Supplementary Information for Chapter 3** 7

2 An improved analytical solution for the temperature profile of ice sheets **8**

2.1 Introduction 10

2.2 One-dimensional models 11

2.2.1 Accuracy of Robin's analytical solution 13

2.2.2 New analytical temperature solution 14

2.2.3 Finding γ_+ 18

2.3 Effect of strain heating 19

2.4 Effect of horizontal advection . . . 23
2.5 Discussion . . . 29
2.6 Conclusion . . . 35

3 Predicting the geothermal heat flux in Greenland: a Machine Learning approach 36
3.1 Introduction . . . 38
3.2 Data . . . 39
3.2.1 GHF measurements: global dataset . . . 39
3.2.2 GHF measurements: Greenland . . . 39
3.2.3 Geologic Features . . . 41
3.3 Method . . . 41
3.3.1 Overview of Statistical Models . . . 41
3.3.2 GHF prediction performance of GBRT . . . 42
3.3.3 GHF prediction with limited local data . . . 43
3.3.4 GHF points for Greenland . . . 47
3.4 Results and Discussion . . . 48
3.4.1 GHF prediction for Greenland . . . 48
3.4.2 Interpretation of GBRT predictions . . . 50
3.5 Conclusion . . . 51

4 Constraining the geothermal heat flux in Greenland: comparing ice cores, radar observation, and numerical models 52
4.1 Introduction . . . 54
4.2 Data and Methodology . . . 58
4.2.1 Ice sheet model . . . 58
4.2.1.1 Thermal model . . . 58
4.2.1.2 Paleoclimate set-up . . . 61
4.2.2 Datasets for radar-detected basal thaw . . . 61

4.2.3 GHF adjustment and simulation setup . . . 63
4.3 Results . . . 65
4.3.1 GHF_{pmp} at Oswald et al. (2018) thawed points . . . 66
4.3.2 GHF_{pmp} at Jordan et al. (2018) thawed points . . . 69
4.3.3 Simplified sensitivity analysis . . . 69
4.3.4 Comparing GHF_{pmp} vs. GHF models . . . 72
4.4 Discussion . . . 76
4.4.1 General discussion . . . 76
4.4.2 Catchment-wide $\dot{M}_b$ estimates . . . 79
4.4.3 Modeling shortcomings . . . 80
4.5 Conclusion . . . 81

5 Concluding Remarks and Future Work **83**
5.1 Summary . . . 83
5.2 Future Work . . . 85

A Supplementary Information for Chapter 3 **103**
A.1 Model Description . . . 103
A.1.1 Problem Setting . . . 103
A.1.2 Regression Trees . . . 104
A.1.3 Boosted Regression . . . 106
A.1.4 Controlling for Overfitting . . . 108
A.1.5 Regularization . . . 109
A.1.6 Stability . . . 109
A.2 Evaluation of GHF Predictions with Limited Local Data . . . 111
A.2.1 Evaluation of Prediction Error . . . 111
A.2.2 Evaluation of Stability . . . 112
A.3 Interpretation and Feature Importances . . . 114

A.3.1 Relative feature importances 115
A.3.2 Further work 115
A.4 Data 118
A.4.1 Distribution of global GHF measurements 118
A.4.2 Available GHF measurements in Greenland 119
A.4.3 Rock type conversions 119

List of Figures

2.1 Linear and SIA-derived vertical velocity profiles and their corresponding temperature profiles from using the Robin and numerical solution, respectively 13

2.2 Parameterization of vertical velocity with different exponents and the resultant temperature profiles 18

2.3 Dependence of γ_+ on vertical *Pe*. 20

2.4 Examining different methods for including the strain heating. 24

2.5 Effect of strain heating on the basal temperature of an ice column with varying ice thickness and rate factors. 25

2.6 Difference between the analytical solution and the full 2D solution ($T_{analytical} - T_{numerical}$) for a Vialov profile with different $\dot{M}$ values. 28

2.7 Difference between the analytical solution and the full 2D solution ($T_{analytical} - T_{numerical}$) for a Vialov profile with different surface temperature lapse rates. 29

2.8 The basal temperature difference between the analytical solution and 2D numerical solution as a function of surface temperature lapse rate. 30

2.9 Difference between basal and surface temperature ($T_b - T_s$) from the analytical solution (equation 2.18) with respect to surface mass-balance rate. 32

2.10 Spatial extent of applicability of the new solution in Greenland and Antarctica. . . 34

3.1 Comparing the performance of Gradient Boosted Regression Tree (GBRT) and linear regression for a random distribution of validation samples. 43

3.2 Step-wise improvement of GBRT predictions with increasing ρ_{ROI} shown over an arbitrary ROI of radius 1300 km. 46

3.3 Normalized RMSE and r^2 of linear correlation for GBRT, linear regression, and constant predictor for different densities. 47
3.4 GHF predictions of GBRT for Greenland. 49

4.1 The GHF maps that are used in this study. 56
4.2 Time series for the temperature anomaly (ΔT) used in paleoclimate runs. 62
4.3 Spatial distribution of radar-detected basal water from Oswald et al. (2018) and Jordan et al. (2018) datasets. 64
4.4 Estimating GHF_{pmp} at locations of basal thaw provided by Oswald et al. (2018) using five different GHF maps and the resultant elevation and surface velocity offset after GHF iterations with respect to the initial geometry. 68
4.5 Estimating GHF_{pmp} at locations of basal thaw provided by Jordan et al. (2018) using five different GHF maps and the resultant elevation and surface velocity offset after GHF iterations with respect to the initial geometry. 71
4.6 Sensitivity of GHF_{pmp} to surface temperature, surface mass balance, and ice thickness using a 1D analytical solution. 73
4.7 Comparing the GHF constraints at thawed points of (a) OSW and (b) JOR with respect to magnetically-inferred GHF of Fox Maule et al. (2009). 74
4.8 Comparing the GHF constraints at thawed points of (a) OSW and (b) JOR with respect to GHF of Martos et al. (2018). 75
4.9 Comparing the GHF constraints at thawed points of (a) OSW and (b) JOR with respect to machine learning-derived GHF of Rezvanbehbahani et al. (2017). 75
4.10 Comparing the GHF constraints at thawed points of (a) OSW and (b) JOR with respect to seismically-inferred GHF of Shapiro & Ritzwoller (2004). 76

A.1 Schematic depiction of a one dimensional regression tree. 105
A.2 Testing the possibility of overfitting by GBRT. 110

A.3 Performance of GBRT, linear regression, and constant predictor for different values of ROI radius. 112
A.4 Sensitivity of GBRT and linear regression to perturbations in training GHF. 114
A.5 Relative importance of different features in the trained GHF prediction model. . . . 116
A.6 Spatial distribution of global GHF point measurements with the corresponding histogram. 117
A.7 Location and magnitude of the prescribed GHF values in Greenland that are included in the training set. 118

List of Tables

2.1 Symbols, values, and units. 12

3.1 Geologic datasets included in the feature vector for predicting GHF. 40

4.1 Basal melt rate in $km^3\ yr^{-1}$ for individual catchments of the GrIS. 80

A.1 GHF measurements or inferences in Greenland. 119

A.2 Conversion of Hartmann & Moosdorf (2012) lithology to general rock type. 120

A.3 Conversion of Dawes (2009) suggested Greenland geologic provinces to general rock type. 120

Chapter 1

Introduction

1.1 Greenland Ice Sheet and sea level

The Greenland Ice Sheet (GrIS) contains enough ice to raise eustatic sea level by about 7 meters if entirely melted (Bamber et al., 2013). Complete collapse of the GrIS, despite having occurred over geologic time-scales, is not anticipated in the near-future. However, continuous mass loss from GrIS to its peripheral oceans will have numerous negative socio-economic ramifications. Increase in global sea level will inundate low-lying lands and island nations (such as Haiti and the Maldives Islands). Given that nearly 10% of the world's population lives near coastal areas, sea level rise and associated storm surges will have undeniable social and economic impacts for all countries. In addition, a significant portion of energy infrastructure is in coastal areas, making the global economic system extremely susceptible to sea level changes. In order for policy-makers to develop effective mitigation and adaptation strategies, polar scientists must provide robust insights on timing and magnitude of the future changes in ice sheets, as an integral component of the global sea level budget.

During the 1991-2015 period, the GrIS contributed an average of $\sim$0.47$\pm$0.23 mm yr^{-1} to sea level rise (Van den Broeke et al., 2016). However, gravity measurements (Harig & Simons, 2016), as well as mass-budget estimates (Van den Broeke et al., 2016) show that since 2012-2013, the near-steady trend of mass loss from Greenland has significantly increased, leading to an accelerated trend of mass loss of $\sim 25.4 \pm 1.2$ Gt yr^{-2} over the last decade (Velicogna et al., 2014). The measured ice loss is commonly attributed to the warming climate and complex feedback mechanisms through which ice sheets respond to temperature changes. However, in order to accurately

predict the future contribution of the GrIS to global sea levels, it is necessary to properly investigate and understand how the ice sheet behaves in a changing climate.

1.2 Greenland mass loss components

In a broad sense, mass loss from the GrIS can be decomposed into two main components. The first component is related to the direct melting at the surface of the ice sheet. It is measured as the difference between total accumulation and net ablation on the ice sheet. This component is controlled by atmospheric forcings and has been relatively well constrained by direct observations (e.g. Fausto et al., 2009), modeling efforts (e.g. Fettweis et al., 2013), and reanalysis studies that combine direct measurements and modelling studies (e.g. Ettema et al., 2010). If the net mass loss due to surface melting is greater than net mass gain (due to snow accumulation), this component will be negative.

The second component of mass loss is due to the dynamic behavior of ice in response to perturbations. Essentially, this component encompasses all the mechanisms that alter the flow characteristics of the ice sheet and affect the direct discharge rate of ice to the surrounding ocean. For example, an increase in ice temperature leads to softer and more deformable ice which results in increased deformational ice velocities. Additionally, when basal melt occurs, the resulting melt-water may lower the traction between ice and the underlying bedrock, which leads to enhanced sliding speeds.

In Greenland, the contribution of these two components to the total mass loss has been nearly equal in the recent years (Enderlin et al., 2014; Csathó et al., 2014). However, there are major shortcomings in our current understanding of the dynamic behavior of glacier ice. These shortcomings have been the major field of investigation in glaciology in the past decade, since the 4th Assessment Report (AR4) of the Intergovernmental Panel on Climate Change (IPCC, Solomon et al., 2007), and they remain the main source of uncertainty in our current estimates of future sea level changes (e.g. Bindschadler et al., 2013). Despite the recent improvements in understanding the processes of ice dynamics changes, our efforts are often hindered by difficulties in making

direct observations and measurements of the subglacial environment.

1.3 Significance of ice temperature

Glacier ice is often modelled as an incompressible thermoviscoelastic fluid (Nye, 1952). That is, it behaves as a fluid with rheologic properties that strongly depend on its temperature. According to Glen's constitutive law for glacier ice (Glen, 1955), the effective stress (τ_e) and effective strain rate ($\dot{\varepsilon}_e$) are related as

$$\dot{\varepsilon}_e = A(T)\tau_e{}^n, \tag{1.1}$$

where $A(T)$ is a temperature-dependent creep rate factor and n is Glen's flow law exponent, often chosen as 3. Based on laboratory experiments, the creep rate factor of glacier ice varies by about 3 orders of magnitude between temperatures of -50 to -5°C (Hooke, 1981; Van der Veen, 2013, section 2.2), with warmer ice being more deformable. Therefore, accurate estimates of ice temperature are important for obtaining reliable numerical ice sheet models.

Apart from the temperature of the upper ice layers, basal temperature is of particular importance in order to understand and simulate subglacial processes. If the basal temperature exceeds the pressure melting temperature, ice will melt and the resulting basal water can impact sliding over the ice-bed interface (Iken & Bindschadler, 1986; Bell et al., 2007). In addition, melting at the basal layers removes the paleoclimate record from the bottom layers. Therefore, identifying regions with frozen bed in the interior of ice sheets is important for potential sites of future ice cores (e.g. Van Liefferinge & Pattyn, 2013; Van Liefferinge et al., 2018). Making direct measurements, however, are extremely difficult and logistically expensive. Due to such difficulties, numerical and analytical models are critical to obtain information about the basal thermal condition of ice sheets (e.g. Robin, 1955; Greve & Hutter, 1995).

1.4 Significance of geothermal heat flux (GHF)

In order to model the basal thermal state of the ice sheets, it is crucial to know the heat sources at the bed. The main heat sources are strain heating, GHF, and frictional heating when basal sliding occurs. Among these heat sources at the bed, GHF is the least constrained by measurements. The effects of spatial variations of GHF on ice sheet dynamics have been investigated by numerical ice sheet models. Larour et al. (2012a) evaluate the uncertainties in GHF models for Pine Island Glacier in West Antarctica, and show that the existing uncertainties can alter the ice hardness by 15% in slow moving regions. In East Antarctica, Pittard et al. (2016) show that localized regions of elevated heat flux can substantially change the ice sheet geometry, especially in the interior regions. Therefore, understanding the spatial variations in GHF is crucial, especially in the interior, slow-moving regions of ice sheets.

To resolve the lack of information about GHF beneath the GrIS, several studies have attempted to estimate the GHF in Greenland using remotely-sensed data. For example, Shapiro & Ritzwoller (2004) use seismic tomography based on similarity functions in Greenland to estimate the GHF in Greenland, and Fox Maule et al. (2009) use satellite-based magnetic anomaly data to infer the depth at which the Curie isotherm occurs (known as the 'Curie depth'). By knowing the Curie depth, Fox Maule et al. (2009) produce a GHF distribution in Greenland that is very different from the results by Shapiro & Ritzwoller (2004). Several other studies have also aimed at predicting the GHF in Greenland (e.g. Pollack et al., 1993; Martos et al., 2018). However, the derived maps often contradict each other, and cannot reproduce the measured basal temperatures at ice core locations when implemented in numerical ice sheet models (Rogozhina et al., 2012). These uncertainties impact the reliability of future sea level rise predictions in numerical models. Therefore, there is a strong need to reconstruct the GHF beneath the GrIS by reconciling remote sensing observations, ice core information, and numerical models.

1.5 Dissertation objectives

The focus of this dissertation is to combine analytical solutions, numerical ice sheet models, and remote sensing observations from radio-echo sounding (RES) to improve our current understanding of the basal thermal state and GHF distribution of the GrIS. In particular I seek to answer the following questions:

1. Are the current analytical solutions for estimating ice sheet temperatures reliable? If not, can they be improved?

2. What is the spatial distribution of GHF in Greenland?

3. Is there a statistical relationship between global GHF measurements and geologic/tectonic variables? If yes, can GHF in Greenland be statistically predicted?

4. How can radar data help constrain the GHF in Greenland?

5. Can the various GHF models be reconciled using radar data and ice core information?

6. Do the uncertainties in GHF models make a substantial difference for estimating the rate of basal melt-water production?

1.6 Dissertation outline

This dissertation consists of 5 chapters. This introduction is the first chapter, and Chapters 2, 3, and 4 are the main body of research conducted by the author. Chapter 2 is published in *Journal of Geophysical Research: Earth Surface*, Chapter 3 is published in *Geophysical Research Letters*, and Chapter 4 will be submitted to the *Journal of Glaciology*. The published chapters are repeated here, verbatim from what has been published and the official citation to the paper is reported as a footnote on the first page of the chapters. A list of references is provided at the end of the dissertation.

1.6.1 Chapter 2: An improved analytical solution for the temperature profile of ice sheets

This chapter outlines the shortcomings of a 60 year-old analytical solution to estimate the temperature profile of ice sheets (Robin, 1955). Then main shortcoming of the Robin solution is due to a simplified assumption of a linear decrease of the vertical velocity profile from the surface mass balance on the surface to zero at the bed. I demonstrate that the 1D energy conservation equation for ice sheets is very sensitive to the choice of vertical velocity profile. Then, I present an alternative way to solve the 1D energy equation in the vertical direction for the interior regions of ice sheets to resolve the shortcomings of the Robin (1955) solution. I also propose a simplified method to incorporate strain heating in the new analytical solution. Finally, I investigate the regions of applicability of the presented solution in Greenland and Antarctica. In Chapter 4, this analytical solution is used as a computationally frugal method to analyze the sensitivity of the minimum required heat flux to thaw the bed in Greenland.

1.6.2 Chapter 3: Predicting the geothermal heat flux in Greenland: a Machine Learning approach

Nearly 40,000 continental GHF measurements are available globally. In this chapter, I combine of all these GHF measurements with globally available geologic and tectonic parameters that are potentially related to GHF (such as crustal thickness and age) to establish a statistical relationship between the geologic features and GHF. I train a machine learning algorithm and evaluate the rigor of the constructed statistical relationship. Then I use the trained algorithm to predict the GHF for Greenland.

1.6.3 Chapter 4: Constraining the geothermal heat flux in Greenland: comparing ice cores, radar observation, and numerical models

In this chapter, I use the locations of radar-detected basal thaw to constrain the GHF in Greenland. I use the large-scale numerical ice sheet model SICOPOLIS and iteratively adjust the GHF in Greenland and calculate the minimum GHF required to thaw the bed. Then I show that the existing GHF models do not honor these estimated GHF constraints and I discuss the reasons for numerous discrepancies between GHF models, radar inferences of basal thaw, and ice core information.

1.6.4 Chapter 5: Summary and conclusion

Here, I summarize and synthesize the results of the dissertation. I discuss how the research conducted in this work has improved our understanding about the basal thermal state of the GrIS and suggest potential directions for future research to improve the current advances.

1.6.5 Appendix A: Supplementary Information for Chapter 3

This appendix outlines the details of the machine learning algorithm that was used in Chapter 3. Here, I investigate the robustness and stability of the employed algorithm, as well as verifying that overfitting is avoided while training the algorithm. Additionally I show the results of feature-importance analysis, obtained from the training step. Finally, I show the map of global GHF measurements on the continental crust, in addition to auxiliary tables and maps showing the GHF measurements at ice core or borehole sites in Greenland.

Chapter 2

An improved analytical solution for the temperature profile of ice sheets[1]

[1]This chapter has been published as Rezvanbehbahani, S., van der Veen, C. J., & Stearns, L. A. (2019). An improved analytical solution for the temperature profile of ice sheets. Journal of Geophysical Research: Earth Surface.

Abstract

The one-dimensional steady-state analytical solution of the energy-conservation equation obtained by Robin (1955) is frequently used in glaciology. This solution assumes a linear decrease in surface velocity from a maximum value equal to the mass balance at the surface to zero at the bed. Here we show that this assumption of a linear velocity profile leads to large errors in the calculated temperature profile and especially in basal temperature. By prescribing a non-linear power function of elevation above the bed for the vertical velocity profile arising from use of the Shallow Ice Approximation (SIA), we derive a new analytical solution for temperature. We show that the solution produces temperature profiles identical to numerical temperature solutions with the SIA vertical velocity near ice divides. We quantify the importance of strain heating and demonstrate that integrating the strain heating and adding it to the geothermal heat flux at the bed is a reasonable approximation for the interior regions. Our analytical solution does not include horizontal advection components, so we compare our solution with numerical solutions of a two-dimensional advection-diffusion model and assess the applicability and errors of the analytical solution away from the ice divide. We show that several parameters and assumptions impact the spatial extent of applicability of the new solution including surface mass-balance rate and surface temperature lapse rate. We delineate regions of Greenland and Antarctica within which the analytical solution at any depth is likely within 2 K of the actual temperatures with horizontal advection.

2.1 Introduction

Variations in ice temperature affect the deformation rate by altering the rate factor several orders of magnitude (e.g. Hooke, 1981), as well as the occurrence of sliding when basal temperatures reach the melting point (e.g. Iken & Bindschadler, 1986). Therefore, robust estimation of ice-sheet temperatures is essential for modeling of ice flow. The temperature fields of ice sheets can be calculated using a variety of numerical models (e.g. SICOPOLIS, Greve & Hutter (1995); ISSM, Larour et al. (2012b); VarGlaS, Brinkerhoff & Johnson (2013); PISM, Aschwanden et al. (2012), etc.). However, applying these models often requires computationally expensive simulations. In contrast, analytical temperature solutions are useful because: 1) they are significantly easier to implement, 2) they serve as a validation tool for numerical models, 3) they facilitate analyzing the sensitivity of temperature profiles to various input parameters, and 4) they can provide efficient tools for initializing numerical ice sheet simulations (e.g., Aschwanden et al., 2013; Adalgeirsdottir et al., 2014).

The only analytical temperature solution widely used in glaciology is the Robin (1955) solution. Robin emphasizes that his model is suitable only for the "temperature distribution near the centre of an ice sheet". This model is often used as a 'back-of-the-envelope' means for estimating basal temperatures (e.g. Anandakrishnan et al., 1998; Siegert, 2000; Palmer et al., 2013; Jezek et al., 2015; Portnov et al., 2016), but there has been no attempt to validate or quantify uncertainties associated with this solution or define the area within which the Robin solution can be applied.

The Robin solution approximates the distribution of the vertical velocity as decreasing linearly from the surface value, equal to minus the surface mass-balance rate, to zero at the glacier bed. Here we show that this assumption leads to an underestimation of temperatures, owing to extreme sensitivity of the energy conservation equation to parameterization of vertical velocity (section 2.2.1). In order to resolve this issue, we approximate the vertical velocity obtained from the Shallow Ice Approximation (SIA) (Hutter, 1983) with a power function of elevation above the bed. We then implement this velocity profile in the one-dimensional, steady-state advection-diffusion equation and derive a new analytical solution that substantially improves the temperature

estimates (sections 2.2.2 and 2.2.3).

The presented analytical solution does not include strain heating and therefore, we evaluate its importance on the temperature profile (section 2.3). Additionally, we confirm the applicability of a previous suggestion of incorporating strain heating by adding the depth-integrated strain heating to the geothermal heat flux at the bed (Fowler, 1992) in the analytical solutions (section 2.3). Since the new analytical solution ignores horizontal heat advection, we also compare the temperatures from the analytical solution to that of a two-dimensional steady-state ice sheet model, aiming at approximating the spatial extent away from the ice divide where our solution can be applied (section 2.4). Finally the results, implications, and spatial extent of applicability to Greenland and Antarctic ice sheets are discussed (section 4.4).

2.2 One-dimensional models

In the interior of ice sheets, where horizontal velocities are small, the energy conservation can be considered in the vertical (z) direction only. That is, horizontal advection and diffusion of heat are assumed small and negligible. In steady-state conditions, the 1D energy conservation with constant heat flux at the bed (G) and constant temperature at the surface (T_s) for an ice thickness of H is (Van der Veen, 2013, Section 6.2);

$$-K\frac{\partial^2 T}{\partial z^2} + v_z\frac{\partial T}{\partial z} = \frac{Q_s}{\rho c}, \text{ for } z \in \Omega = (0, H) \tag{2.1a}$$

$$\frac{\partial T}{\partial n_z} = -\frac{G}{\kappa}, \quad \text{for } z \text{ on } \Gamma_N\ (z = 0) \tag{2.1b}$$

$$T = T_s, \text{ for } z \text{ on } \Gamma_D\ (z = H), \tag{2.1c}$$

where T is the ice temperature, K is thermal diffusivity and κ is thermal conductivity, v_z is the vertical velocity, ρ and c are ice density and specific heat capacity, respectively. The surface and basal boundaries are denoted by Γ_D and Γ_N, while Ω refers to the ice column (minus the

Table 2.1: Symbols, values, and units.

Symbol	Value	Unit	Description
A	5×10^{-8}	$\text{kPa}^{-3}\ \text{yr}^{-1}$	deformation rate factor
$\dot{b}$		m yr^{-1}	basal melt rate
c	2097	$\text{J kg}^{-1}\ \text{K}^{-1}$	heat capacity
$\text{erf}(x)$			error function
$\dot{\varepsilon}_{xz}$		yr^{-1}	strain rate of vertical shear
G	50	mW m^{-2}	geothermal heat flux
G_s		mW m^{-2}	depth-integrated strain heating
γ			non-linear exponent of vertical velocity
γ_+			optimal exponent
$\Gamma(a,x)$			upper incomplete gamma function
H		m	ice thickness
K	34.4	$\text{m}^2\ \text{yr}^{-1}$	thermal diffusivity
κ	2.10	$\text{W m}^{-1}\ \text{K}^{-1}$	thermal conductivity
L		m	ice sheet length
L_f	333.5	kJ kg^{-1}	laten heat of fusion
$\dot{M}$		m yr^{-1}	surface mass-balance rate (ice equivalent)
n	3		Glen's flow law exponent
n_x, n_z			normal vectors
Q_s		mW m^{-2}	strain heating
ρ	910	kg m^{-3}	ice density
T		°C	temperature
T_s		°C	surface temperature
T_b		°C	basal temperature
τ_{dx}		kPa	driving stress
$\vec{v} = \{v_x, v_z\}$		m yr^{-1}	horizontal and vertical velocity

boundaries). The quantity **n** is the unit normal vector with components $\{n_x, n_z\}$ in horizontal and vertical directions, respectively. Symbols and their values are defined in Table 2.1.

In this study, we initially ignore strain heating Q_s in the analytical derivation. We then include Q_s in the numerical solution and show how it affects the temperature profile. We also evaluate a simple method to include strain heating in the analytical solution in section 2.3. Since we focus on non-temperate ice, the surface temperatures that we use are cold enough to ensure that the basal temperatures will not reach the pressure melting point throughout the study. Frictional heating at the bed is also ignored.

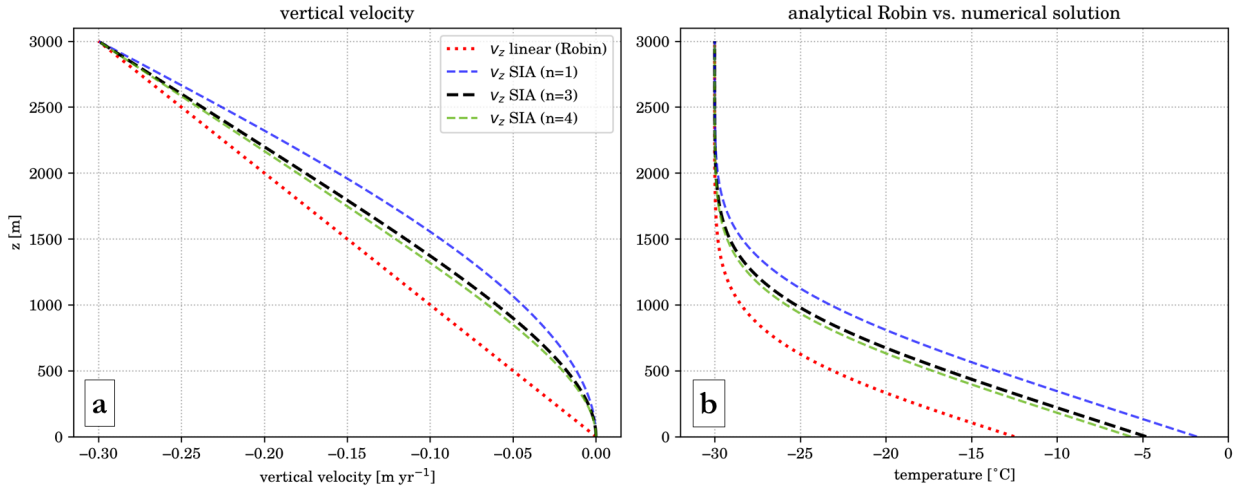

Figure 2.1: Parameterization of vertical velocities (a), and their corresponding temperature profiles (b) from the SIA (equation 2.4) with different exponents of Glen's flow law and the Robin solution (equation 2.3). The linear v_z from the Robin solution (*red dotted*) is compared with the exact vertical velocity from SIA (*dashed*). Surface mass-balance rate, $\dot{M}$, is 0.3 m yr^{-1} and geothermal heat flux is G=50 mW m^{-2}.

2.2.1 Accuracy of Robin's analytical solution

In the absence of basal melt, if the vertical ice velocity, v_z, is assumed to vary linearly from minus the surface mass-balance rate, $-\dot{M}$, at the ice surface to zero at the bottom (with z-axis positive upwards), where the bed is at $z = 0$

$$v_z = -\frac{\dot{M} z}{H}, \tag{2.2}$$

then the analytical solution obtained by Robin (1955) for ice temperature at a given depth reads

$$T(z) = T_s - \frac{G\sqrt{\pi}}{2\kappa q}[\mathrm{erf}(zq) - \mathrm{erf}(Hq)], \tag{2.3}$$

with $q = \sqrt{\frac{\dot{M}}{2KH}}$ and the error function is defined as $\mathrm{erf}(z) = \frac{2}{\sqrt{\pi}} \int_0^z \exp(-z'^2)\, dz'$, where z' is a dummy variable. The basal temperature can be obtained by setting $z = 0$ in equation (2.3). Equation (2.2) holds when the bed is frozen, and therefore, basal vertical velocity is zero. However, extensions to the Robin solution have been proposed by Zotikov (1986, Section 4.2) and Hindmarsh et al. (2009) to include basal melt by introducing a non-zero vertical velocity at the bed in

the analytical solution.

Robin's linear approximation for the vertical velocity does not substantially deviate from vertical velocities obtained by using the SIA. However, the system of equations (2.1) is very sensitive to the choice of vertical velocity distribution with inappropriate approximations leading to incorrect temperature estimates.

Using the SIA and further assuming that the surface vertical velocity equals the surface mass-balance rate, the vertical velocity for $z \in (0, H)$ is (Hindmarsh, 1999),

$$v_{z_{SIA}} = -\frac{\dot{M}}{n+1}\left[\left(1-\frac{z}{H}\right)^{n+2} - 1 + (n+2)\frac{z}{H}\right]. \tag{2.4}$$

We use a finite element framework, FEniCS (Logg et al., 2012), to solve equation (2.1) numerically, given the SIA vertical velocity profile for equation (2.4). Comparison of the numerical temperature solution with that of the Robin solution (Fig. 2.1) shows that small differences in the vertical velocity distribution leads to the underestimation of the basal temperature by $\sim$8 K in the Robin solution. This is because the linear velocity profile systematically overestimates the vertical velocity at depth, and thus overestimates the downward advection of colder ice from the surface to deeper ice layers. Therefore, the Robin solution must be cautiously used as a 'back-of-the-envelope' method to estimate temperature in the interior regions. Note that warmer ice near the bed (produced by the geothermal heat flux) changes the profile from the form of (2.4) to more resemble the Robin solution profile (2.2), reducing the numerical error associated with the Robin solution. In the following section, we address this issue by proposing a new analytical solution to equation (2.1).

2.2.2 New analytical temperature solution

Assuming $n = 3$, the vertical velocity profile in the SIA (equation 2.4) is a fifth-order polynomial. Deriving an analytical solution for the temperature profile in equation (2.1) using this equation is not straightforward and may not be possible. However, equation (2.4) can be approximated with a

similar form to that of the Robin's approximation but with an exponent greater than unity for the z/H term so as to introduce a concavity to the vertical velocity profile, similar to that produced by modeling internal deformation using the SIA (Fig. 2.1). Thus

$$v_z = -\dot{M}\left(\frac{z}{H}\right)^{\gamma}. \tag{2.5}$$

To find an analytical solution to the temperature equation (2.1) using this form for the velocity profile, we follow the classic procedure for solving second order ordinary differential equations without the source term outlined by, for example, Boyce et al. (1969, Chapter 3).

Substituting profile (2.5) in equation (2.1) and, for now, setting Q_s to zero, the 1D advection-diffusion equation becomes,

$$\frac{\partial^2 T}{\partial z^2} + \frac{\dot{M}}{KH^{\gamma}} z^{\gamma} \frac{\partial T}{\partial z} = 0. \tag{2.6}$$

Next, we define λ as

$$\lambda = \frac{\dot{M}}{KH^{\gamma}}. \tag{2.7}$$

The heat equation can then be written as

$$\frac{\partial^2 T}{\partial z^2} + \mathscr{P}(z) \frac{\partial T}{\partial z} = 0, \tag{2.8}$$

where $\mathscr{P}(z) = \lambda z^{\gamma}$.

We define the temperature gradient term as $\frac{\partial T}{\partial z} = \psi(z)$, so that the heat equation becomes

$$\frac{\partial \psi(z)}{\partial z} + \mathscr{P}(z)\psi(z) = 0. \tag{2.9}$$

The solution of the function $\psi(z)$ is (Boyce et al., 1969, chapter 3)

$$\psi(z) = \frac{C_1}{\mu(z)}, \tag{2.10}$$

where $\mu(z)$ is the integrating factor defined as

$$\mu(z) = \exp\left(\int \mathscr{P}(z)dz\right) = \exp\left(\int \lambda z^{\gamma} dz\right) = \exp\left(\frac{\lambda}{\gamma+1} z^{\gamma+1}\right). \tag{2.11}$$

At the ice sheet bed, $\psi(z) = \frac{\partial T}{\partial z}\Big|_{z=0}$ represents the geothermal flux boundary condition on a flat bed (equation 2.1b),

$$\psi(0) = \frac{C_1}{\mu(0)} = -\frac{G}{\kappa}. \tag{2.12}$$

From equation (2.11) we know that $\mu(0) = 1$, meaning that $C_1 = -\frac{G}{\kappa}$ and the full expression for $\psi(z)$ is

$$\psi(z) = \frac{-\frac{G}{\kappa}}{\mu(z)} = -\frac{G}{\kappa}\exp\left(-\frac{\lambda}{\gamma+1} z^{\gamma+1}\right). \tag{2.13}$$

Then, by defining $\phi = -\frac{\lambda}{\gamma+1}$, the temperature profile $T(z)$ can be obtained by integrating $\psi(z)$ as

$$T(z) = \int \psi(z)dz = -\frac{G}{\kappa}\int \exp\left(\phi z^{\gamma+1}\right) dz. \tag{2.14}$$

Therefore, the general solution to the temperature profile is

$$T(z) = -\frac{G}{\kappa}\left(\frac{-z\left(-\phi z^{\gamma+1}\right)^{\frac{-1}{\gamma+1}}}{\gamma+1}\right)\Gamma\left(\frac{1}{1+\gamma}, -\phi z^{\gamma+1}\right) + C_2. \tag{2.15}$$

where $\Gamma(\cdot,\cdot)$ is the upper incomplete gamma function (a.k.a. the Euler integral of second kind) defined by Boyce et al. (1969, chapter 6),

$$\Gamma(a,x) = \int_x^{\infty} t^{a-1} e^{-t} dt. \tag{2.16}$$

The value of $\Gamma(\cdot,\cdot)$ can be found in ordinary differential equation textbooks or standard numerical tables (e.g. Abramowitz & Stegun, 1964), as well as in several standard software packages, e.g. NAG®, MATLAB®.

The integration constant, C_2, is found by setting $T(H)$ equal to the surface temperature, T_s. Substitution of this into equation (2.15) produces

$$T(z) = T_s + \frac{G(-\phi)^{\frac{-1}{\gamma+1}}}{\kappa(\gamma+1)}\left[\Gamma\left(\frac{1}{1+\gamma}, -\phi z^{\gamma+1}\right) - \Gamma\left(\frac{1}{1+\gamma}, -\phi H^{\gamma+1}\right)\right]. \tag{2.17}$$

Equation (2.17) is a general form of the analytical steady-state solution to the 1D energy equation with a prescribed heat flux at the bed, surface temperature T_s, and a velocity parameterization of the form $-\dot{M}(\frac{z}{H})^{\gamma}$ with $\gamma > 0$. In the special case where $\gamma = 1$, the error function emerges from the upper incomplete gamma function through $\text{erf}(x) = 1 - \frac{\Gamma(\frac{1}{2}, x^2)}{\sqrt{\pi}}$ (Gautschi, 1998; Amore, 2005) and the Robin solution is reproduced. The difference between basal and surface temperature can be obtained by setting $z = 0$ in equation (2.17),

$$T_b - T_s = \frac{G(-\phi)^{\frac{-1}{\gamma+1}}}{\kappa(\gamma+1)}\left[\Gamma\left(\frac{1}{1+\gamma}, 0\right) - \Gamma\left(\frac{1}{1+\gamma}, -\phi H^{\gamma+1}\right)\right]. \tag{2.18}$$

The value of γ that produces the best fit for approximating the vertical velocity profile obtained from the SIA (equation 2.4) is $\gamma = 1.397$. However, comparing the temperature profile calculated with this value in the analytical solution with the temperature profile obtained numerically (with the vertical velocity profile given by equation 2.4) shows that the analytical solution does not quite match the numerical solution with γ=1.397. Further adjustment of γ is required to match the temperature profile from analytical solution with that of the numerical solution.

To find the optimal γ (hereafter γ_+), we plot temperature profiles from the analytical solution for a range of γ values in order to match this solution with the numerical solution (Fig. 2.2). For the specific case shown in Fig. (2.2) (that is, $\dot{M}$=0.3 m yr^{-1} and H=3000 m), we find that γ_+=1.523. However, γ_+ depends upon surface mass-balance rate and thickness values, which is investigated in section 2.2.3.

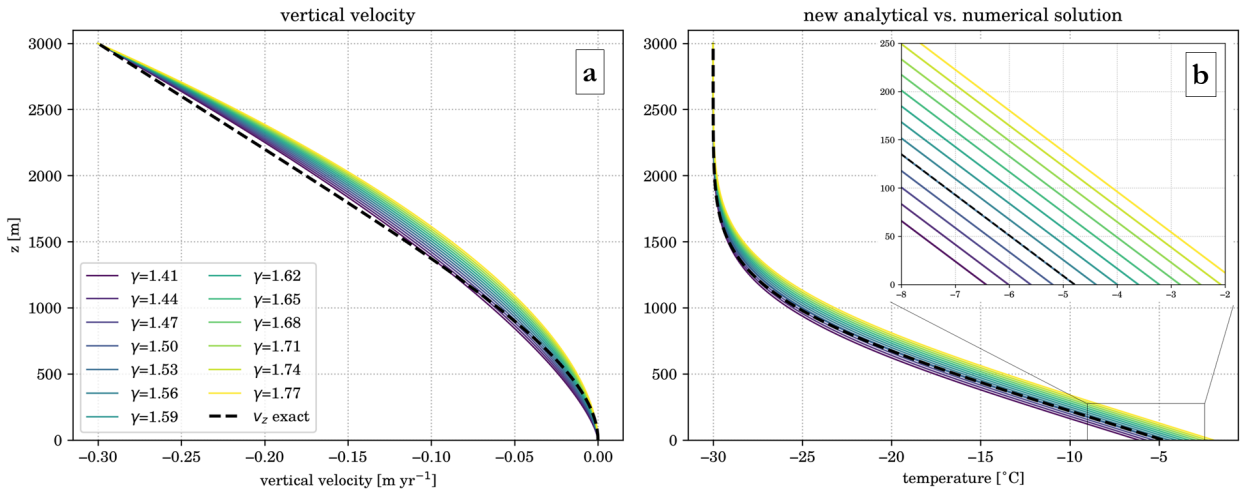

Figure 2.2: Parameterization of vertical velocity with different exponents (a), and their corresponding temperature profiles (b). The exact v_z from the SIA (equation 2.4, *dashed black*) is compared with nonlinear power functions. A range of γ values are used to estimate velocities (*colored lines*). In this specific case, $\gamma = 1.532$ shows the optimal exponent to match temperature calculations from our solution with that of SIA exact vertical velocities (*inset*). $\dot{M}$ is 0.3 m yr^{-1}.

2.2.3 Finding γ_+

We perform a series of experiments to investigate parameters that affect γ_+. We find that γ_+ is sensitive to surface mass-balance rate ($\dot{M}$) and ice thickness (H). Since $\dot{M}$ has the unit of velocity, the vertical Péclet number can be defined as $Pe = \frac{\dot{M}H}{K}$ (hereafter we drop 'vertical'). The Péclet number is a non-dimensional number that represents the ratio of advective to diffusive heat transfer (Bergman et al., 2011, Section 6.6). The vertical temperature distribution of the ice sheet strongly depends on Pe number. If $Pe = 0$ (i.e. no vertical advection), the vertical temperature distribution becomes linear with slope determined by the geothermal heat flux. In steady-state conditions with large Pe, advective heat transfer dominates the upper part of the ice sheet, causing the upper layers to become isothermal (same as the surface temperature) while the lower parts of the column will be mostly modulated by conductive heat transfer forming a conductive boundary layer near the bottom (Zotikov, 1986; Cuffey & Paterson, 2010). The normalized thickness of the conductive boundary layer near the bottom is $Pe^{-1/3}$ for the case of internal shearing, and $Pe^{-1/2}$ for plug flow (Morland, 1984).

The range of Péclet numbers considered here is between ∼2 and 100, corresponding to $\dot{M}$

values from 0.1 to 1.5 m yr^{-1} and thickness values from 1000 to 3000 m (e.g. Van den Broeke et al., 2011). In the thick interior regions of ice sheets, vertical velocity as measured by the Péclet number is often insubstantial. For example, in the East Antarctic Ice Sheet (EAIS) the Péclet number lies between 2 and 4. Although *Pe* values as high as 100 are atypical in Greenland and Antarctica, they can occur in ice-caps in Iceland or Antarctic Peninsula. We include this wide range of *Pe* numbers for completeness.

In order to find the γ_+, we iteratively solve for the γ in equation (2.18) with a fixed surface temperature T_s, in order to match the basal temperature from the analytical solution with the numerical solution. The iteration is terminated when the difference between basal temperatures from the two models is less than 0.05 K. Results are summarized in Fig. 2.3 where γ_+ is shown to have a logarithmic relationship with Péclet number as,

$$\gamma_+ = 1.39 + 0.044 \ln(Pe). \tag{2.19}$$

Hereafter, all the calculations from the analytical solution are with γ_+ obtained from equation (2.19), unless otherwise is specified. Note that since our analysis is thermo-mechanically decoupled, the vertical velocity distribution is independent of the ice temperature. Therefore, the value of γ_+ does not vary with changing T_s or G.

2.3 Effect of strain heating

The analytical solution (2.17) is obtained in the absence of strain heating in (2.1). Since strain heating is a depth-dependent term, it cannot be easily incorporated in the analytical solution. However, because most vertical shear is concentrated in the basal ice layers, Fowler (1992) suggests that a good approximation is that the strain heating can be included by adding it to the basal boundary condition (equation 2.1b). In this section, we investigate under which conditions this 'lumping' of strain heating to the basal boundary condition is valid, by comparing the basal temperatures estimated from the analytical solution with those obtained from the numerical solution (which

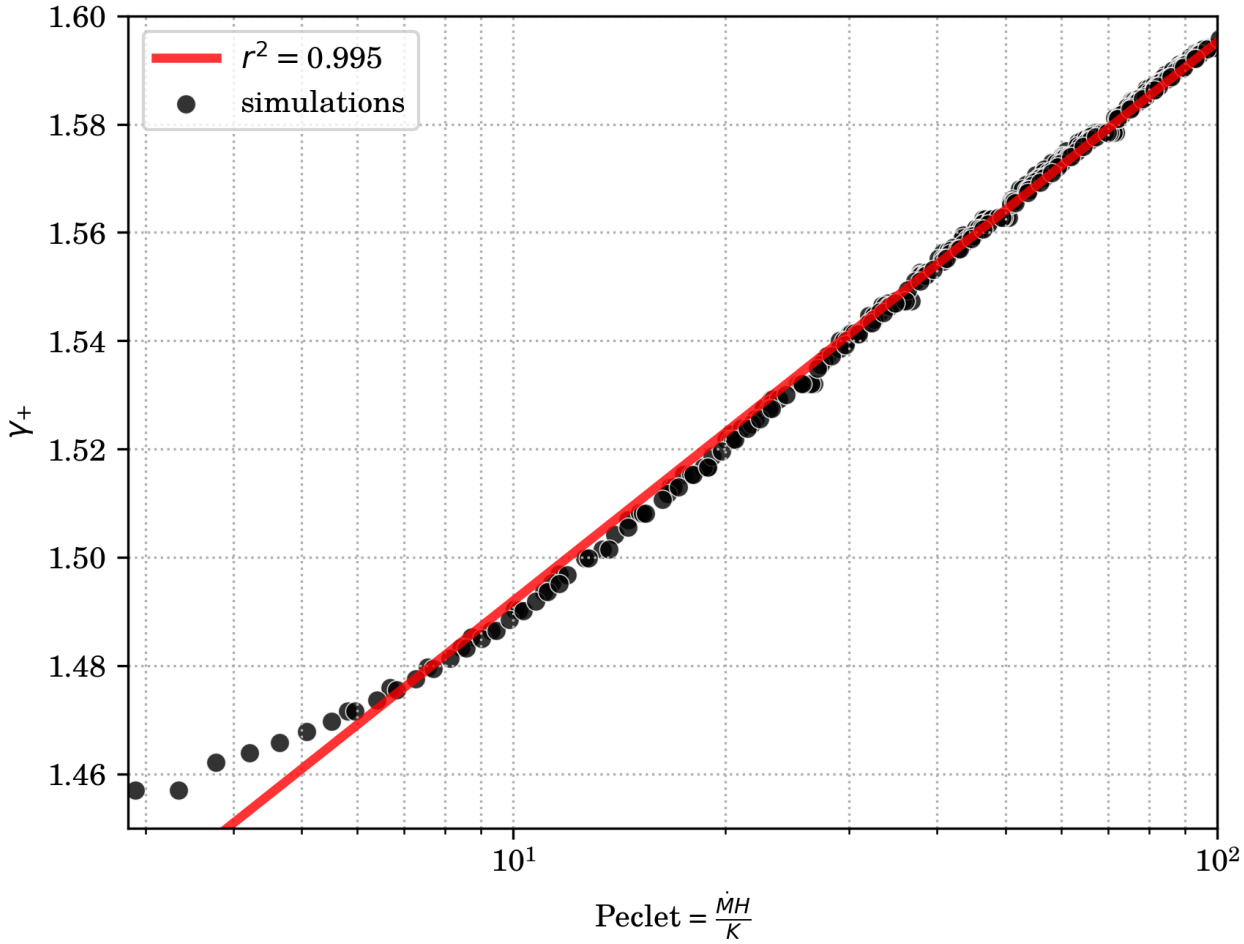

Figure 2.3: Dependence of γ_+ on vertical *Pe*. The value for γ_+ is calculated by iterative adjustment of γ in our solution to match the numerical solution (*black circles*), and the logarithmic fit (*red line*) provides an expression for finding the optimal gamma value. The γ_+ is independent of basal and surface boundary conditions (G and T_s).

includes explicit calculation of strain heating at depth).

Heat released by internal deformation of ice can be expressed in terms of vertical shear strain rate ($\dot{\varepsilon}_{xz}$) and shear stress (τ_{xz}) at depth through (e.g. Van der Veen, 2013, Section 4.2)

$$Q_s = 2\ \dot{\varepsilon}_{xz}\ \tau_{xz}. \tag{2.20}$$

This equation is a valid approximation when SIA constraints hold. For lamellar flow the shear stress increases linearly from zero at the surface to maximum shear stress at the bed. In case of SIA, the basal shear stress equals the driving stress which is calculated by $\tau_{dx} = -\rho g H \frac{\partial H}{\partial x}$ (Nye,

1952). Applying Glen's constitutive relation with $n = 3$, and rate factor A to express the vertical strain rate in terms of the shear stress, the strain heating at depth becomes (Van der Veen, 2013; Blatter & Greve, 2015),

$$Q_s = 2A \left(1 - \frac{z}{H}\right)^4 \tau_{dx}^4. \tag{2.21}$$

If the temperature is solved numerically, this term can be added explicitly at every depth (note that dependence of rate factor, A, on temperature is neglected). However, including the source term in the form of equation (2.21) in the 1D energy conservation equation would further complicate the analytical temperature solution, if a solution exists at all. Therefore, we evaluate whether strain heating can be incorporated by elevating the heat flux at the bed. The total strain heating in an ice column (G_s) can be obtained by integrating equation (2.21) along a vertical profile, and

$$G_s = \int_0^H Q_s \, dz = \int_0^H 2A \left(1 - \frac{z}{H}\right)^4 \tau_{dx}^4 \, dz = \frac{2}{5} AH \tau_{dx}^4. \tag{2.22}$$

This amount of strain heating needs to be added to the basal boundary condition used in the analytical solution.

To assess the importance of strain heating for temperature of an ice column, we compare temperature profiles from 1) temperature profile from the analytical solution without strain heating, 2) temperature profile from the analytical solution with G_s added to the geothermal heat flux, and 3) numerical solution with Q_s as strain heating at depth. The ice thickness is 3000 m with T_s of $-30°$C, $\dot{M}$ of 0.3 m yr^{-1}, and G of 50 mW m^{-2}. Since strain heating depends on rate factor and driving stress, different values of rate factor are chosen to represent the effect of hard and soft ice, in addition to three driving stress values (Fig. 2.4). The three driving stress values of 20, 40, and 60 kPa are chosen as typical values in the interior regions of ice sheets (see Fig. 1 in Sergienko et al., 2014)

Our results indicate that for low driving stresses ($\sim$20 kPa), regardless of the rate factor, the effect of strain heating is negligible, and all three profiles (with different rate factors) produce

nearly identical temperatures (Fig. 2.4a,d,g). At a driving stress of 40 kPa, temperature estimates from both the numerical inclusion of strain heating (Q_s) and the 'lumped' strain heating (G_s) increase, with the 'lumped' strain heating slightly overestimating the basal temperatures compared to the numerical solutions. For a soft ice with the rate factor of 10^{-7} kPa^{-3} yr^{-1} (corresponding to $\sim -5^{\circ}$C), the basal temperature with G_s exceeds that of Q_s by less than 2 K. However, ignoring the strain heating underestimates the basal temperature by about $\sim$4 K (Fig. 2.4h). With the driving stress of 40 kPa, these two approaches of including the strain heating (i.e., Q_s and G_s) produce relatively similar temperature profiles, confirming the previous suggestion by Fowler (1992). With the driving stress of 60 kPa, temperature overestimation of the 'lumped' method compared with the numerical inclusion of Q_s is small for a hard ice with a rate factor of 10^{-8} kPa^{-3} yr^{-1} (Fig. 2.4c). However, this overestimation rapidly increases for softer ice with rate factors of 5×10^{-8} and 10^{-7} kPa^{-3} yr^{-1}, making the 'lumping' method inaccurate (Fig. 2.4f,i).

Since both G_s and Q_s are related to the fourth power of driving stress, the significance of including strain heating (either through G_s or Q_s) sharply increases with increase in driving stress. Therefore, ignoring the strain heating in the analytical solution results in erroneous underestimation of temperature profile. Although the 'lumping' method suggested by Fowler (1992) slightly overestimates the basal temperature compared with the numerical inclusion of Q_s, the magnitude of its overestimation is significantly smaller than the magnitude of underestimation when strain heating is ignored.

Fig. 2.5 shows a similar comparison to that in Fig. 2.4, but for basal temperatures of ice columns with different thickness and rate factors. For a hard ice with rate factor of 10^{-8} kPa^{-3} yr^{-1} (corresponding to $\sim -20^{\circ}$C) ignoring strain heating results in underestimation of basal temperature in the analytical solution by $\sim$2 K. For softer ice the underestimation becomes more marked and rapidly increases with larger driving stress values (Fig. 2.5a). However, lumping the depth-integrated strain heating with geothermal heat flux, despite the slight overestimation of basal temperature compared with the numerical solution with Q_s, produces a more reliable approximation of the basal temperature. Although the difference between the analytical and numerical solu-

tions (with G_s and Q_s, respectively) increases with driving stress (Fig. 2.5b), the difference in basal temperatures remains within $\sim$2 K up to driving stress of $\sim$50-60 kPa. Ignoring the strain heating in the analytical solution, however, results in substantial underestimation of basal temperatures even with small driving stresses and rate factors (Fig. 2.5a). Therefore, our results corroborate the findings of Fowler (1992) and G_s obtained from equation (2.22) must be incorporated in the analytical solution.

Note that a uniform rate factor over the depth of the ice column has been used throughout this study. The rate factor is, however, a temperature-dependent parameter, but that is not considered here. In order to properly account for the changes of rate factor, the energy equation must be solved numerically by parameterizing the rate factor as a function of temperature (e.g. Clarke et al., 1977), which is not included in this study.

Although the driving stress is zero at the ice divide (and strain heating is consequently zero), our temperature solution does not accurately estimate the basal temperature at the ice divide locations. Since the basal shear stress becomes zero at the ice divide, the SIA assumptions are violated and therefore, the vertical velocity shape function at the ice divide is different from the SIA-derived vertical velocity (Raymond, 1983). Since our solution incorporates an approximation to the SIA-derived vertical velocity profile, it cannot be used at the ice divide where SIA assumptions are violated (see section 4.4 for discussion).

2.4 Effect of horizontal advection

Since the upstream high-elevation regions have a colder surface temperature (owing to temperature lapse rates being negative), the ice that is advected downstream has a lower temperature than the ice deposited immediately above. Hence, the horizontal ice flow lowers the temperature of the downstream regions. Since equation (2.17) is derived as a solution of the 1D temperature equation and ignores the effect of horizontal heat advection, we compare temperatures from our solution with those obtained numerically for a two-dimensional ice sheet. As with the one-dimensional numerical solutions, we use FEniCS to solve the temperature equation,

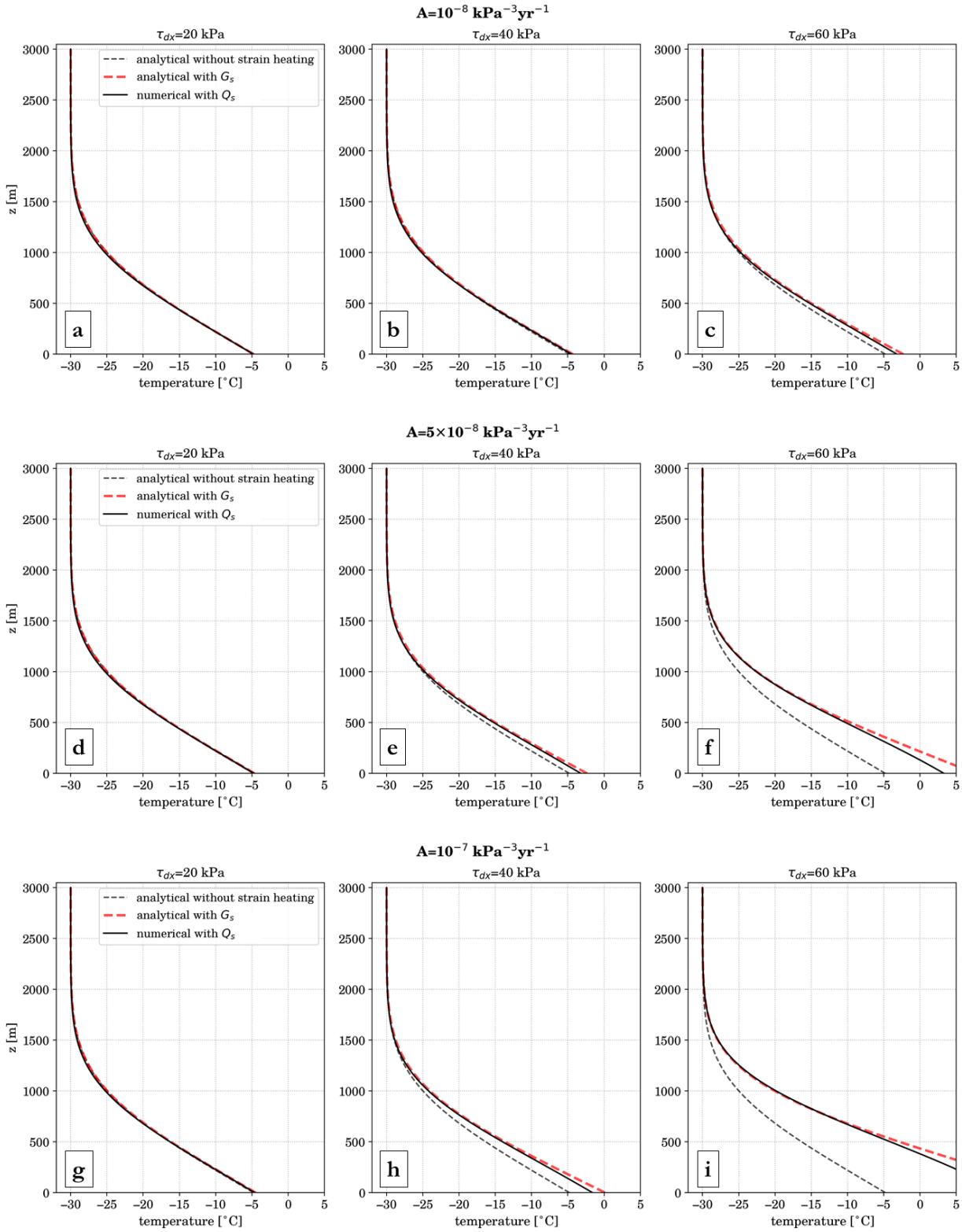

Figure 2.4: Incorporating strain heating in the temperature profile. The analytical solution without strain heating (*dashed grey*) is compared with the numerical solution with strain heating (*solid black*) and addition of depth-integrated strain heating to the geothermal heat flux in the analytical solution (*dashed red*). Temperature profiles at each row have the same rate factor, that correspond to -20, -10, and -5°C, respectively.

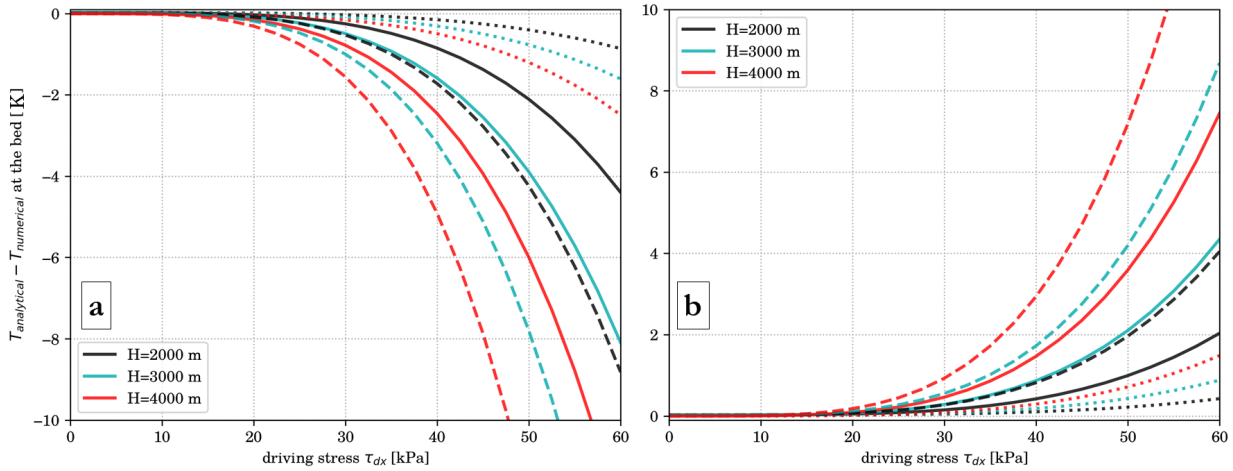

Figure 2.5: Effect of strain heating on the basal temperature of an ice column with varying ice thickness and rate factors. (a) shows the difference between basal temperature from the analytical solution without strain heating and the numerical solution with strain heating, and (b) shows the same temperature difference but depth-integrated strain heating is added to the heat flux at the bed. In the numerical solution, strain heating expression (Q_s, equation 2.21) is incorporated as a source term in the solution (right hand side of equation 2.1). For the analytical solution the depth integrated strain heating (G_s, equation 2.22) is added to the geothermal heat flux of 50 mW m^{-2} at the bottom. Results are shown for three different values of rate factor as $A = 10^{-8}$ (*dotted*), $A = 5 \times 10^{-8}$ (*solid*), and $A = 10^{-7}$ kPa^{-3} yr^{-1} (*dashed*) lines. Note the difference in $y-$axes.

$$-K\left(\frac{\partial^2 T}{\partial z^2} + \frac{\partial^2 T}{\partial x^2}\right) + \left(v_z \frac{\partial T}{\partial z} + v_x \frac{\partial T}{\partial x}\right) = 0, \text{ on } \Omega, \tag{2.23a}$$

$$\frac{\partial T}{\partial n_z} = -\frac{G}{\kappa}, \text{ for } z \text{ on } \Gamma_{N_1}\ (z = 0), \tag{2.23b}$$

$$\frac{\partial T}{\partial n_x} = 0, \text{ for } x \text{ on } \Gamma_{N_2}\ (x = 0), \tag{2.23c}$$

$$T = T_s, \quad \text{for } z \text{ on } \Gamma_D\ (z = H), \tag{2.23d}$$

with Γ_{N_1} denoting the basal boundary and Γ_{N_2} denoting the boundary at the ice divide. We apply a range of surface mass balance and temperature lapse rates for 2D simulations with surface temperature of $-20°$C at zero elevation, chosen sufficiently low to keep basal temperatures below the pressure melting point. Strain heating is also ignored for 2D simulations.

For the ice sheet profile, we use the Vialov (1958) steady-state profile, which is based on

horizontal ice velocity determined by the SIA and constant surface mass-balance rate. The Vialov profile is

$$\left(\frac{H}{H_0}\right)^{2+\frac{2}{n}} + \left(\frac{x}{L}\right)^{1+\frac{1}{n}} = 1, \tag{2.24}$$

with thickness at the ice divide, H_0, defined as

$${H_0}^{2+\frac{2}{n}} = 2\left(\frac{\dot{M}}{A_0}\right)^{\frac{1}{n}} L^{1+\frac{1}{n}}, \tag{2.25}$$

and the constant A_0 defined as

$$A_0 = \frac{2A}{n+2}(\rho g)^n. \tag{2.26}$$

Since the ice thickness goes to zero at the edge of the Vialov profile, we artificially assign a thickness of 5 m to the downstream edge of the profile to prevent singularity in the continuity equation. We adopt the Vialov profile to avoid introducing too many variables and feedbacks. The two-dimensional temperature equation (2.23) is solved numerically for this profile. The artificially-modified 5 m thickness at the edge of the profile has a constant temperature boundary condition of $-20°$C.

The Vialov profile (equation 2.24) is calculated for an ice sheet of length L=750 km and rate factor of A=5×10^{-8} kPa^{-3} yr^{-1}, roughly corresponding to $-10°$C temperature. The uniform rate factor implies that we are not accounting for thermo-mechanical coupling between temperature and ice flow (similar to section 2.3). We use different surface mass-balance rates between 0.3 to 1 m yr^{-1}. After obtaining the surface profile and driving stress through $\tau_{dx} = -\rho g H \frac{\partial H}{\partial x}$, we calculate the horizontal and vertical velocities $\{v_x, v_z\}$ from the SIA (Van der Veen, 2013, equations 4.22-4.30). We then apply the calculated velocities into the 2D energy conservation equation (2.23) and solve for the temperature distribution using the Galerkin finite element method. The streamline upwind Petrov-Galerkin method (SUPG, Brooks & Hughes, 1982) is implemented to stabilize the spurious oscillations arising from the advection terms (similar to Brinkerhoff & Johnson, 2013;

Cummings, 2016).

So far in the analysis, the surface kinematical condition has been equating the surface vertical velocity to $-\dot{M}$. While this is a reasonable approximation close to the ice divide, farther away, the effect of surface slope on the kinematical condition has to be taken into account. For steady-state conditions, the vertical velocity at the surface is related to the mass balance and horizontal velocity at the surface as (Van der Veen, 2013, equation 9.77),

$$v_z\Big|_{surface} = v_x\Big|_{surface} \frac{\partial H}{\partial x} - \dot{M}. \tag{2.27}$$

The surface vertical velocities are calculated from equation (2.27) and applied in the analytical solution.

We present a series of comparisons between our analytical solution and the 2D thermal model. For clarity, only one parameter is changed at a time. Fig. 2.6 shows the difference between the analytical and the numerical solution for a range of surface mass-balance rates with a lapse rate of 7.1 K km^{-1} (the annual average for Greenland, Steffen & Box, 2001). A new Vialov profile and corresponding SIA velocity fields are calculated for every surface mass-balance rate and the surface horizontal velocity along the ice sheet is plotted over the Vialov profile (Fig. 2.6). This comparison shows that the 1D analytical solution overestimates englacial temperatures away from the ice divide (owing to the absence of horizontal advection terms). However, the basal temperature differences remain within $1-2$ K for a large portion of the ice sheet length. Use of the SIA in the creation of the Vialov profile shows that the horizontal velocities increase with an increase in the surface mass-balance rate. Hence the effect of horizontal advection lowers the downstream temperatures (as shown in Fig. 2.6). Although the location of the 2 K offset in basal temperatures varies with changes in $\dot{M}$ values, the magnitude of surface velocities remains between $\sim 100-200$ m yr^{-1} for all profiles (Fig. 2.6).

We assess the effect of surface temperature lapse rate on horizontal heat advection. We use a range of lapse rates from 5 to 8 K km^{-1} to a Vialov profile with $\dot{M}$ of 0.3 m yr^{-1} (Fig. 2.7). Since the surface mass-balance rate is taken as uniform for all comparisons, velocities for all simulations

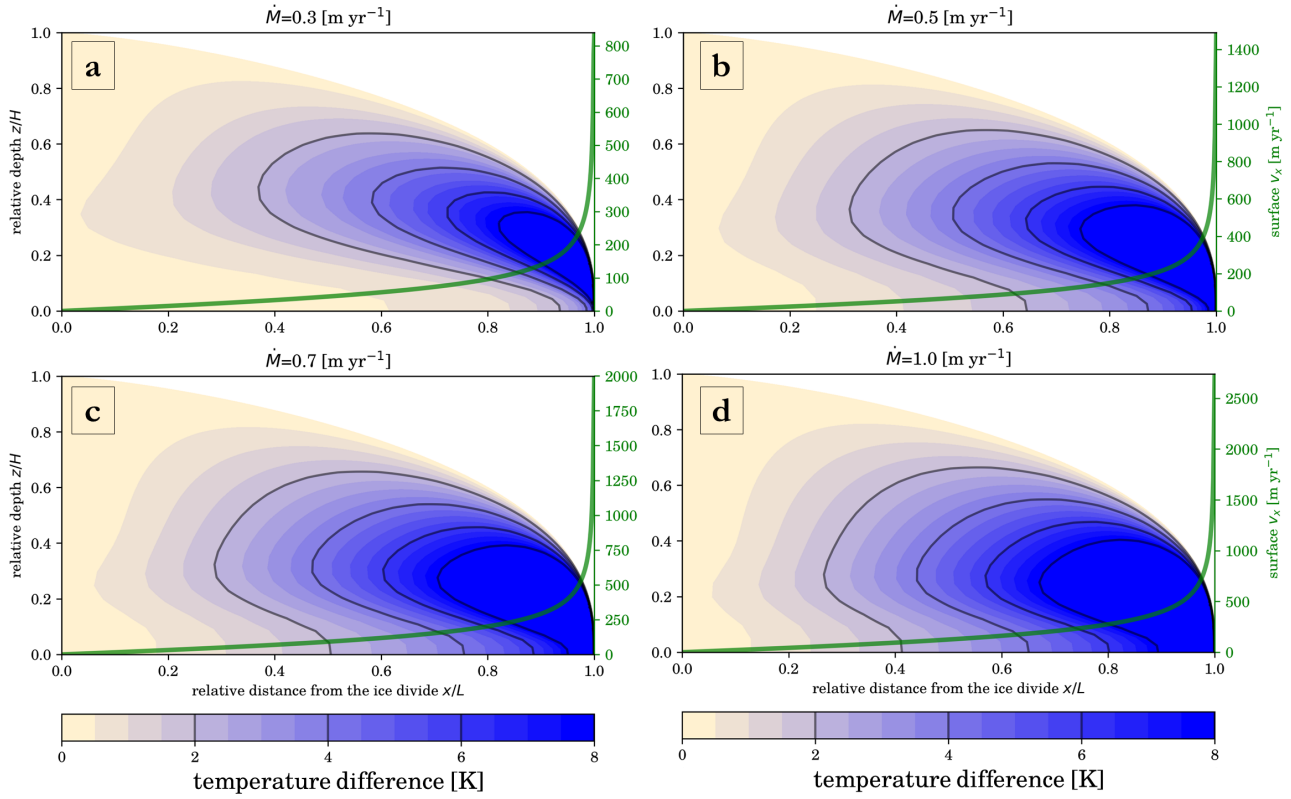

Figure 2.6: Difference between the analytical solution and the full 2D solution ($T_{analytical} - T_{numerical}$) for a Vialov profile with different $\dot{M}$ values and geothermal heat flux of G=50 mW m^{-2}. The analytical solution is calculated using γ_+ as a function of Péclet number (equation 2.19). Surface temperature lapse rate of 7.1 K km^{-1} is used as an average annual value representing Greenland (Steffen & Box, 2001). Contour lines representing two degree intervals are shown (*solid black*). The second y-axis shows the surface horizontal velocity of the Vialov profile (*green line*).

are identical and surface temperature is the only different parameter between these simulations. With a lower lapse rate of 5 K km^{-1} our solution slightly overestimates the basal temperature farther from the ice divide. As the lapse rate increases, the colder ice advected from upstream regions increases and shortens the extent of our 1D solution's applicability within a 2D Vialov profile. The surface horizontal velocity at the location where the offset in basal temperatures is 2 K is $\sim$100 m yr^{-1} (similar to Fig. 2.6).

We summarize the results of experiments with different lapse rates in Fig. 2.8, which shows the maximum normalized distance from the ice divide where the difference between the basal tem-

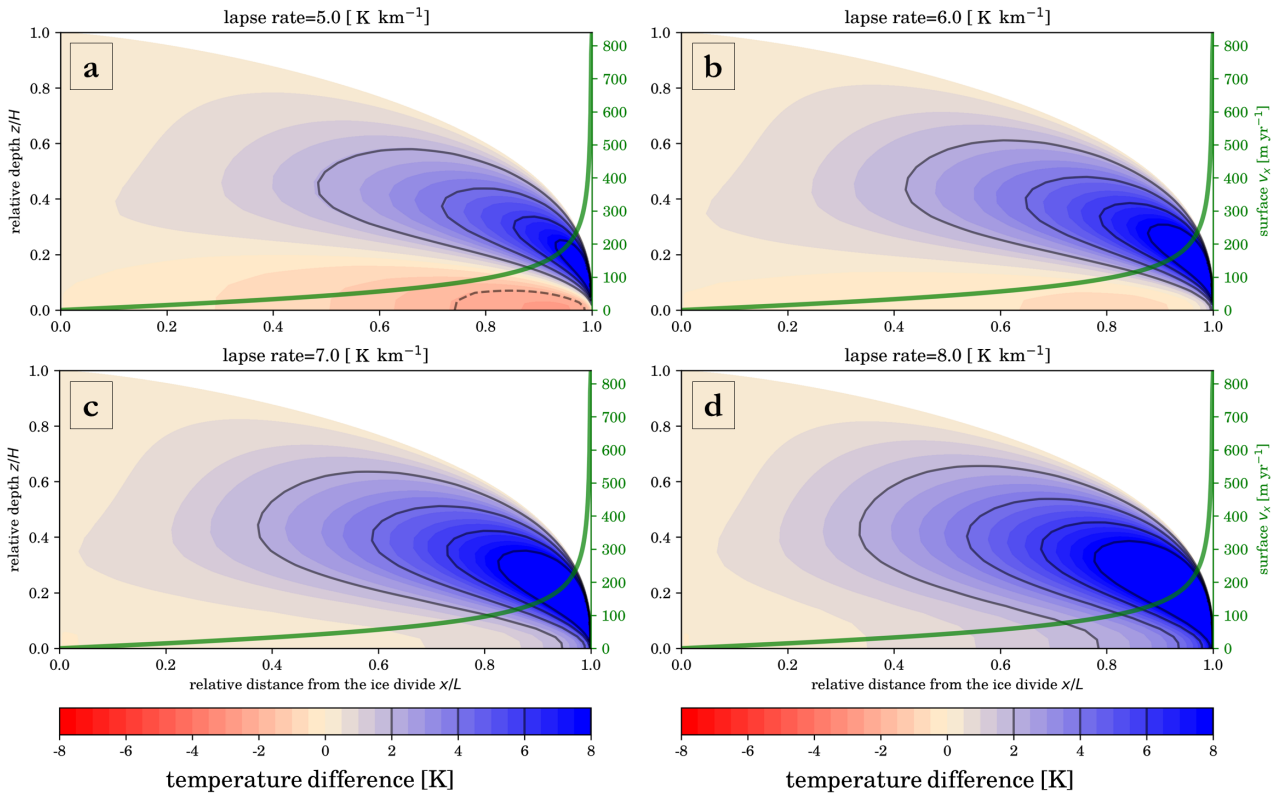

Figure 2.7: Same as Fig. 2.6 with different values for surface temperature lapse rates. The $\dot{M}$ of 0.3 m yr^{-1} is used in the Vialov profile and geothermal heat flux is G=50 mW m^{-2}.

peratures from the two solutions less than a defined threshold. The thresholds, arbitrarily defined at 0.5, 1, and 2 K and are plotted with respect to the range of lapse rates. The extents of applicability show a notable peak at certain lapse rates, below which the analytical solution overestimates, and above which it underestimates the basal temperature profiles. For lapse rates between 5.5−7.5 K km^{-1}, the difference in basal temperature estimates are small for much of the ice-sheet length. However, for low lapse rates of 3−4 K km^{-1} and lapse rates larger than 8 K km^{-1}, the extent of applicability of the 1D analytical solution is more limited.

2.5 Discussion

We have presented a new analytical solution to the 1D vertical heat transport equation with flow field constrained by the Shallow Ice Approximation by parameterizing the vertical velocity of the

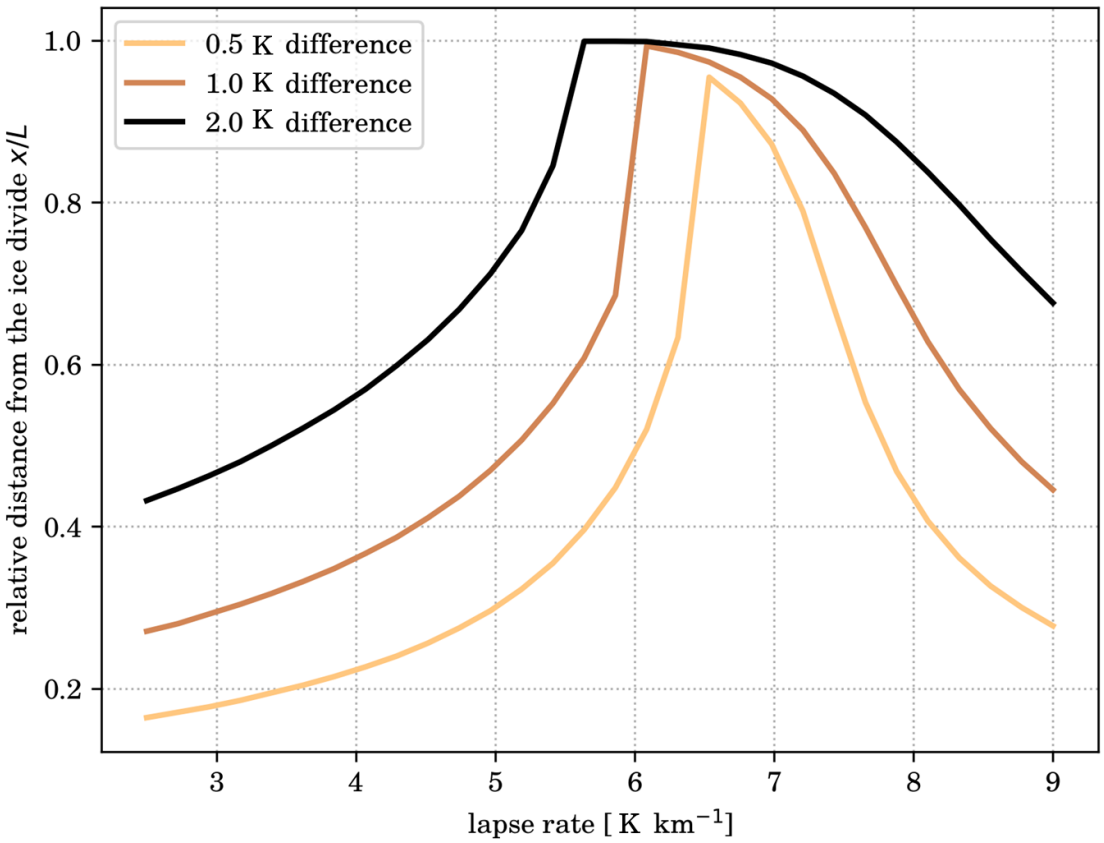

Figure 2.8: The basal temperature difference between the analytical solution and 2D numerical solution as a function of surface temperature lapse rate. The x-axis shows the range of lapse rates and the y-axis is the maximum normalized distance from the ice divide where the difference between the two solutions is less than defined temperature thresholds. At lapse rates lower than where the peak occurs, our model overestimates the basal temperatures and vice versa. $\dot{M}$ of 0.3 m yr^{-1} and G of 50 mW m^{-2} are used for simulations.

SIA as a power function. In the absence of horizontal velocities, the temperatures from the new analytical solution match those from the numerical solution with the exact SIA vertical velocity. The analytical solution incorporates an exponent, γ_+, which depends on surface mass-balance rate, $\dot{M}$, and thickness of the ice column, H. In order to use this solution, one must first calculate the vertical Péclet number as $Pe = \frac{\dot{M}H}{K}$ and use it to obtain γ_+ (equation 2.19). The value of γ_+ can be used to calculate the temperature profile using equation (2.17) and basal temperature can be obtained through equation (2.18). In order to include the strain heating in the analytical solution, the depth-integrated strain heating obtained from equation (2.22) can be added to the geothermal

heat flux at the bed (following Fowler, 1992).

The Péclet number includes the effects of two parameters that have an opposite effect on the temperature of an ice column: ice thickness has an insulating effect, so that thicker ice results in warmer temperatures at depth, while increase in surface mass-balance rate results in increased vertical advection of cold surface-ice, lowering the temperature at depth. According to equation (2.19), γ_+ increases with an increase in $\dot{M}$, and higher γ_+ results in warmer temperature profiles (Fig. 2.2). This may appear contradictory because surface mass balance acts as a cooling agent. However, the magnitude of γ_+ increases marginally with an increase in $\dot{M}$, while changes in ϕ and $\Gamma(\cdot,\cdot)$ in the analytical solution (equation 2.17) cancel the small increase in basal temperature due to increased γ_+. Therefore, the analytical solution is robust in capturing the thermal effect of increased vertical advection. This is evident in Fig. 2.9, where larger surface mass-balance rates reduce the difference between surface and basal temperature $T_s - T_b$, hence cooling the temperature profile, while the $T_b - T_s$ increases with an increase in ice thickness.

Note that at close proximity to ice divides (i.e., a few ice thicknesses) the basal shear stress becomes zero, violating SIA assumptions (Raymond, 1983) and having the consequence of inducing formation of a stagnant plug near the base under the divide. Also, it has been suggested that Glen's flow exponent near ice divides is close to 1 (Pettit & Waddington, 2003) which also results in lower rate of vertical advection of cold ice and leads to a warmer basal ice (Fig. 2.1, blue curves). Therefore, our analytical solution likely underestimates the basal temperatures in a region about $\sim$3-4 ice thicknesses away from ice divides for two separate reasons.

In all comparisons, the parameters of interest are kept uniform along the ice flow. This is certainly an over-simplification; surface mass balance clearly is not uniform on the ice sheet with higher rates near the margins than the interiors (e.g. Ettema et al., 2010), and spatial variations of geothermal heat flux (e.g. Fox Maule et al., 2009; Rezvanbehbahani et al., 2017) have been shown to significantly impact the velocity field of ice sheets (e.g. Larour et al., 2012a; Schlegel et al., 2015). Surface temperature lapse rate is also unlikely to be uniform along the surface of an ice sheet (e.g. Hanna et al., 2005; Erokhina et al., 2017), which can alter the ice sheet temperature

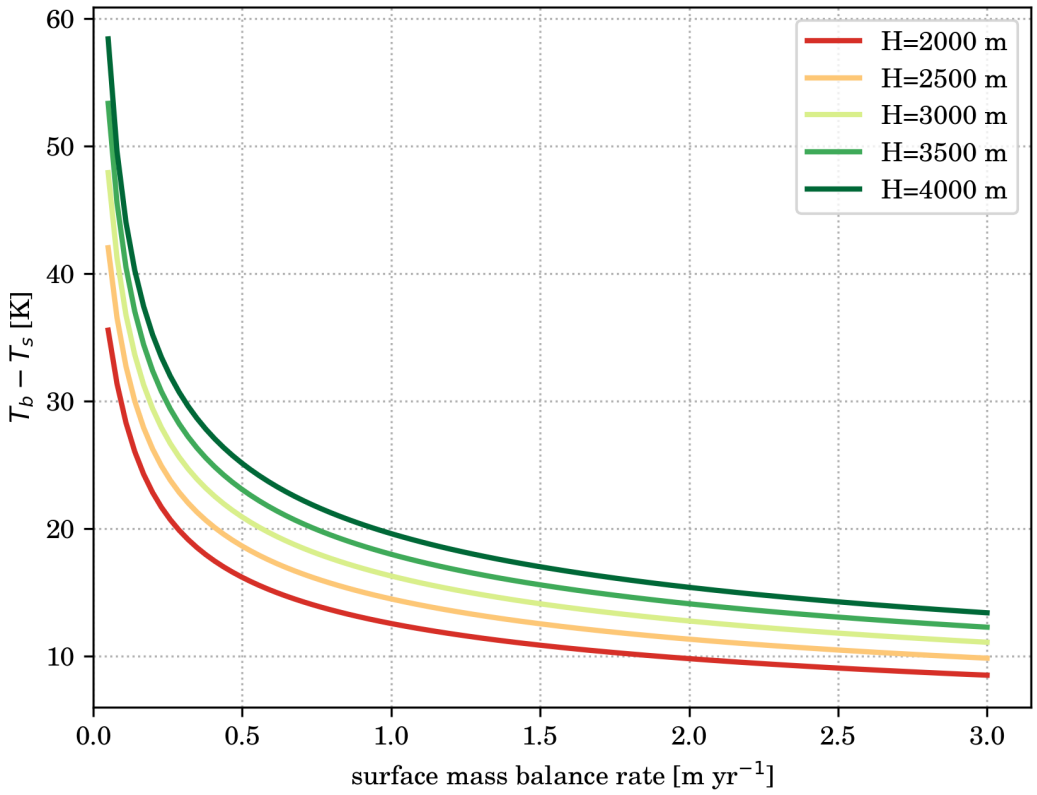

Figure 2.9: Difference between basal and surface temperature ($T_b - T_s$) from the analytical solution (equation 2.18) with respect to surface mass-balance rate at the ice divide for different thickness values.

distribution. In the present study, the Vialov profiles and the corresponding velocities are obtained from an ice-sheet-wide uniform rate factor, and the mechanical model is decoupled from the thermal model. The interaction between the flow regime and thermal field requires thermo-mechanical coupling which is not included and is beyond the scope of this study (see for example, Clarke et al., 1977; Dahl-Jensen, 1989; Greve & Blatter, 2016; Bondzio et al., 2017). Thermal coupling can also lead to stream formation and oscillations, (e.g., MacAyeal, 1993; Payne, 1995; Hindmarsh, 2009; Brinkerhoff & Johnson, 2015).

The goal of the presented comparisons with the 2D thermal model is not to mathematically quantify the effect of the horizontal advection term. Rather, our goal is to demonstrate the limitations of the 1D analytical solution in a simple 2D ice sheet profile and setting loose constraints

beyond which the solution cannot be applied. Evidently, even in these simplest cases quantifying the impact of horizontal advection is not straightforward. Despite these limitations, we delineate the interior regions of the Greenland and Antarctic ice sheets where the effect of horizontal advection and strain heating are likely less than 2 K compared with the analytical solution. In all the comparisons between the analytical solution and the 2D numerical solution shown in section 2.4, the horizontal surface velocity that corresponds to the location of a 2 K difference was more than 100 m yr^{-1}. Owing to all the simplifications associated with the 2D simulations, we chose a significantly more conservative range of 20 m yr^{-1} for the limit of 2 K offset in the analytical temperature solution. Also, as shown in section 2.3, strain heating can be incorporated in the analytical solution by adding the depth-integrated strain heating to the geothermal heat flux up to driving stresses of ∼50-60 kPa and produce basal temperatures within ∼2 K of the actual value. Therefore, the boundaries marked in Fig. 2.10 show the regions with both surface velocities less than 20 m yr^{-1} and driving stresses smaller than ∼60 kPa. Ice streams are excluded from the marked regions, because their inherent shelfy-stream characteristic (MacAyeal, 1989) makes horizontal advection the dominant heat transport mechanism.

Throughout this study, the surface temperatures are chosen sufficiently low so as to avoid melting of the basal ice. However, assessing whether basal ice is at the pressure melting point can be done using our solution, since one can solve for the heat flux in (2.18) that is required for the basal ice to reach the pressure melting point, G_{pmp}, as

$$G_{pmp} = \frac{(T_{pmp} - T_s)\kappa(\gamma+1)\,(-\phi)^{\frac{1}{\gamma+1}}}{\Gamma\left(\frac{1}{1+\gamma}, 0\right) - \Gamma\left(\frac{1}{1+\gamma}, -\phi H^{\gamma+1}\right)}. \tag{2.28}$$

The pressure melting temperature can be estimated by $T_{pmp} = 273.16 - \beta P$ where $P = \rho g H$ is the overburden pressure and β is the Clausius-Clapeyron constant of 9.8×10^{-8} kPa^{-1} (Cuffey & Paterson, 2010). If the sum of geothermal heat flux and strain heating close to the ice divide exceeds G_{pmp}, the melt rate, $\dot{b}$ can be estimated by

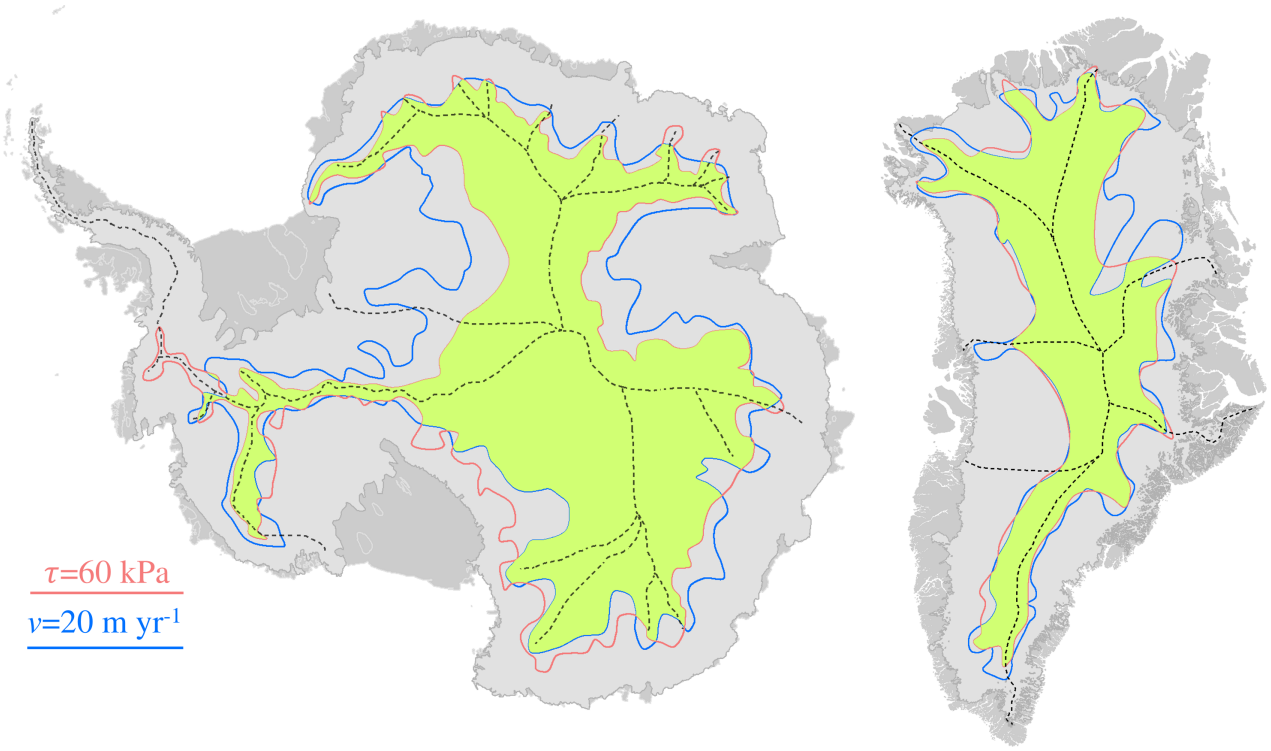

Figure 2.10: Approximate delineation of the regions where the analytical temperature solution can be used on the Greenland and Antarctic ice sheets with less than 2 K error (*green regions*). The boundaries mark the interior of both the driving stress of ∼60 kPa (*pink contour*) and surface velocity of 20 my yr^{-1} (*blue contour*). Greenland and Antarctic velocities are from Joughin et al. (2010) and Rignot et al. (2011), respectively. The driving stresses for Greenland and Antarctica are calculated from surface DEMs of Bamber et al. (2013) and Fretwell et al. (2013), respectively, and all parameters are resampled to 10 km spatial resolution.

$$\dot{b} = \frac{G + G_s - G_{pmp}}{L_f \rho}, \tag{2.29}$$

where L_f is the latent heat of fusion (see Table 1). This can be used as a first order approximation for assessing the thermal condition at the bed or find the minimum amount of heat required to thaw the bed, at the radar-detected locations with basal thaw (e.g. Oswald et al., 2018). If it is concluded that the bed is at the pressure melting temperature, frictional heating can be readily added to the geothermal heat flux as $G_{sliding} = \tau \times v_{sliding}$.

Finally, it is worth noting that according the results presented here, the Robin (1955) solution consistently underestimates the basal temperature. Therefore, the argument of the studies that have

used the Robin solution to show that the bed is near the pressure melting temperature (e.g. Siegert, 2000) remains valid (despite its underestimation of the basal melt rate). In contrast, the studies where the Robin solution has been used to demonstrate the presence of cold basal ice should be revisited.

2.6 Conclusion

We present a new analytical solution to the one-dimensional heat transport equation by parameterizing the vertical velocity profile as a power function. Temperatures from the analytical solution match numerical results obtained using vertical velocities derived from the SIA. We show that strain heating plays an important role in calculating the temperature profile of ice sheet interiors. We validate the approach suggested by Fowler (1992) that strain heating can be integrated at depth (G_s) and added to the geothermal heat flux at the bed. We show that with driving stresses of up to $\sim$50$-$60 kPa, the analytical solution with G_s overestimates the basal temperature by less than 2 K.

We evaluate errors in temperature estimates from the analytical solution arising from ignoring horizontal advection away from the ice divide, by calculating the offset between the analytical solution and two-dimensional temperature estimates of a Vialov profile. The comparison results depend on various parameters such as surface mass-balance rate, geothermal heat flux, and surface temperature lapse rate. Although the effect of horizontal advection terms is not included in the analytical solution, we show using numerical methods that the effect of horizontal advection on temperatures computed using the Vialov profile depends on various parameters including surface mass balance and surface temperature lapse rate. The effect of horizontal heat advection is more pronounced on the englacial temperatures, however, the basal temperatures from the analytical solution remain within 2 K for a large portion of the ice sheet length. Finally, we mark approximate boundaries where the new analytical solution can be used with less than 2 K error in Greenland and Antarctica. The analytical solution presented can be used to validate temperature calculations from numerical ice sheet models.

Chapter 3

Predicting the geothermal heat flux in Greenland: a Machine Learning approach[1]

[1]This chapter has been published as Rezvanbehbahani, S., Stearns, L. A., Kadivar, A., Walker, J. D., & van der Veen, C. (2017). Predicting the Geothermal Heat Flux in Greenland: A Machine Learning Approach. Geophysical Research Letters, 44(24), 12,271–12,279.

Abstract

Geothermal heat flux (GHF) is a crucial boundary condition for making accurate predictions of ice sheet mass loss, yet it is poorly known in Greenland due to inaccessibility of the bedrock. Here we use a machine learning algorithm on a large collection of relevant geologic features and global GHF measurements, and produce a GHF map in Greenland which we argue is within $\sim$15% accuracy. The main features of our predicted GHF map include a large region with high GHF in central-north Greenland surrounding the NorthGRIP ice core site, and hotspots in the Jakobshavn Isbræ catchment, upstream of Petermann Gletscher, and near the terminus of Nioghalvfjerdsfjorden glacier. Our model also captures the trajectory of Greenland movement over the Icelandic plume by predicting a stripe of elevated GHF in central-east Greenland. Finally, we show that our model can produce substantially more accurate predictions if additional measurements of GHF in Greenland are provided.

3.1 Introduction

Among the numerous input parameters needed to run ice sheet models, geothermal heat flux (GHF) is perhaps the least constrained by observations. GHF affects the ice temperature and viscosity, which can impact the ice sheet geometry and ice velocity (e.g. Larour et al., 2012a; Pittard et al., 2016; Seroussi et al., 2017). In addition, the origin of ice streams in both Greenland and Antarctica are commonly associated with locally elevated heat flow in the underlying bedrock (e.g. Fahnestock et al., 2001; Bell et al., 2007). Therefore, it is critical to have a robust estimate of the spatial distribution of GHF in the underlying bedrock.

For the Greenland Ice Sheet (GrIS), the GHF is largely unknown apart from a few ice cores where GHF is inferred from the temperature gradient in the basal ice layers. Two GHF models are frequently used for Greenland; one inferred from seismic tomography (Shapiro & Ritzwoller, 2004), and the other from magnetic anomalies (Fox Maule et al., 2009). These two models differ significantly from each other and suffer from numerous simplifying assumptions and unknown parameters in ice-covered areas. Additionally, applying either of these GHF models in numerical ice sheet models cannot reproduce the observed temperatures at ice core locations (Rogozhina et al., 2012). Given the importance of GHF, it is clear that a new and independent estimate should be constructed that honors both the ice core data as well as Greenland geology.

This study derives a new map of GHF for the GrIS using statistical relationships between global heat flux observations and the combined influence of local geology and regional tectonic setting. Compilations of global heat flux measurements on the continental crust include over 35,000 point measurements distributed across all continents. By assuming that GHF is a complex function of geologic and tectonic features (e.g. crustal thickness, magnetic anomaly, gravity field, rock type, age, elevation, proximity to spreading ridge), we construct a machine learning algorithm to obtain the statistical relationship between geologic features and GHF. Based on the obtained relationship, we predict the GHF for Greenland and discuss the relative importance of input parameters in obtaining the new GHF map.

3.2 Data

3.2.1 GHF measurements: global dataset

Global GHF data measured on the continents are obtained from the International Heat Flow Commission provided by the University of North Dakota (Gosnold, 2011). The data have a nearly-normal and unimodal distribution, with mean and standard deviation of 60.8 and 18.2 mW m^{-2}, respectively (Figure A.6). The spatial resolution of the data varies considerably; North America and Europe are extensively surveyed, while measurements are sparse in South America and Africa. We use the mean of GHF values within each 1 by 1 degree latitude-longitude cell, which reduces the number of points from 35,000 to more than 4,000 points. We apply a low pass filter to remove the short-scale spatial variability and highlight the large-scale spatial patterns of GHF that we are interested in predicting for Greenland.

Prior to applying the low pass filter, we limit our analysis to GHF values less than 200 mW m^{-2}, because even in Iceland (with an obvious mantle plume) the majority of heat flow measurements are below 200 mW m^{-2} (Hjartarson, 2015). Thus, we assume that for non-plume areas, such high readings are anomalous local processes (similar to Goutorbe et al., 2011) and are therefore removed to not contaminate our procedure.

3.2.2 GHF measurements: Greenland

There are only ten determinations of GHF in Greenland; five inferences from ice core sites and five direct bedrock measurements in ice-free coastal areas (Table A.1 and Figure A.7). GHF determinations at ice core sites usually mean that the GHF is inferred from the temperature gradient in the basal ice layer. GHF is also estimated using numerical ice sheet models by adjusting the GHF value at ice core locations so that the modeled basal temperature matches the measured basal temperature (e.g. Greve, 2005), or using a Monte Carlo simulation to inversely infer the GHF (e.g. Dahl-Jensen et al., 1998; Buchardt, 2009). Despite the uncertainties in these techniques, they form our current understanding of the GHF of the GrIS.

Table 3.1: Geologic datasets included in the feature vector for predicting GHF. The lithologies of Hartmann & Moosdorf (2012) and geologic provinces of Dawes (2009) are converted to the volcanic, sedimentary, and metamorphic rock types. Details are explained in Supplementary Material, section A.3 and Tables A.2 and A.3.

Variable Type	Variable Name	Reference
Continuous	Global surface topography	Amante & Eakins (2009)
	Greenland bedrock topography	Bamber et al. (2013)
	Depth to Moho	Reguzzoni et al. (2013)
	Lithosphere-asthenosphere boundary	Pasyanos et al. (2014)
	Age	Poupinet & Shapiro (2009)
	Bougeur gravity anomaly	Balmino et al. (2012)
	Crustal thickness	Laske et al. (2013)
	Upper mantle density anomaly	Kaban et al. (2004)
	Magnetic anomaly	Maus et al. (2007)
	Thickness of upper crust	Bassin (2000)
	Thickness of lower crust	Bassin (2000)
	Heat production provinces	Goutorbe et al. (2011)
Classification	Age of last thermotectonic event	USGS (1997)
	Upper Mantle velocity structure	Shapiro & Ritzwoller (2002)
	Rock type	Hartmann & Moosdorf (2012)
	Rock type (Greenland)	Dawes (2009)
Proximity	Distance to trench	Coffin et al. (1998) (UTIG Plates Project)
	Distance to transform ridge	Coffin et al. (1998) (UTIG Plates Project)
	Distance to young rift	Şengör & Natal'in (2001)
	Distance to volcano (5 nearest)	Goutorbe et al. (2011)
	Distance to ridge	Coffin et al. (1998) (UTIG Plates Project)
	Distance to hotspot	Caltech seismic lab (Anderson, 2016)

On the exposed rocks around the coast of Greenland, Sass et al. (1972) report GHF values of 37 and 41.8 mW m^{-2} in the southernmost part of Greenland. There is also one data point from Langseth et al. (1972) who measure the GHF at 51 mW m^{-2} in a fjord in south Greenland. In addition, the Greenland Analogue Project (GAP) reports two GHF measurements near Isunnguata Sermia in west Greenland of 27.2 mW m^{-2} (Meierbachtol et al., 2015) and 34.8 mW m^{-2} (Harper et al., 2011). Meierbachtol et al. (2015) do not report the exact location of their GHF measurements, therefore we use the average GHF value of these measurements (because the study domain of Meierbachtol et al. (2015) is small, the two GHF measurements certainly fall in the same 1 by 1 latitude-longitude cell), which reduces the total number of GHF points in Greenland to nine.

3.2.3 Geologic Features

In contrast to other efforts to estimate GHF in Greenland that use single geophysical features such as gravity anomaly (Shapiro & Ritzwoller, 2004) or magnetic anomaly (Fox Maule et al., 2009), we use a compilation of geologic features and information that are globally available on the continental crust (Table 1). These geologic features are grouped into three major categories (similar to Goutorbe et al., 2011): i) continuous data such as gravity anomaly and crustal thickness, ii) categorical data including rock type and classes of velocity structure of the upper mantle, and iii) proximity variables that describe the distance of each point to thermally active geologic features such as hotspots, ridges, and volcanoes. All geologic features are resampled to a 1 degree latitude-longitude grid using an ordinary kriging interpolation scheme.

3.3 Method

3.3.1 Overview of Statistical Models

The problem of predicting a continuous variable from a collection of relevant features is generally known as a regression problem. In our case, we wish to find a *predictor* that assigns a GHF value (denoted by $\widehat{GHF}$) to any point observation of geologic features. Performance of any such predictor is then evaluated by comparing its predictions to known GHF values. Such models are first *trained* on a set of point observations consisting of known values for geologic features and GHF, referred to as *training data*. The output of the training procedure is an optimal predictor which minimizes prediction error with respect to some cost function. The main model we present here for GHF prediction is Gradient Boosted Regression Tree (GBRT, Friedman, 2001) which has many desirable properties including ability to discover nonlinear statistical relationships, as well as handling both continuous and categorical features in the regression model, and stability (Friedman et al., 2001; Elith et al., 2008) (see Supplementary Material, section A.1 for general explanation of GBRT and section A.2.2 for our stability analysis of the model).

In order to assess the applicability of GBRT for GHF prediction, we compare its behavior to

two simpler regression models. First, we consider a linear regression model which we subsequently show to be inferior to GBRT. Second, since applying constant GHF values to numerical ice sheet models is still common in glaciology, we include a 'constant predictor' which simply predicts a spatially uniform GHF equal to the mean GHF value of its training data.

3.3.2 GHF prediction performance of GBRT

We use a standard cross validation scheme in which the entire data set is randomly partitioned into two disjoint sets: a *training set* used to find the optimal GHF predictor and a *validation set* on which the optimal predictor is evaluated. To quantify prediction performance we report two measures of error. First, we report the normalized root mean squared error (RMSE) between predicted $\widehat{GHF}$ and known GHF values in the validation set. Normalized RMSE is a standard and robust (invariant to rescaling) measure of error and is defined as

$$\text{Normalized RMSE} = \frac{1}{\langle GHF \rangle} \sqrt{\left\langle \left| GHF - \widehat{GHF} \right|^2 \right\rangle},$$

where $\langle \cdot \rangle$ indicates the average over the validation set. Normalized RMSE can be interpreted as a relative measure of error; for instance, an error of 0.15 can be understood as an average 15% relative error in predictions. Second, we report the r^2 of linear correlation analysis between $\widehat{GHF}$ and GHF on the validation set (see Supplementary Material, section A.2).

Using the above procedure with 80% of all data points for training and the remaining 20% for validation, GBRT predicts GHF with high accuracy (RMSE=0.14 and r^2=0.75), while predictions of the linear model have significantly higher error (RMSE=0.21 and r^2=0.40) as shown in Figure 3.1.

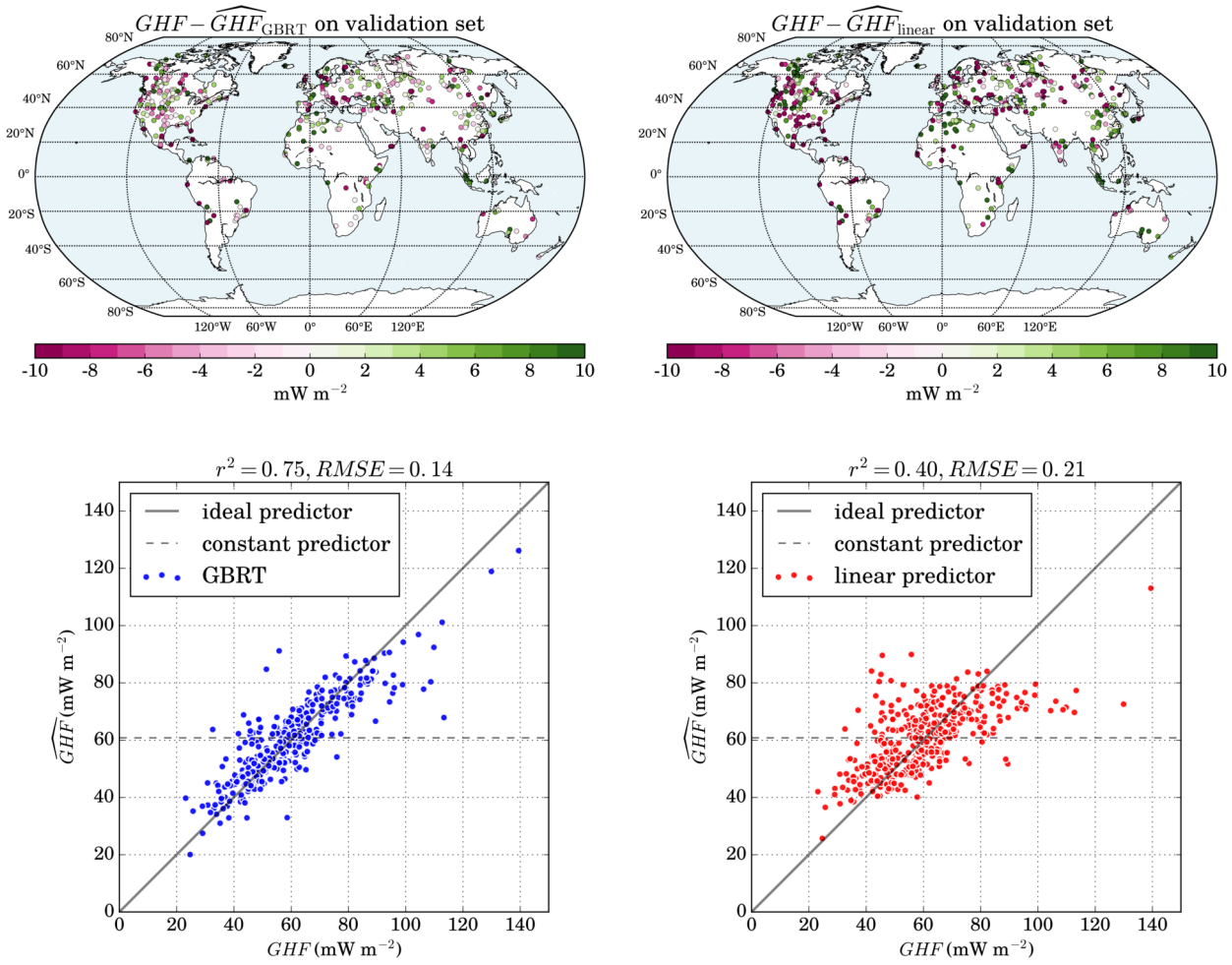

Figure 3.1: Performance of GBRT (left panels) and linear regression (right panels) when validation samples are distributed randomly. For each model, the difference between measurements and predictions $GHF - \widehat{GHF}$ (top panels), and linear correlation analysis between GHF and $\widehat{GHF}$ (bottom panels) are shown.

3.3.3 GHF prediction with limited local data

Since the goal of this work is to predict the heat flow specifically for Greenland, we investigate whether GBRT is capable of predicting GHF over a region with limited local data. We consider a region of interest (ROI) over which we wish to predict GHF. To quantify the abundance of local training data we define the notion of *local training density* for an ROI as:

$$\rho_{ROI} = \frac{\text{no. of training samples in ROI}}{\text{area of ROI}}.$$

We then pose our question regarding GHF prediction with limited local data as follows: given a ρ_{ROI} and a radius R, what is the expected error in GHF prediction over an arbitrary circular ROI of radius R?

We answer the above question by modifying the cross validation procedure described in the previous section. For a given ROI and a local training density ρ_{ROI} we randomly pick a subset of all available data points within the ROI as the local training set. These points together with all data points lying outside the ROI constitute the training set while the remaining samples within the ROI constitute the validation set (Figure 3.2). For each R and ρ_{ROI} we report the average value of normalized RMSE and r^2 over 50 random choices of ROI center in North America and West-Central Europe; the choice of these regions is due to the large number of GHF measurements that are located in these regions (see Supplementary Material, section A.2).

Using the above evaluation scheme we find that regardless of the location of the circle, GHF predictions have high RMSE ($\sim$0.25) and low r^2 values ($\sim$0.4) when all samples from the ROI are excluded from the training set (i.e. $\rho_{ROI} = 0$). This shows that GBRT performs poorly over a region with no local training data (top row in Figure 3.2). If an area is completely removed from the training procedure, GBRT cannot spatially extrapolate and predict GHF over an ROI with no local training data, highlighting the importance of regional geology and tectonics in predicting GHF. Therefore, we investigate the extent to which this reduction in prediction performance relates to the density ρ_{ROI} of training samples within the ROI as well as the ROI radius R.

We run two sets of experiments for assessing the local performance of GBRT; corresponding results for linear regression and constant predictors are also included for comparison. In the first set of experiments we fix the ROI radius $R = 1300$ km (size of Greenland) and vary ρ_{ROI} in each experiment from 5 to 50 samples per 10^6 km^2. Increasing ρ_{ROI} leads to lower RMSE and higher r^2 values for GBRT indicating increasing quality of prediction with increasing density of local training samples (Figures 3.2 and 3.3). Conversely, the linear model shows marginal reduction

in RMSE and insignificant increase in r^2 with increasing ρ_{ROI} (Figure 3.3). We conduct similar procedures for North America and West Europe separately and find near-identical trends in RMSE and r^2 (as in Figure 3.3) which shows that the model uncertainty does not depend on tectonic settings and local geology.

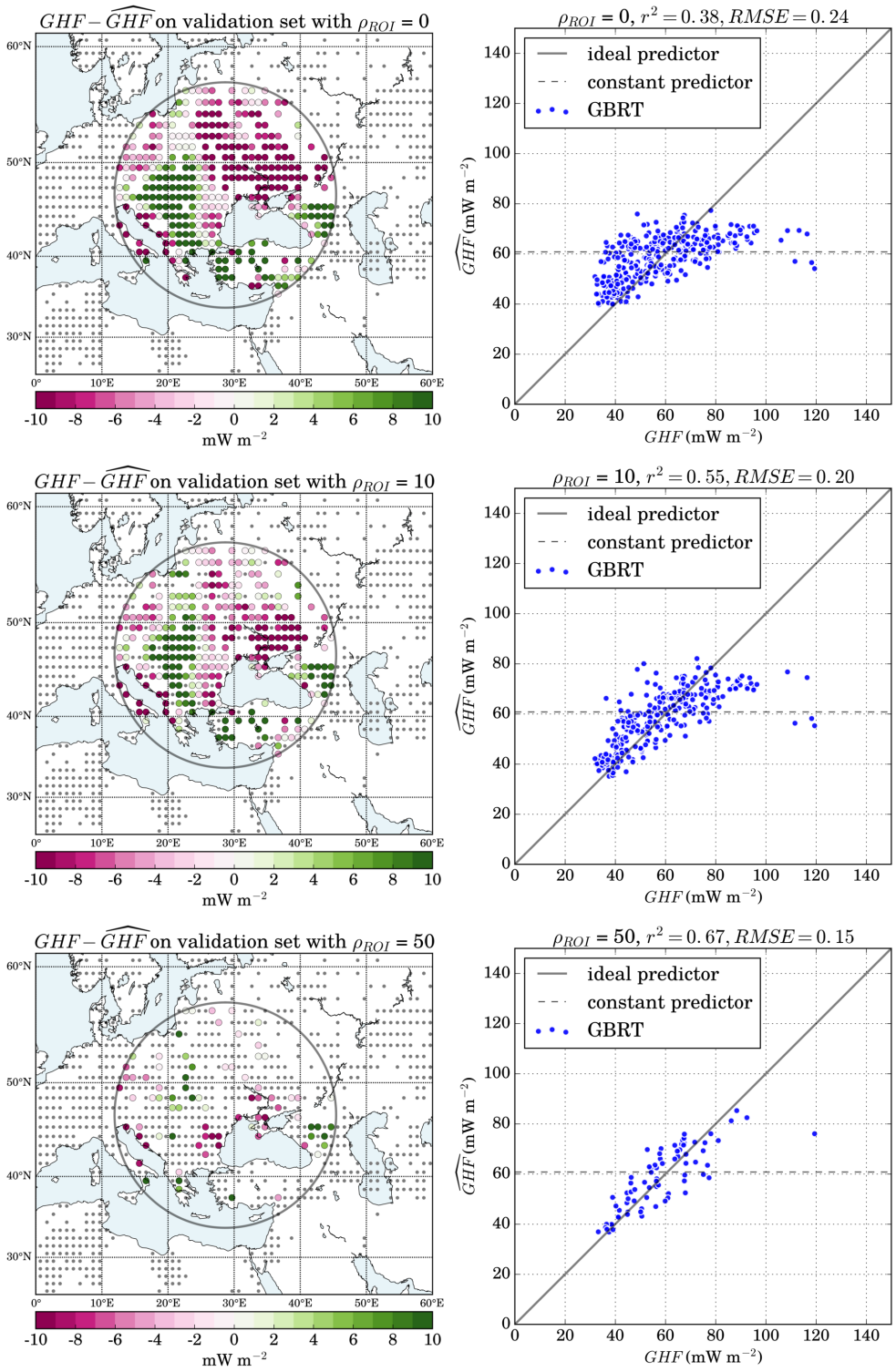

Figure 3.2: Step-wise improvement of GBRT predictions with increasing ρ_{ROI} shown over an arbitrary ROI of radius 1300 km. In each map grey dots indicate training data, colored dots indicate validation points, and the grey circle is the ROI. For three densities (0, 10, and 50 per 10^6 km^2) the difference between measurements and predictions (right panels) and their linear correlation (left panels) are shown.

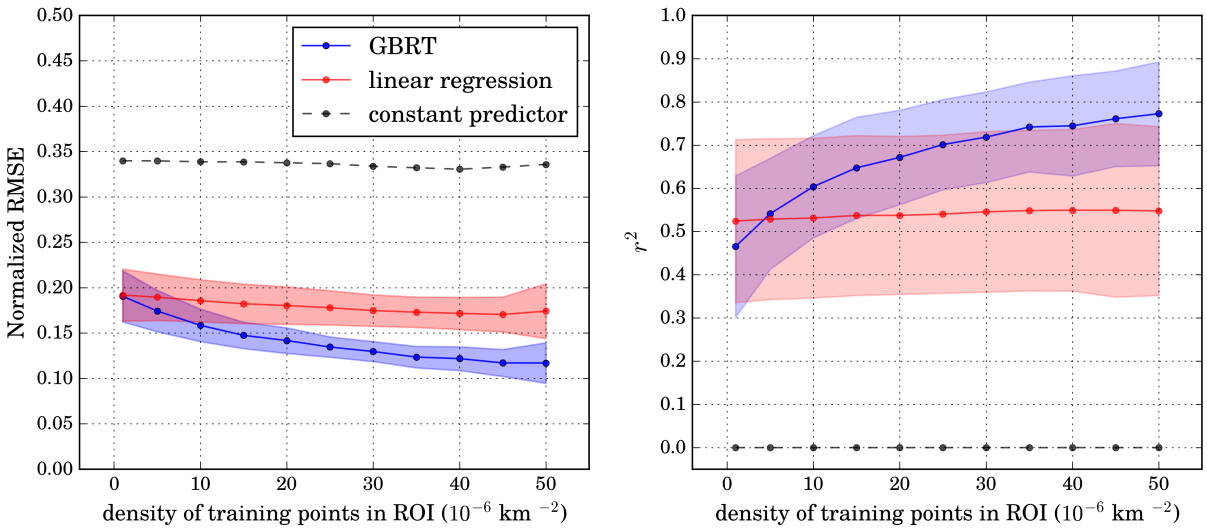

Figure 3.3: Normalized RMSE (left) and r^2 of linear correlation (right), for GBRT (solid blue lines), linear regression (solid red lines), and constant predictor (dashed black lines) for different densities. For each model and density, the cross validation procedure of Figure 3.2 is used and average errors on 50 ROIs of radius 1300 km are reported. The blue and red regions show one standard deviation.

In the second set of experiments, we fix the local training density $\rho_{ROI} \sim 10$ per 10^6 km^2 (corresponding to the availability of training samples in Greenland, see section 3.3.4) and vary the radius, R, of the ROI from 500 to 4000 km. Our results show that the RMSE of GBRT predictions remains unchanged with increasing values of R, while the corresponding r^2 continuously increases (Figure A.3). In both sets of experiments, our results strongly confirm that GBRT performs significantly better than linear regression for predicting GHF with limited local data.

3.3.4 GHF points for Greenland

There are only 9 direct GHF measurements/inferences in Greenland; with R=1300 km, these measurements roughly constitute ρ_{ROI}=2 per 10^6 km^2 on a 1 by 1 degree cell basis. With such sparse GHF measurements, our analysis shows that GBRT results in low r^2 values of 0.5 and RMSE of 0.2 (Figure 3.3). In order to compensate for the paucity of GHF points in Greenland, we assume that the regions surrounding each of the 9 direct measurements in Greenland can be represented by a Gaussian kernel of the form $GHF_x = GHF \times e^{-x^2/d^2}$ where GHF_x is the Gaussian-fit GHF

at distance x from the ice core location. We assume an influence radius of 150 km for GHF near ice cores. For all GHF measurements in Greenland, we use the large value of $d = 1000$ km which essentially results in a nearly planar distribution of GHF around the measurement location (e.g., $\sim$2% decrease within 150 km radius for 30 mW m^{-2} measurement, Figure A.7). The exception is at NorthGRIP ice core. Because the inferred GHF at NorthGRIP is anomalously high (Table A.1), we assume the high GHF is a very local process (see section 3.2.1) and thus we chose $d = 200$ km for the Gaussian kernel to make GHF drop more rapidly from high GHF values. By fitting the Gaussian kernel around ice cores, we increase the number of known GHF values in Greenland from 9 to more than 60 which is equivalent to ρ_{ROI}=11.3 per 10^6 km^2 for $R = 1300$ km. Based on the performance analysis shown in Figure 3.3, our GHF prediction for Greenland is expected to be within 15% of correct values (RMSE=0.15, r^2=0.6).

3.4 Results and Discussion

3.4.1 GHF prediction for Greenland

In order to train GBRT for predicting the GHF in Greenland, we include the entire global GHF dataset in addition to the points that we add for Greenland using the Gaussian kernel (Figure A.7). We perform the prediction for Greenland using three GHF values at the NorthGRIP ice core: Dahl-Jensen et al. (2003) estimate an upper and lower bounds of 160 and 90 mW m^{-2}, respectively, based on modeling the age of ice layers in radar echograms, and Greve (2005) calculates that the GHF of 135 mW m^{-2} is the GHF required to match the measured and modeled basal melt rate at the NorthGRIP site. The GHF predictions using these three GHF values at NorthGRIP are shown in Figure 3.4.

The predictions show that apart from the anomalously high heat flux near the NorthGRIP ice core, a relatively large northern region that spreads from the interior east and west has a similarly high GHF value. Changing the magnitude of the prescribed GHF at the NorthGRIP ice core location alters the magnitude of predicted GHF in this region, but the spatial pattern and extent remain

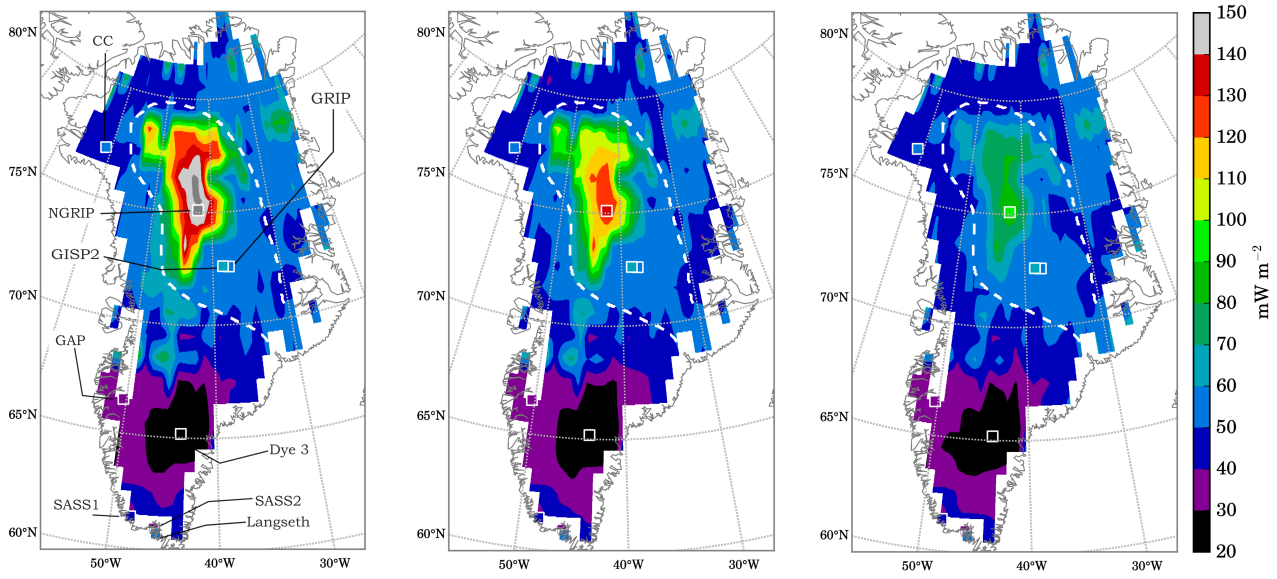

Figure 3.4: GHF predictions of GBRT for Greenland. Direct GHF measurements from the coastal rock cores, inferences from ice cores, and additional Gaussian-fit GHF data around ice core sites are used as training samples within the ROI leading to ρ_{ROI} = 11.3 per 10^6 km^2. Predictions are shown for three different values prescribed at NorthGRIP: 160 mW m^{-2} (left) as the upper limit (Dahl-Jensen et al., 2003), 135 mW m^{-2} (middle) suggested by Greve (2005), and 90 mW m^{-2} (right) as the lower range suggested by Dahl-Jensen et al. (2003). The white dashed region roughly shows the extent of elevated heat flux and a possible trajectory of Greenland's movement over the Icelandic plume.

unchanged.

Our model predicts a region with relatively low GHF in south Greenland, which is consistent with the GHF measurements and age of the North Atlantic Craton. The extent of this low heat flux region (GHF values less than 40 mW m^{-2}) corresponds well with the suggested extent of the North Atlantic Craton (Dawes, 2009, Fig. 1). In addition, GHF measurements across the Labrador Sea, on the Canadian region of the North Atlantic Craton show low GHF values of about 25 mW m^{-2}, comparable to our predictions in south Greenland (Mareschal & Jaupart, 2004, Fig. 4).

There are a number of distinguishable features in our predicted GHF map. First is the slightly-elevated predicted GHF which forms a path from northwest to central-east Greenland (white dashed line in Figure 3.4). This path closely follows the span of Icelandic plume tracks suggested by Rogozhina et al. (2016, Fig. S8). Other notable features are the two pockets of high GHF in central-west Greenland, which persist regardless of the choice of GHF for NorthGRIP. This region

is at the center of the catchment that is drained by Jakobshavn Isbræ. It is important to note that there are no GHF measurements/observations in this region. The closest GHF measurement is the location of the GAP project (Harper et al., 2011) which has a low GHF of 30 mW m^{-2}. Similar regions of elevated GHF exist in the northeast region, close to the margin of the ice sheet, near the terminus of Nioghalvfjerdsfjorden (79North). There is no nearby GHF measurement in this region either, and therefore, these predictions are independent of the prescribed GHF values in Greenland.

3.4.2 Interpretation of GBRT predictions

A standard technique in probing additive models is to first take the total amount of reduction in prediction error provided by each feature as its importance in an individual tree. Then the average error reduction over all trees provides a relative measure of importance for each feature (see Supplementary Material section A.3.1). Our model predicts topography, distance to young rifts, distance to trench, depth of lithosphere-asthenosphere boundary, and depth to Moho as the top five important features, respectively (Figure A.5).

The relative importance of the top 10 features are very close to each other which hinders a straightforward association of the observed GHF patterns to individual geologic features. Furthermore, summarizing the importance of each feature in a single number will mask the importance of features that are somehow correlated with each other. In our feature vector, for example, distance to volcanoes is likely correlated with distance to hotspots and rifts. Including strongly correlated features in the feature vector only marginally improves the model performance, but the relative importance of correlated features will get distributed (Figure A.5). A robust interpretation or simplification of the GBRT model presented here is beyond the scope of current study and is a potential avenue for future work (see Supplementary Material, section A.3.2).

3.5 Conclusion

Using the Gradient Boosted Regression Tree (GBRT) algorithm, we present a robust statistical relationship between a large group of geologic and tectonic features and global GHF. We combine the global GHF measurements on the continental crust with GHF inferences from ice cores, and few available GHF measurements on exposed coastal rock in Greenland and train GBRT to predict the GHF for the entire unsurveyed land mass of Greenland.

Our predicted GHF map shows a notable contrast between the regions south and north of $\sim 67^{\circ}$ with south having significantly lower GHF than north. The GHF map predicts a large region with high GHF in central-north Greenland close to the NorthGRIP ice core site, where other studies suggest thin lithosphere and trajectory of crust movement over the Icelandic plume as the cause of elevated GHF. This trajectory is also captured by our model in central-east Greenland. Finally, our GHF map shows slightly elevated GHF in central-west Greenland (upstream of Jakobshavn Isbræ), near the terminus of Nioghalvfjerdsfjorden in northwest, and small pockets in the northern regions.

The model's performance evaluation shows that the performance of GBRT will be significantly improved if any additional GHF measurements become available in Greenland, and thus, resolve the need for logistically expensive field measurements for the entire ice sheet.

Chapter 4

Constraining the geothermal heat flux in Greenland: comparing ice cores, radar observation, and numerical models

Abstract

The spatial distribution of temperate ice is a critical parameter for numerical ice sheet models. Current estimates of the basal melt distribution beneath the Greenland Ice Sheet (GrIS) contain large uncertainties due to poorly constrained boundary conditions, primarily from geothermal heat flux (GHF). Several methods have been developed that estimate the GHF for Greenland. However, these GHF models often contradict each other and implementing them in numerical ice sheet models cannot reproduce the measured temperatures at ice core locations. In this study, we utilize two radar datasets that detect basal water in Greenland to constrain the GHF at regions with a thawed bed. Using the three-dimensional ice sheet model SICOPOLIS, we iteratively adjust the GHF to find the minimum heat flux required to reach the bed to the pressure melting point, GHF_{pmp}, at locations of radar-detected basal water. We identify parts of the central-east, south, and northwest regions that have significantly high GHF_{pmp}. Conversely, we find that the majority of low-elevation regions of west Greenland and parts of northeast have very low GHF_{pmp}. We compare the estimated constraints with the available GHF models for Greenland and ice core information and show that the majority of GHF models do not satisfy the estimated constraints. Our results highlight the need for community effort to reconcile the discrepancies between radar data, GHF models, and ice core information to better constrain the basal thermal state of the GrIS.

4.1 Introduction

Basal ice temperature plays an important role in controlling ice velocity and consequently, ice sheet geometry and discharge. If basal ice is at the pressure melting point, basal water is generated, which can enhance the sliding velocity. At temperatures lower than the melting point, ice temperature affects ice stiffness and deformational velocity. Therefore, estimating the basal temperature of ice sheets is critical for generating realistic results using numerical ice sheet models. However, our current knowledge of basal temperature is poorly-constrained by observations and *in situ* measurements.

The amount of heat generated at the base of an ice sheet governs the basal ice temperature. This heat can derive from three major sources: heat generated from the internal deformation of ice, heat produced from the friction of ice with the glacier bed, and geothermal heat flux from the Earth's interior (GHF). The effect of each of these components on basal conditions varies spatially, primarily based on ice thickness, velocity, and tectonic setting. Among these sources, GHF has the largest uncertainty range; apart from a handful of deep ice cores, direct measurements of GHF are not available under the ice sheet.

The importance of spatial variations in GHF on subglacial hydrology and ice sheet dynamics has been discussed in several studies (e.g. Larour et al., 2012a; Rogozhina et al., 2012; Pittard et al., 2016). Modeling studies show that GHF not only affects the basal thermodynamic condition but also alters the thickness and surface geometry of ice sheets (Greve & Hutter, 1995; Larour et al., 2012a). Therefore, understanding the spatial distribution of GHF is important for enhancing the robustness of ice sheets models.

At ice core locations, GHF can be inferred from the measured vertical temperature gradient in the basal ice layer and the thermal conductivity of ice.Measurements from ice cores reveal large variations in GHF over short distances in the Greenland Ice Sheet (GrIS). For example, the estimated GHF from the NGRIP ice core ($\sim$140 mW m^{-2}, Dahl-Jensen et al., 2003) is more than 50% higher than GHF measurements at the GRIP ice core, located roughly 300 km away (51.3 mW m^{-2}, Dahl-Jensen et al., 1998). In addition, GHF estimates at the onset of the Northeast Greenland

Ice Stream (NEGIS) are possibly an order of magnitude higher than at the GRIP ice core, only 200 km away (Fahnestock et al., 2001). In south Greenland, at the location of the Dye 3 ice core, the modeled GHF suggests low values of roughly 20 mW m^{-2} (Gundestrup & Hansen, 1984; Greve, 2005). At the base of paleo ice sheets, radiometric measurements from till and glacially eroded bedrock reveal GHF values that range from 30 to 83 mW m^{-2} over distances less than 100 km (Naslund et al., 2005). Although spatial variations in GHF are shown to have significant effects on the thermodynamics of basal ice, they remain largely unknown in Greenland.

Direct measurements of GHF of the GrIS are limited to a few deep ice core sites. To overcome this limitation, several methods have been developed to predict the spatial patterns of GHF. For example, Fox Maule et al. (2009) use remotely-sensed magnetic data to calculate the Curie depth, from which the GHF can be inferred (Fig. 4.1a). The analysis of magnetic data is advanced by Martos et al. (2018) who use spectral analysis to estimate depth of Curie isotherm in Greenland from high resolution magnetic anomaly data (Fig. 4.1b). Recently, Rezvanbehbahani et al. (2017) train a machine learning algorithm by combining the global GHF measurements and geologic and tectonic properties to predict the GHF in Greenland (Fig. 4.1c). In addition, seismic tomography models, based on structural similarity functionals, are used to estimate the global GHF (Shapiro & Ritzwoller, 2004) (Fig. 4.1d), and Greve (2005) modifies the empirical GHF estimates of Pollack et al. (1993) to match the modelled and measured basal temperatures in Greenland ice cores.

Seismic and magnetically-derived maps of Shapiro & Ritzwoller (2004) and Fox Maule et al. (2009) have been used in thermomechanical ice sheet models to estimate the basal temperature of the GrIS (e.g. Larour et al., 2012a; Rogozhina et al., 2012; Seroussi et al., 2013); however, the calculated basal temperatures often do not match deep ice core measurements. Using spatially uniform GHF values in numerical ice sheet models may yield more accurate results for surface elevation reconstructions and temperature profiles at ice core sites than other GHF models (e.g. Rogozhina et al., 2012). Consequently, applying a spatially uniform GHF for GrIS is still common in modeling studies.

Radar surveys are pivotal in identifying regions with temperate bed or ponded water. Basal

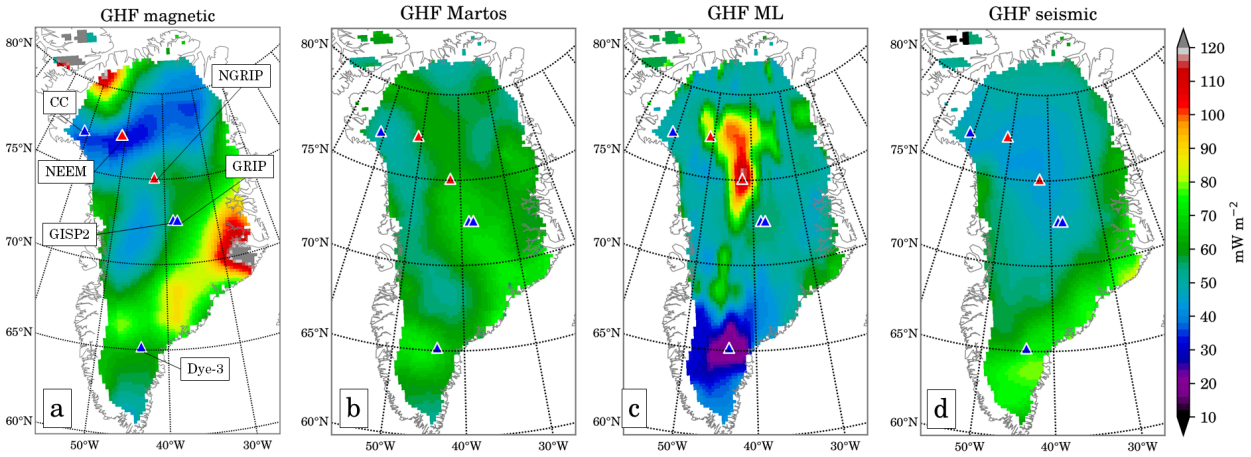

Figure 4.1: The GHF maps that are used in this study from (a) Fox Maule et al. (2009), (b) Martos et al. (2018), (c) Rezvanbehbahani et al. (2017) (ML refers to machine learning), and (d) Shapiro & Ritzwoller (2004). The fifth GHF map is spatially uniform GHF of 56 mW m^{-2}. Ice cores sites are shown with triangles with blue and red colors indicating observed frozen and thawed basal conditions, respectively. The Camp Century ice core is denoted by CC.

water or temperate bed is not explicitly a boundary condition in modeling ice sheet behavior. However, the existence of basal temperate ice sets an important constraint on the thermal boundary condition of the bed; it implies that the GHF must be larger than a critical value below which the bed would be frozen (referred to as GHF$_{pmp}$). Therefore, numerical ice sheet models can implement the spatial distribution of radar-detected basal water to estimate GHF$_{pmp}$. Such results are necessary to evaluate the reliability of current GHF models.

This study seeks to improve our understanding of basal thermal conditions of the GrIS by constraining the spatial variations of GHF according to the extent of thawed basal state, predicted by radar data. We use two datasets that independently predict the location of basal melt or frozen bed of the GrIS. The first dataset is from Oswald et al. (2018) where they use the reflection intensity of radar signals (Oswald & Gogineni, 2008) to delineate regions where subglacial water likely exists. This dataset identifies thawed regions with substantial basal water thickness ($\sim$3 cm). The second dataset is from Jordan et al. (2018), who use a "bed-echo reflectivity variability" method to detect wet-dry transitions in the basal material. Both datasets are purely based on radar data and are independent of numerical or GHF models. Note that in both datasets, not detecting temperate ice

or ponded water at the bed does not imply that the bed is frozen. In other words, the implemented criteria to determine the basal condition is a necessary condition, but not sufficient.

Here we use the three-dimensional thermomechanical ice sheet model SICOPOLIS (Greve & Hutter, 1995; Greve, 1997) to iteratively estimate the GHF at locations where basal water is detected. By adjusting the value of GHF at thawed points, we constrain the GHF of the ice sheet so that the basal condition matches the predictions of both of these radar studies. We then compare the GHF_{pmp} values with the available GHF maps in Greenland, namely, magnetically derived (Fox Maule et al., 2009, MAG), seismically derived (Shapiro & Ritzwoller, 2004, SEIS), machine learning-based (Rezvanbehbahani et al., 2017, ML), and the GHF from spectral analysis of high resolution magnetic data (Martos et al., 2018, MAR).

A similar approach has been conducted by Van Liefferinge & Pattyn (2013) and Van Liefferinge et al. (2018) in order to identify the possible locations with a frozen bed in East Antarctica in search for the oldest ice. Because the regions that are investigated in those studies are in the interior regions of East Antarctica (with balance velocities less than 2 m yr^{-1}), vertical 1D models would suffice. However, because some of the regions of interest in our study are near the margins, the effect of horizontal heat advection and thermo-mechanical coupling becomes important and a 3D model is necessary.

The structure of this study is as follows: we first introduce the thermal component of the numerical ice sheet model, SICOPOLIS, which is used to perform the simulation (section 4.2.1). Then, we explain the two radar datasets of Oswald et al. (2018) and Jordan et al. (2018) (section 4.2.2), followed by the description of simulation set up (section 4.2.3). We present the results of adjusting the GHF at the locations of radar-detected basal water in section 4.3.1 and 4.3.2 and compare the estimated constraints and the GHF models in section 4.3.4. We then discuss the uncertainty of the estimates, as well as an in-depth comparison with ice core data (section 4.4). Finally, we investigate the importance of such constraints on the total melt-water production at the base of the ice sheet (section 4.4.2).

4.2 Data and Methodology

4.2.1 Ice sheet model

We use the SImulation COde for POLythermal Ice Sheets (SICOPOLIS version 3.3) to iteratively solve for GHF. SICOPOLIS simulates the dynamic and thermodynamic evolution of ice sheets using the Shallow Ice Approximation (SIA, Hutter, 1983). Glacier ice is treated as a heat-conducting incompressible fluid with power-law rheology (Glen, 1955), modified to compensate for infinite viscosity at the ice surface (Greve & Blatter, 2009). Given a time-dependent external forcing (climate conditions), SICOPOLIS simulates the temporal evolution of ice thickness, temperature, and velocity field. The thermodynamic schemes in SICOPOLIS allows for tracking the cold-temperate transition surface (CTS). Because our focus is the thermal model in SICOPOLIS, we present the fundamental equations for energy conservation and thermal boundary conditions. Mathematical details of SICOPOLIS are explained in detail in Greve & Hutter (1995) and Greve (1997).

4.2.1.1 Thermal model

We model the thermal evolution of GrIS using the enthalpy method (e.g. Aschwanden et al., 2012). This method has the advantage of including temperature and water content in a single thermal enthalpy parameter, h. The specific enthalpy is a function of temperature, T, and water content, W, and is written as:

$$h(T,W) = \int_{T_0}^{T} c(\hat{T})d\hat{T} + LW, \tag{4.1}$$

where L is the latent heat of fusion (3.35×10^5 J kg^{-1}) and $T_0 = 273.15$ K. For cold ice $W = 0$, and at CTS, where ice is at the pressure melting point, the enthalpy becomes only a function of T_{pmp} (which is itself a function of overburden pressure, N_b), hence,

$$h_{pmp}(T_{pmp}, W = 0) = \int_{T_0}^{T_{pmp}} c(\hat{T})d\hat{T} \tag{4.2}$$

and T_{pmp} is calculated as $T_{pmp} = T_0 - \beta N_b$, with $\beta = 9.8 \times 10^{-8}$ K Pa^{-1} the Clasius-Clapeyron constant. The overburden pressure is calculated through the conventional equation, $N_b = \rho g H$, with g the gravitational acceleration of 9.81 m s^{-2}, H as the ice thickness, and ice density $\rho = 910$ kg m^{-3}.

By knowing the specific enthalpy, one can calculate T and W through

$$T = \begin{cases} T(h), & h < h_{pmp} \\ T_{pmp}(N_b), & h \geq h_{pmp}, \end{cases} \tag{4.3}$$

$$W = \begin{cases} 0, & h < h_{pmp} \\ \frac{h - h_{pmp}}{L}, & h \geq h_{pmp}. \end{cases} \tag{4.4}$$

Similar to balance laws for temperature, the balance equation for enthalpy can be written as

$$\frac{\partial h}{\partial t} = -\vec{v}.\nabla h + \frac{\partial}{\partial z}\left(k_{c,t}\frac{\partial h}{\partial z}\right) + \frac{Q}{\rho} \tag{4.5}$$

where the enthalpy diffusivity for cold ice is $k_c = \frac{\kappa}{\rho c}$ and for temperate ice is $k_t = \frac{\nu}{\rho}$ with ν the diffusivity of water in temperate ice. In equation (4.5), $\vec{v}$ denotes the three dimensional velocity field and diffusion is assumed significant only in the vertical z-direction. Strain heating is denoted by Q and is calculated as the trace of the product of the Cauchy stress tensor and effective strain-rate tensors.

At the CTS, the temperature and enthalpy of cold (denoted by a '+' superscript) and temperate zones (denoted by a '−' superscript) must be equal due to continuity considerations. Therefore,

$$h^+ = h^- = h_{pmp}. \tag{4.6}$$

Similar to temperature gradients at the CTS, normal enthalpy gradients must also be equal in cold and temperate zones, therefore the continuity of sensible heat flux reads

$$\nabla h^{+} \cdot \mathbf{n} = \nabla h^{-} \cdot \mathbf{n}. \tag{4.7}$$

At the surface of the ice sheet, temperature is applied as a constant Dirichlet-type boundary condition and at the base, GHF is included as a constant Neumann-type heat flux. A Weertman-type sliding law is implemented everywhere in the basal layer. At regions with a frozen bed, sub-temperate sliding is introduced following Hindmarsh & Le Meur (2001). The applied sliding relation reads

$$v_b(T_b) = -C_b \exp(\frac{T_b}{\gamma}) \frac{\tau^p}{N_b^q}, \tag{4.8}$$

where p and q are sliding parameters chosen as 3 and 2, respectively. Basal temperature relative to the pressure melting point is denoted by T_b, C_b is the sliding coefficient, $\gamma = 1^{\circ}$C is the sub-melt-sliding parameter, and basal drag is shown by τ_b. Sub-temperate sliding is added to avoid singularity in calculation of velocity field at the transition between frozen and thawed bed regions. Frictional heating is included in the thermal boundary condition as the product of sliding velocity and basal shear stress (which in the case of SIA equals the driving stress).

In order to simulate the thermal evolution of the ice sheet, we follow the one-layer melting-CTS enthalpy scheme of SICOPOLIS. This approach utilizes the CTS boundary condition (equation 4.7) by enforcing it explicitly on the upper most temperate layer of any ice column that contains CTS. For details of this method see Blatter & Greve (2015) and Greve & Blatter (2016).

We use a spatial resolution of 20 km which leads to a grid of 140 $\times$ 82 in the stereographic plane. Sigma coordinates are used in the vertical direction (z) and the cold ice-column is mapped into [0,1] intervals and discretized by 81 vertical grid points. For modeling the thermal conduction in underlying bedrock we use 41 layers in the thermal lithosphere. The creep enhancement factor is chosen as a constant value of 1 for Holocene ice ($<$11 ka) and 3 for Pleistocene ice ($>$11 ka) (similar to Greve, 2005; Rogozhina et al., 2012). The rest of the physical parameters are the same as those of Greve & Herzfeld (2013, Table 1). Since the simulations are not in steady-state condi-

tion, a model for the glacial isostatic adjustment must be included to simulate the changes in bed elevation due to changes in the ice load. We use the Local-Lithosphere-Relaxing-Asthenosphere model (LLRA) with a time lag of 3000 years for relaxing the asthenosphere (following Le Meur & Huybrechts, 1996).

4.2.1.2 Paleoclimate set-up

Input parameters to the model include average annual and monthly surface temperatures, annual surface mass balance, global sea level, and GHF. Paleoclimate temperature variations across the ice sheet are modelled by implementing a time-dependent temperature anomaly function $\Delta T(t)$, such that

$$\begin{aligned} T_{\mathrm{ma}}(S,\phi,\lambda,t) &= T_{\mathrm{ma}}^{\mathrm{present}}(S,\phi,\lambda)+\Delta T(t), \\ T_{\mathrm{mj}}(S,\phi,\lambda,t) &= T_{\mathrm{mj}}^{\mathrm{present}}(S,\phi,\lambda)+\Delta T(t) \end{aligned} \tag{4.9}$$

where T_{ma} and T_{mj} represent present-day's mean annual and July temperatures (from Fausto et al., 2009); ϕ and λ denote latitude and longitude, respectively, and S is the surface elevation of the ice sheet. Temperature anomaly function is reconstructed using δ^{18}O records from the NorthGRIP ice core since the last interglacial at -120 ka until -4 ka (Andersen et al., 2004). The time series is extended to the previous glacial maximum at about -140 ka by ΔT linearly decreasing to -20°C. From -4 ka to present the parameterization of Kobashi et al. (2011) the GRIP ice core is used (Dansgaard et al., 1993). The climate anomaly function is shown in Fig. 4.2 and is spatially uniform. For global sea level history, we use the reconstruction from the SPECMAP marine δ^{18}O records provided by Imbrie et al. (1984).

4.2.2 Datasets for radar-detected basal thaw

The spatial distribution of the basal thermal state is determined from two sources. The first dataset from Oswald et al. (2018, hereafter OSW) is essentially based on the character of reflected radar signals from the ice-bed interface (after Oswald & Gogineni, 2008). Basal state determinations

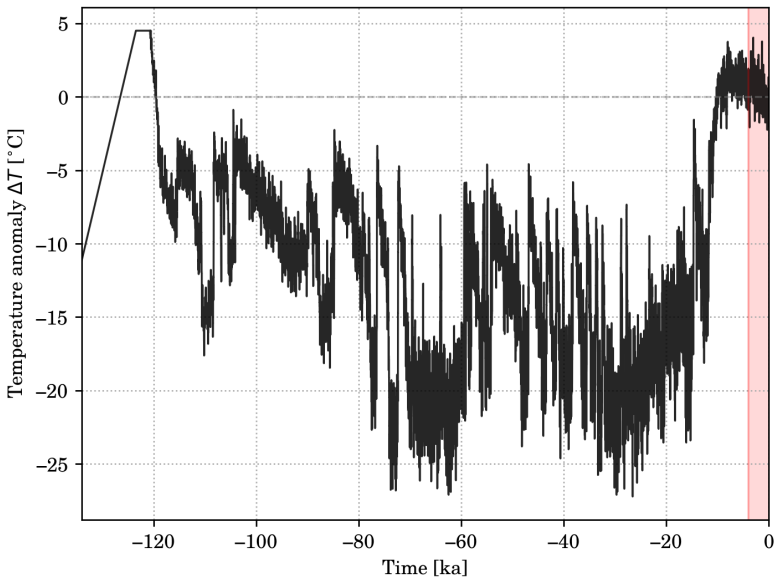

Figure 4.2: Time series for the temperature anomaly (ΔT) used in equation (4.9). The last 4 ka years (marked by light-red region) are reconstructed from Kobashi et al. (2011) while the rest of the anomaly is from the NorthGRIP ice core δ^{18}O records (Andersen et al., 2004).

based on radar data (provided by Center for Remote Sensing of Ice Sheets, CReSIS during 1999-2003; Gogineni et al., 2001) are made approximately every 200 m along each radar flight line; melt detections are separated along the flight path by one ice thickness and the conditions for melting are assumed to be effectively continuous between melt detections. Circles are then drawn on the effectively continuous melting or frozen path segments, and an assumption of isotropy of the basal state distribution is used to infer the probable state across the flight path. This means that determinations from neighboring flight paths can be used in support of interpolated basal states and the effect of random detection errors is minimized. This technique allows for larger scale interpolation of the basal state of the ice, as opposed to narrow radar flight paths. The detected basal water using this method represents 'ponded' basal water that is thicker than $\sim$3 cm. The rest of the regions could be frozen or temperate with a thinner layer of basal water. The spatial distribution of basal 'ponded water' from Oswald et al. (2018) is shown in Fig. 4.3a.

The second dataset is from Jordan et al. (2018, hereafter JOR) who develop a new diagnostic method for inferring basal thermal state from radio echo sounding data. Their method, termed

"bed-echo reflectivity variability", combines reflectivity with additional metrics such as specularity and bed-echo abruptness to identify the locations where rapid transition between wet-dry bed occurs. Jordan et al. (2018) show that their method is not affected by spatial variability in attenuation and can be adjusted to be used with different radar systems employed in different Operation IceBridge surveys. They interpret their results as 'basal water distribution' and every pick corresponds to a circle with 5 km diameter as the effective resolution of their method (Jordan et al., 2018, Fig.). The spatial distribution of basal water from Jordan et al. (2018) is shown in Fig. 4.3b.

In order to apply the scattered points from the two datasets into a 20 km SICOPOLIS grid, we cluster all the individual picks from both studies with an aggregate distance of 100 km to represent data in a spatial 2D domain (rather than individual points along flight tracks). Then, the nodes from SICOPOLIS grid points that fall within the created polygons are chosen as the targeted thawed points in SICOPOLIS. This method over-interprets the locations of basal water, since not all the radar points in a 20 km pixel are necessarily inferred to be thawed. The uncertainties associated with such interpretation are discussed in section 4.4.

The focus of this study is to set constraints on the GHF based on the spatial distribution of thawed or frozen beds, predicted by these two studies. Assessing the causes of the observed differences between the two datasets is beyond the scope and aim of the current work. However, it is worth mentioning that since the absence of thaw determination in neither of these datasets indicate a frozen bed, they are not mutually exclusive. Therefore, their differences are not necessarily contradictions; they rather show the strength or weakness of one of the radar techniques compared to the other.

4.2.3 GHF adjustment and simulation setup

In numerical ice sheet models, GHF is applied as a boundary condition to the thermal model, which itself is strongly tied to the mechanical model. Therefore, inversion for GHF in thermo-mechanically coupled ice sheet models is very challenging. Studies have attempted to formulate and solve the inverse problem for GHF (e.g. Zhu et al., 2016). However, their analysis is limited to

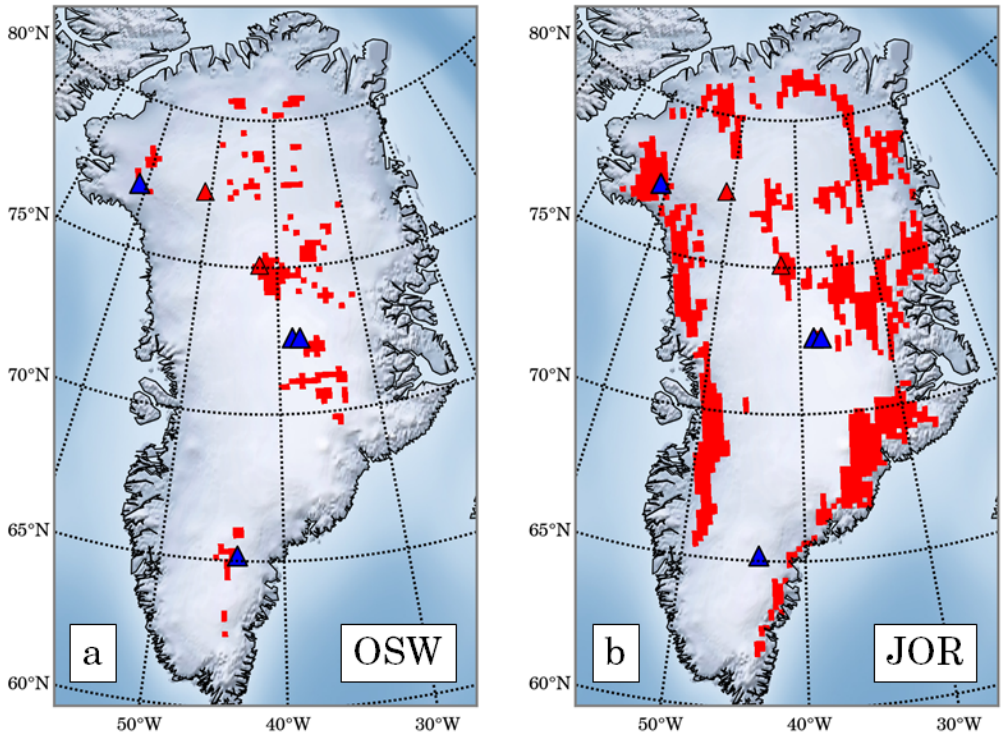

Figure 4.3: Spatial distribution of radar-detected basal water from (a) Oswald et al. (2018)-OSW, and (b) Jordan et al. (2018)-JOR. The datasets provided by the two authors are grouped in 100 km polygons and then sampled at 20 km spacing to represent the spatial resolution of SICOPOLIS that is used in this study.

a cold ice sheet with a no-slip basal condition. This assumption makes their method unsuitable for the current study, because frictional heating is an important heat source especially near the margins of the ice sheet. Therefore, we apply an iterative scheme that incrementally adjusts the GHF in a forward model.

In this study we start the paleoclimate simulations at -134 ka and all simulations are composed of three steps:

1. First, the present-day geometry of GrIS provided by Bamber et al. (2013) is relaxed for 100 years to create smoothed geometry of the ice sheet.

2. From -134 ka to -9 ka, the ice sheet freely evolves given the initial and boundary conditions. Enhanced basal sliding is implemented in the first 5 ka of this step.

3. From -9 ka to present, the results of step (2) are used as initial conditions and ice sheet geometry is continuously nudged to result in the relaxed geometry produced in step (1).

Because the goal is to estimate the GHF required to reach the bed to the pressure melting temperature, at the end of step (3) we check the basal thermal conditions at the locations of radar-detected basal thaw: if T_{pmp} is smaller than -0.1°C, we increase the GHF by 5%. Otherwise, if the basal melt rate $\dot{M}_b$ at these locations is larger than 0.001 m yr^{-1}, we decrease the GHF by 5%. We terminate the simulations after 50 iterations of steps (1) through (3) when the majority of regions of interest have met the pressure melting point's criteria. Note that throughout the iterative procedure, we assume that basal water is due to basal melting at the same location (and not generated in other places and transported to that region), nor does it derive from surface water that has reached the bed.

Since SICOPOLIS is thermo-mechanically coupled, the thermal properties at the locations where GHF is not adjusted impacts the flow field, and hence they impact the thermal properties of all regions. Therefore, we estimate GHF$_{pmp}$ for both radar detections of basal thaw, using five independent simulations with different initial GHF models; four simulations are with the GHF models shown in Fig. 4.1, and one simulation with a spatially uniform GHF of 56 mW m^{-2} (denoted by U56, corresponding to the average GHF value of the North American plate, Sclater et al., 1980). It is important to note that the points being considered for adjustment are not treated individually. Because adjustment of GHF at one location affects the velocity field and temperature profile of its surrounding area, it is important that the GHF adjustment takes into account all the points simultaneously.

4.3 Results

We calculate GHF$_{pmp}$ at the locations of basal thaw predicted by OSW and JOR separately. For each of these datasets, we perform 5 different simulations with all the GHF models considered in this study: at the locations where GHF is not being adjusted (referred to as 'background' GHF),

the GHF values remain fixed as prescribed by each GHF model.

4.3.1 GHF$_{pmp}$ at Oswald et al. (2018) thawed points

Figure 4.4 shows the estimated GHF$_{pmp}$ values at the thawed bed-predictions by Oswald. In every row, the left panel shows the calculated GHF$_{pmp}$; the middle and right panels show the concomitant offset of initial and final surface elevation and surface velocity maps, respectively. For the majority of the ice sheet, the initial surface elevation and velocity maps have been preserved, confirming that the present-day ice sheet is reproduced. The melting point criteria (i.e. $T_b > -0.1°$C relative to the pressure melting point or $\dot{M}_b < 0.001$ m yr^{-1}) are satisfied for all simulations with the OSW dataset.

Although GHF$_{pmp}$ estimates vary based on what is the 'background' GHF, there are several regions where GHF$_{pmp}$ estimates are relatively consistent. In the central-east region, southeast of GISP2 and GRIP ice cores, nearly all simulations show that GHF$_{pmp}$ is between 70-90 mW m^{-2}. Near the NGRIP ice core site, our estimates show that GHF of about 70 mW m^{-2} is sufficient to thaw the bed. Slightly downstream of NGRIP site towards the northeast region, GHF$_{pmp}$ is smaller with values near 40-50 mW m^{-2}. In the northwest region close to the Camp Century ice core site, despite the extent of basal thaw being rather small, the GHF$_{pmp}$ is relatively high with values greater than 85 mW m^{-2}.

An example of a region with different GHF$_{pmp}$ estimate based on the 'background' GHF is in the south near the Dye-3 ice core; with the background of GHF-ML is between 90-110 mW m^{-2}, while it is between 70-80 mW m^{-2} using the other background GHF models. Also, the scattered points in the northern regions have a relatively consistent GHF$_{pmp}$ of about 60-70 mW m^{-2} with exception of magnetic GHF as the background; if the magnetic GHF is used as the background map, these locations require a higher GHF$_{pmp}$ around 80-90 mW m^{-2}.

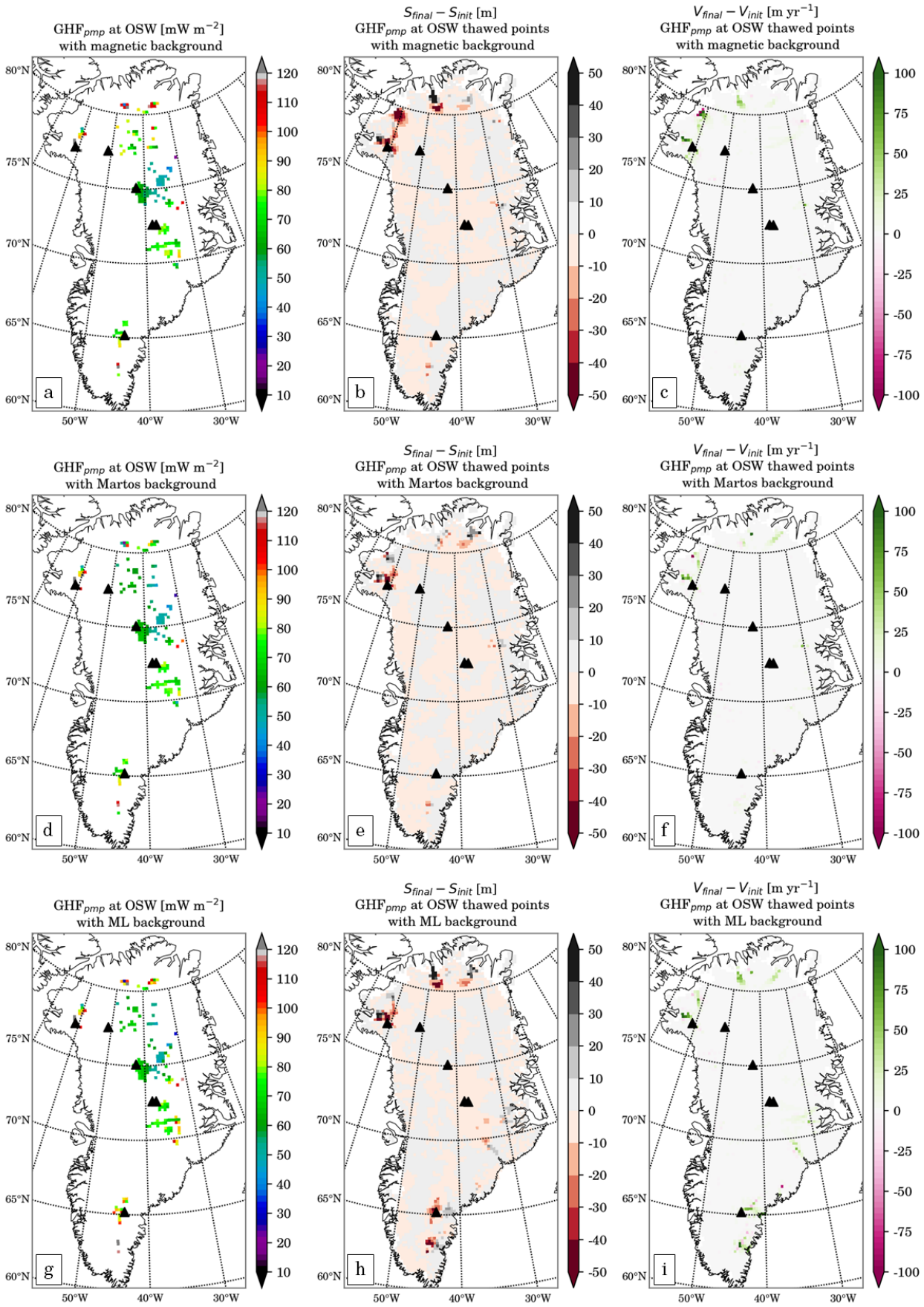
GHF$_{pmp}$ at OSW [mW m^{-2}]
with magnetic background
$S_{final} - S_{init}$ [m]
GHF$_{pmp}$ at OSW thawed points
with magnetic background
$V_{final} - V_{init}$ [m yr^{-1}]
GHF$_{pmp}$ at OSW thawed points
with magnetic background
GHF$_{pmp}$ at OSW [mW m^{-2}]
with Martos background
$S_{final} - S_{init}$ [m]
GHF$_{pmp}$ at OSW thawed points
with Martos background
$V_{final} - V_{init}$ [m yr^{-1}]
GHF$_{pmp}$ at OSW thawed points
with Martos background
GHF$_{pmp}$ at OSW [mW m^{-2}]
with ML background
$S_{final} - S_{init}$ [m]
GHF$_{pmp}$ at OSW thawed points
with ML background
$V_{final} - V_{init}$ [m yr^{-1}]
GHF$_{pmp}$ at OSW thawed points
with ML background
a
b
c
d
e
f
g
h
i
80°N
75°N
70°N
65°N
60°N
50°W
40°W
30°W
120
110
100
90
80
70
60
50
40
30
20
10
50
40
30
20
10
0
-10
-20
-30
-40
-50
100
75
50
25
0
-25
-50
-75
-100

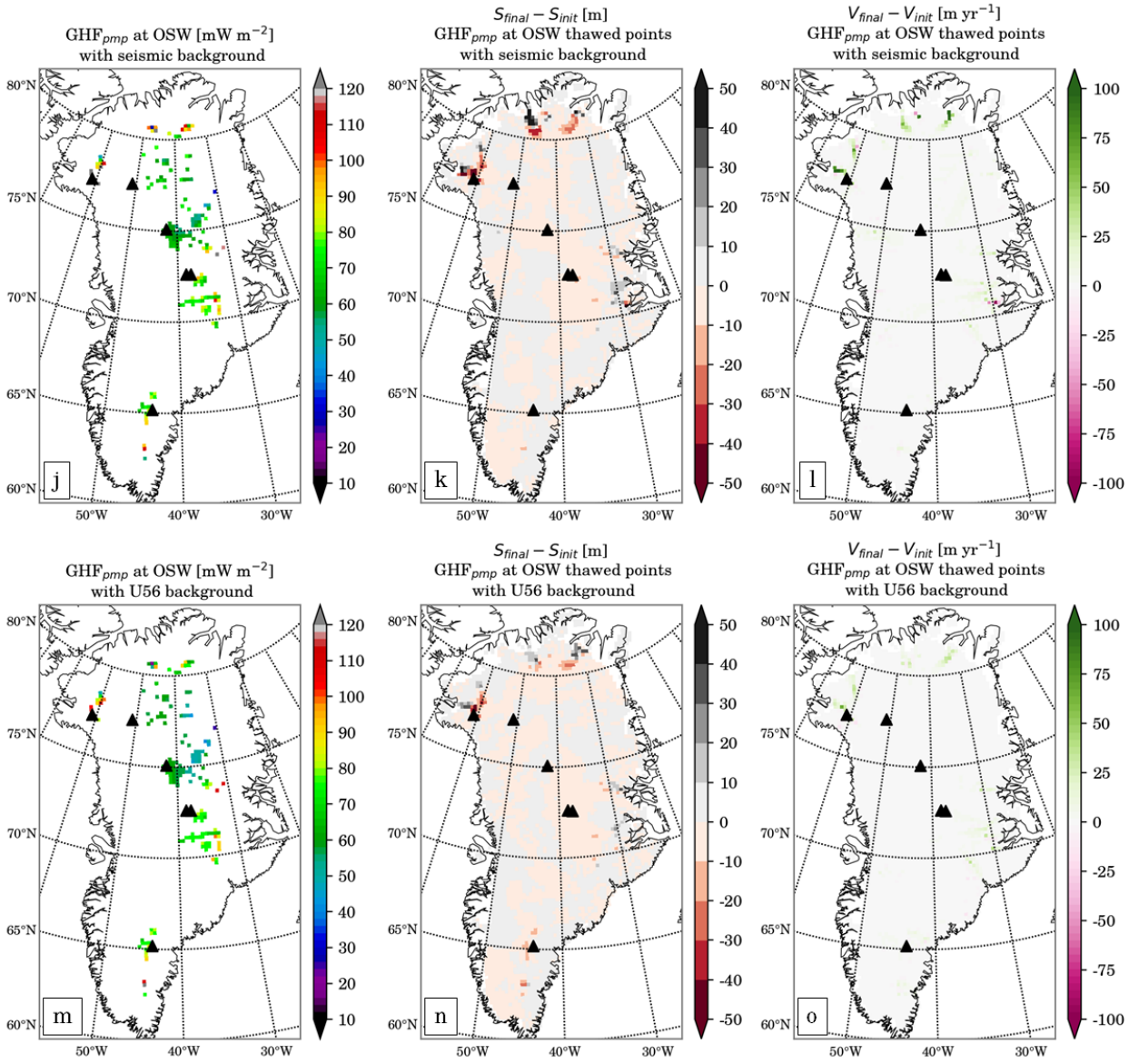

Figure 4.4: Estimating GHF$_{pmp}$ at locations of basal thaw provided by Oswald et al. (2018) using five different GHF maps and the resultant elevation and surface velocity offset after GHF iterations with respect to the initial geometry. Each row shows the GHF$_{pmp}$ with a different 'background' GHF maps; (a-c) Fox Maule et al. (2009), (d-f) Martos et al. (2018), (g-i) Rezvanbehbahani et al. (2017), (j-l) Shapiro & Ritzwoller (2004), and (m-o) uniform GHF of 56 mW m^{-2}.

4.3.2 GHF$_{pmp}$ at Jordan et al. (2018) thawed points

The estimated GHF$_{pmp}$ at the locations of JOR dataset and different initial GHF models are shown in Fig. 4.5. The GHF constraints in the northern parts of interior regions close to the NGRIP ice core site are within the range of 55-75 mW m^{-2}. In contrast, the estimated GHF$_{pmp}$ decreases downstream of NGRIP towards the northeast region of the ice sheet and upstream of the 79North glacier to values as low as 10 mW m^{-2}. These regions, despite having such low GHF$_{pmp}$ values still experience basal melt rates higher than our cut-off criterion (i.e. $\dot{M}_b < 0.001$ m yr^{-1}). The low GHF$_{pmp}$ values in the entire western flank of the ice sheet are similar to those of the downstream reaches of the northeast Greenland. Apart from a few scattered points, the low GHF$_{pmp}$ persists in the entire low-elevation regions in western Greenland.

In contrast to the low GHF$_{pmp}$ regions, two regions stand out in terms of having notably high GHF$_{pmp}$ values using the JOR dataset. In central east and northern parts of the GrIS, GHF$_{pmp}$ values as high as 100-120 mW m^{-2} are estimated. At several of these points, the cut-off criterion for basal temperature relative to the pressure melting point (i.e. $T_b > -0.1°$C) was not achieved and the simulation was terminated after 50 iterations (see section 4.2.3).

4.3.3 Simplified sensitivity analysis

The simulations presented here contain paleoclimate simulations that are enforced based on climate reconstructions of ice cores and marine δ^{18}O records. Therefore, they carry uncertainties that can alter the present results. Given the computational expense of the iterative simulations presented here, performing sensitivity analysis on climatic parameters is extremely costly. Therefore, we analyze the sensitivity of GHF$_{pmp}$ estimates at several anomalous locations with a 1D analytical solution of the temperature profile of ice sheets. We use the solution provided in Chapter 2 of this work which is an improvement to the Robin (1955) analytical solution and allows estimating the GHF$_{pmp}$ given the surface temperature, ice thickness, and surface mass-balance rate. Although the solution is obtained in steady-state conditions (unlike the SICOPOLIS simulations presented here), it facilitates analyzing the sensitivity of GHF constraints on a wider range of climatic variables.

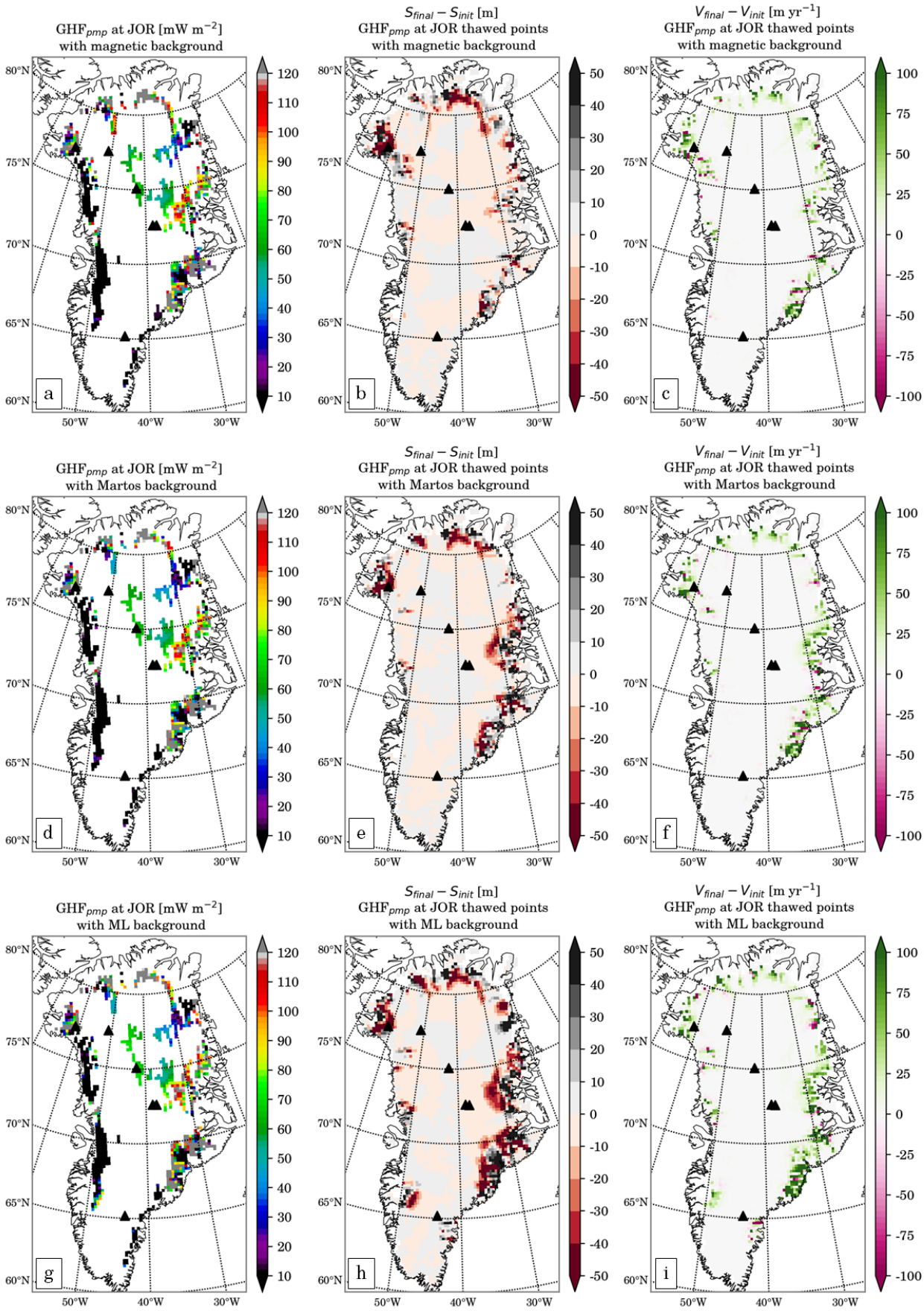
GHF$_{pmp}$ at JOR [mW m^{-2}]
with magnetic background
$S_{final} - S_{init}$ [m]
GHF$_{pmp}$ at JOR thawed points
with magnetic background
$V_{final} - V_{init}$ [m yr^{-1}]
GHF$_{pmp}$ at JOR thawed points
with magnetic background
GHF$_{pmp}$ at JOR [mW m^{-2}]
with Martos background
$S_{final} - S_{init}$ [m]
GHF$_{pmp}$ at JOR thawed points
with Martos background
$V_{final} - V_{init}$ [m yr^{-1}]
GHF$_{pmp}$ at JOR thawed points
with Martos background
GHF$_{pmp}$ at JOR [mW m^{-2}]
with ML background
$S_{final} - S_{init}$ [m]
GHF$_{pmp}$ at JOR thawed points
with ML background
$V_{final} - V_{init}$ [m yr^{-1}]
GHF$_{pmp}$ at JOR thawed points
with ML background
a
b
c
d
e
f
g
h
i
80°N
75°N
70°N
65°N
60°N
50°W
40°W
30°W
120
110
100
90
80
70
60
50
40
30
20
10
50
40
30
20
10
0
-10
-20
-30
-40
-50
100
75
50
25
0
-25
-50
-75
-100

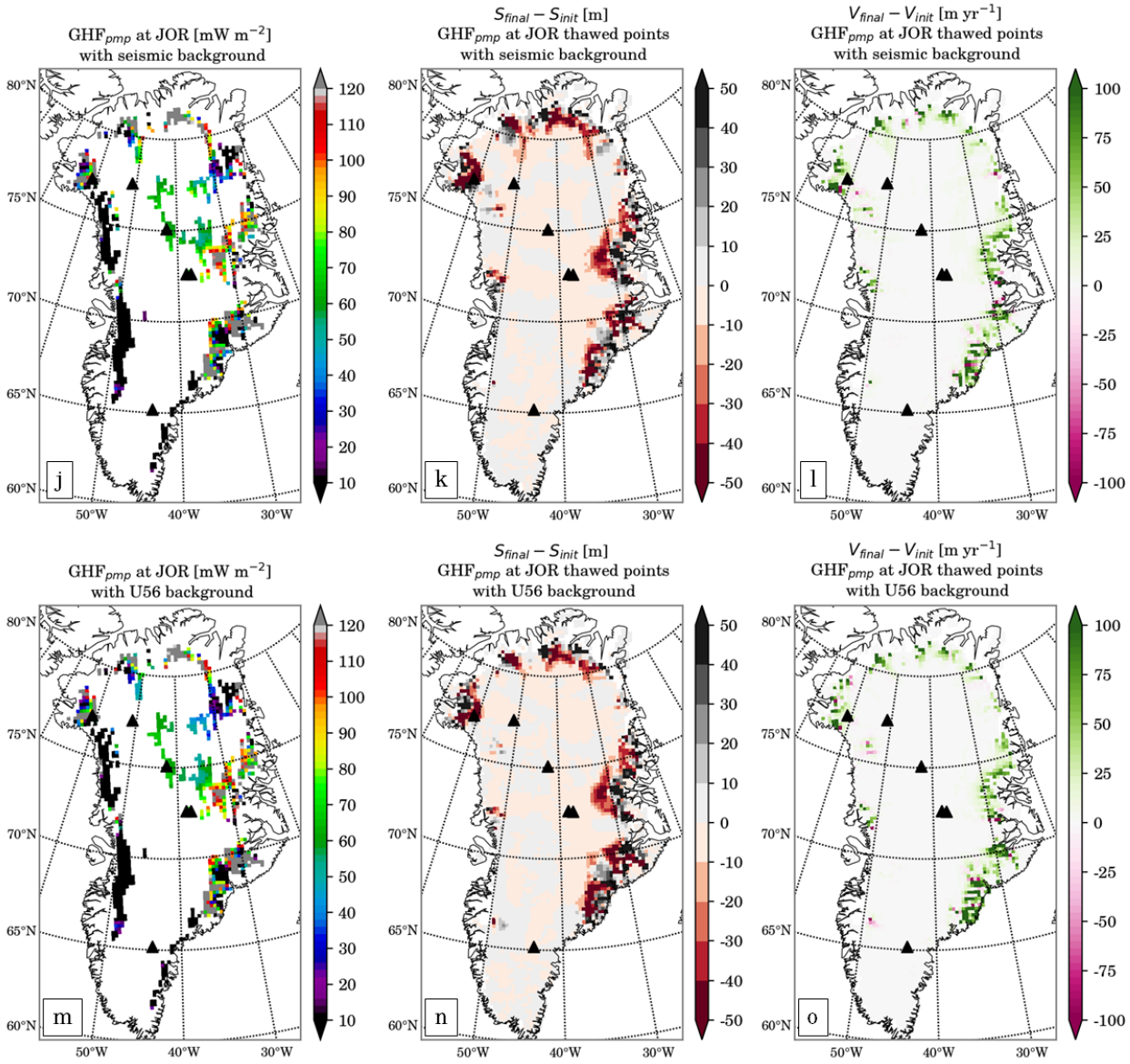

Figure 4.5: Same as Fig. 4.4, with GHF adjustments at the locations of basal water detected by Jordan et al. (2018).

We assess the sensitivity of high GHF_{pmp} estimates near CC, Dye-3, and central east regions of the GrIS.

The CC and Dye-3 ice cores are near ice divides and the horizontal velocities are small. Therefore, the conditions are suitable to use a 1D analytical solution for the vertical temperature near this site. Thickness of the CC and Dye-3 ice cores are $\sim$1400 m and 2000 m, respectively. In the central-east region of the ice sheet where the GHF_{pmp} estimates from SICOPOLIS are high, thickness values range from a few hundred to about 1000 m. Because the analytical solution is in steady-state, we use a range of input variables for surface mass-balance rate and surface temperature to calculate the GHF_{pmp}.

During the 1960-1990 period (during which net accumulation matched the net ablation, Van den Broeke et al., 2009), the surface mass balance from regions obtained from RACMO2/GR (Ettema et al., 2010) ranges between $\sim$0.4 to 0.8 m yr^{-1} ice equivalent with surface temperatures around -30 to $-20°C$ for all the three regions of interest. We use a wider range of surface mass-balance rate values (0.1-1 m yr^{-1}), as well as surface temperatures ranging from -40 to $-10°C$.

The GHF_{pmp} calculations from the 1D analytical solution are shown in Fig. 4.6. Fig. 4.6a,b represent the central-east regions; Fig. 4.6c and d correspond to CC and Dye-3 ice core regions, respectively. This simple sensitivity analysis confirms that the central-east region requires a significantly higher GHF to thaw the bed. It also shows that at the CC ice core site, where RACMO2/GR reports surface temperature of $-25°C$ and surface mass balance-rate of $\sim$0.4 m yr^{-1}, the GHF value of roughly 90 mW m^{-2} is needed to thaw the bed (Fig. 4.6c). The value of GHF_{pmp} drops to $\sim$60 mW m^{-2} for Dye-3 with surface mass balance-rate of $\sim$0.65 m yr^{-1} and surface temperature of $-19°C$. Considering that both these ice cores have measured basal temperatures about $-13°C$, the actual GHF is likely much less than GHF_{pmp} estimates in this section.

4.3.4 Comparing GHF_{pmp} vs. GHF models

The GHF constraints calculated here are the lower limits of GHF to produce basal thaw, and so the GHF models must be larger than the constraints if they are to properly simulate the detections

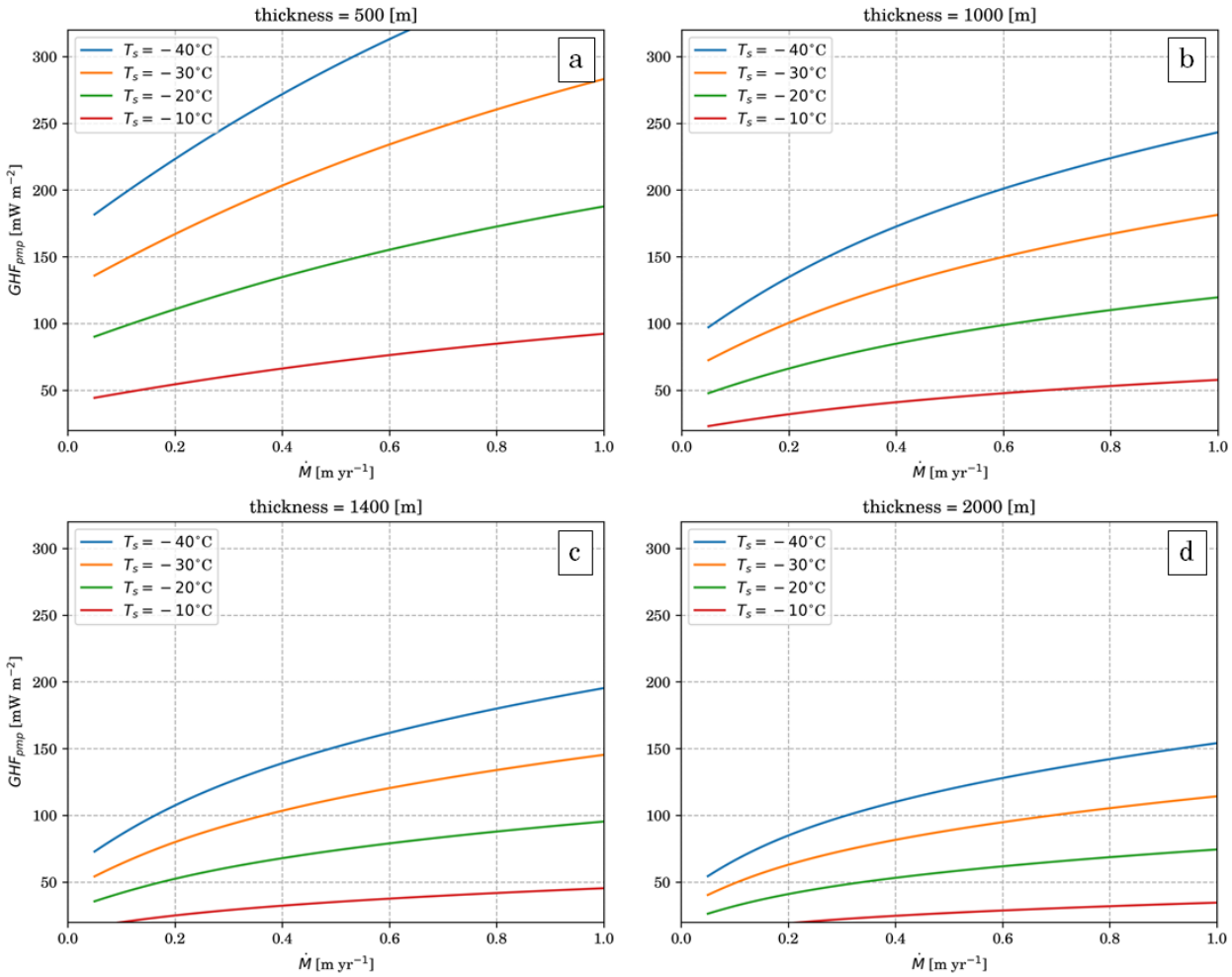

Figure 4.6: GHF$_{pmp}$ calculated from the 1D analytical solution provided by Rezvanbehbahani et al. (2019). The GHF$_{pmp}$ is calculated for 4 thickness values of (a) 500 m, (b) 1000 m, (c) 1400 m, and (d) 2000 m and a range of surface temperature values T_s from -10 to $-40°$C. The x-axis represents the surface mass balance, $\dot{M}$. The thickness ranges of (a) and (b) are chosen to represent the central-east region of the GrIS, while (c) is chosen to represent the CC ice core, and (d) represents the Dye-3 ice core.

of basal thaw. Figs. 4.7 through 4.10 show the difference between GHF$_{pmp}$ and GHF models at locations of basal thaw for both radar datasets; green and blue colors refer to regions that satisfy the constraints (GHF>GHF$_{pmp}$) and red colors mark the regions of disagreement (GHF<GHF$_{pmp}$). Because the uncertainties in all GHF models are relatively high, the colorbar is chosen such that ± 2 mW m^{-2} difference appears as a reasonable range on the comparison maps.

There are several locations where the GHF models satisfy their lowest constraint imposed by

GHF_{pmp}. The most notable of all are the downstream regions of almost the entire western margin of the ice sheet where JOR dataset predicts extensive basal thaw. Our estimated GHF constraints are very small and all GHF models satisfy the constraints. Other notable regions are the northeast of the NGRIP ice core (from OSW dataset) and approximate location of the downstream of NEGIS upstream of 79North glacier (from JOR dataset).

In contrast, several regions from both datasets result in very high GHF constraints that are not satisfied in any of the GHF models. The most prominent one is the central-east region at 30°W, 70°N and to the north at about 30°W, 73°N. The GHF models in this region are substantially smaller than the required heat flux to thaw the bed. Other regions of disagreement are around the CC ice core (from both radar datasets), scattered points near Dye-3 (Figs. 4.7a to 4.10a) and the northern margin of the ice sheet (Figs. 4.7b to 4.10b).

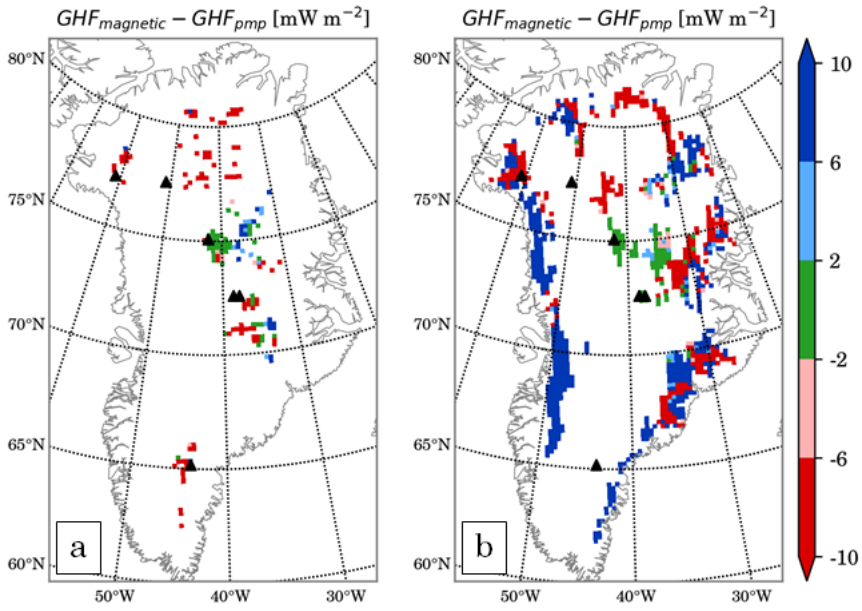

Figure 4.7: Comparing the GHF constraints at thawed points of (a) OSW and (b) JOR with respect to magnetically-inferred GHF of Fox Maule et al. (2009).

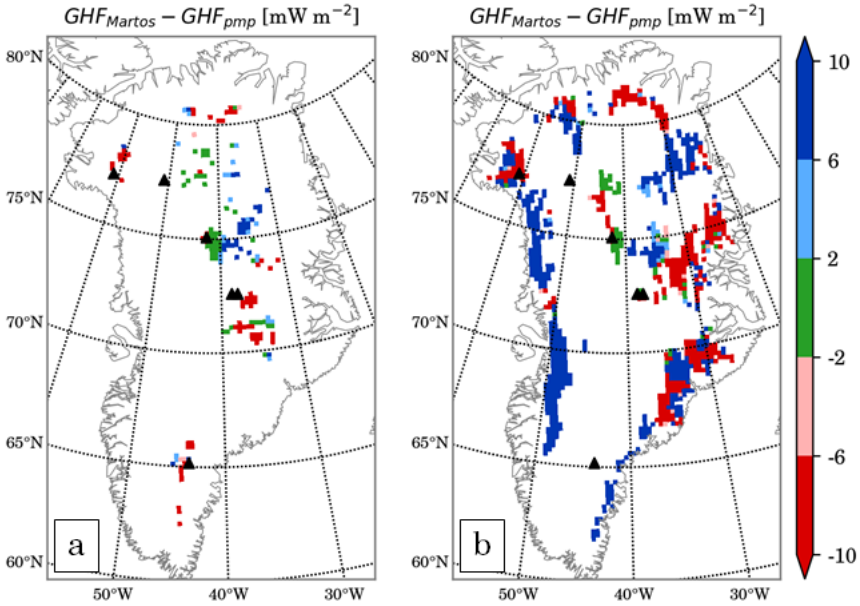

Figure 4.8: Same as Fig. 4.7 but with respect to GHF derived by Martos et al. (2018).

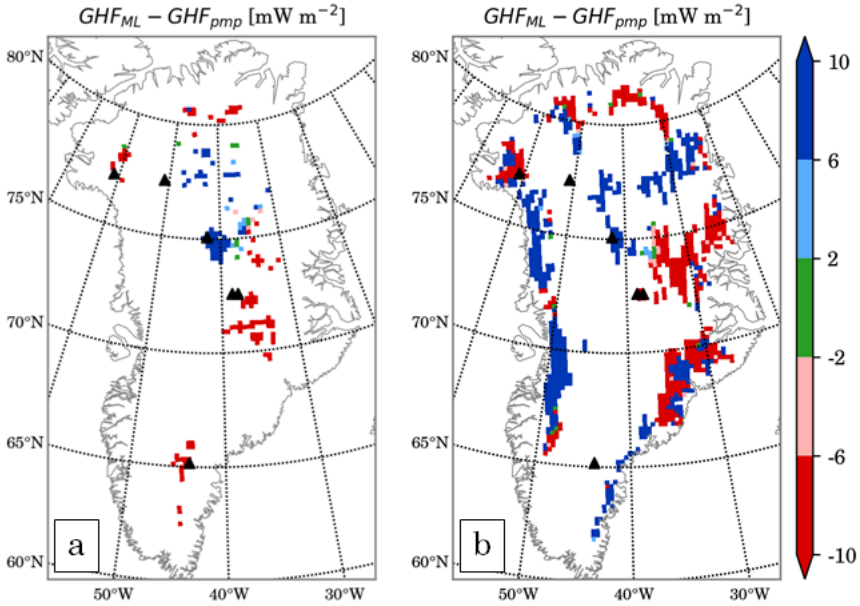

Figure 4.9: Same as Fig. 4.7 but with respect to GHF derived by Rezvanbehbahani et al. (2017).

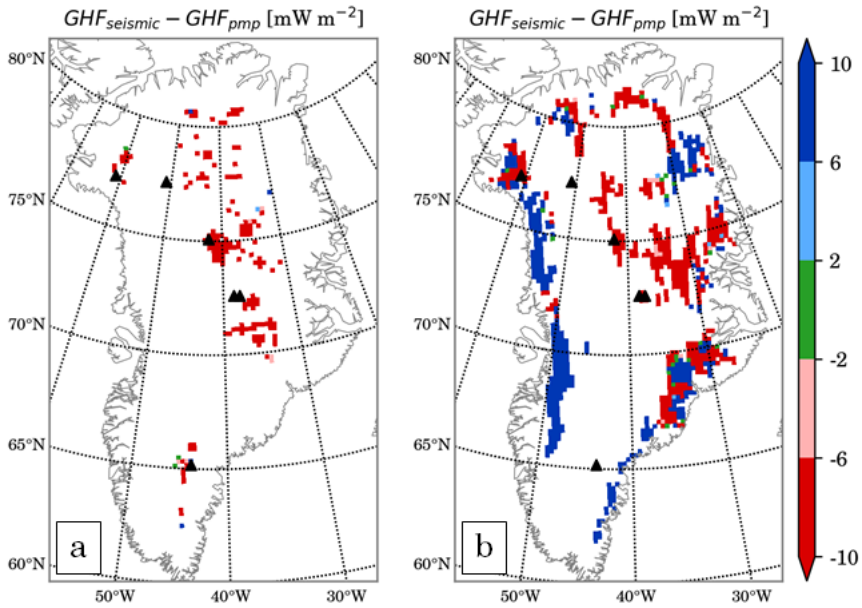

Figure 4.10: Same as Fig. 4.7 but with respect to GHF derived by Shapiro & Ritzwoller (2004).

4.4 Discussion

4.4.1 General discussion

There are regions of basal thaw in the central-east catchment of the ice sheet where the GHF_{pmp} values are estimated to be very high. There are no deep ice cores in this area to confirm or reject such high GHF estimates. Nearly all GHF models predict elevated GHF values in the eastern edge of Greenland (at 70°N,30°W, Fig. 4.1), but except for the magnetically-derived GHF map of Fox Maule et al. (2009), none of the maps predict GHF values as high as 100 mW m^{-2}. The GHF reconstruction of Rogozhina et al. (2016) does predict such high values; however, their analysis has not been included in this study, since it is only limited to the northern half of Greenland. This region is suggested to have lower lithosphere viscosity as well as a higher temperature compared to rest of the cratonic regions in Greenland (Mordret, 2018). Therefore, the extensive basal thaw in the central-east region may be associated with GHF variations due to the remnant of Icelandic plume.

Among the six deep ice cores shown in Fig. 4.3, only two of them contain evidence of basal

thaw: NGRIP (Dahl-Jensen et al., 2003) and NEEM (Dahl-Jensen, private communication with R. Greve). However, the two radar datasets used in this study suggest the existence of basal thaw near the site of several ice cores. Oswald et al. (2018) detect ponded water underneath NGRIP, southeast of GISP2, and at close proximity to CC and Dye-3 sites. The extent of basal thaw near CC is much greater in the JOR dataset, while they detect no temperate zone near Dye-3.

The basal temperature at the GISP2 and GRIP ice core sites are reportedly cold at about $-9°C$ (Dahl-Jensen et al., 1998). Both radar datasets detect water a few tens of kilometers to the east of these ice cores. The GHF to match the basal temperature measurements at the GRIP ice core site is 51 mW m^{-2} (Greve, 2005). The value of GHF_{pmp} at the basal thaw determinations in these regions is estimated to be close to the continental average (~ 70 mW m^{-2}). Given that the distance between GRIP/GISP2 ice core sites and the closest cluster of basal water determinations from the two datasets is about 30-40 km, we suggest that the observed basal thaw in this region can be associated to spatial variations in the GHF.

Radar determinations of basal thaw or ponded water near Dye-3 and CC ice core sites are surprising. The basal temperatures at Dye-3 and CC ice cores are both near $-13°C$ (Gundestrup & Hansen, 1984; Dansgaard et al., 1969), far below the pressure melting temperature. The matching GHF to reproduce these basal temperatures in SICOPOLIS are 32 mW m^{-2} for Dye-3 and 47 mW m^{-2} for CC (Greve 2018, in press). Our results show that GHF_{pmp} ranges between 70-90 mW m^{-2} near Dye-3 and is over 100 mW m^{-2} near the CC ice core site (Figs. 4.4 and 4.5). Comparison between the GHF models and estimated GHF_{pmp} shows that neither of the GHF models predict such high GHF values in these regions (see section 4.3.4). The closest cluster of basal thaw determinations from Jordan et al. (2018) dataset is about 5 km away from the CC ice core and the closest cluster of ponded water from Oswald et al. (2018) is more than 10 km away. The contrast between the GHF at ice cores and GHF_{pmp} in close vicinity of the core sites indicates that the basal thermal conditions could vary over much shorter spatial scales than commonly assumed. While there is no standard expected length-scale for spatial variations in GHF, it is unlikely that GHF can vary so drastically in such small spatial scales.

The apparent contradiction between detection of basal thaw from radar data and very low basal temperatures from ice cores cannot be reconciled without considering other local mechanisms that can alter the local heat flux at the bed. Van der Veen et al. (2007) show that variations in topography (such as troughs and valleys) alter the local GHF so that topographic lows experience enhanced heat fluxes at edges, while the topographic highs have lower heat flux peaks. Given the rough nature of subglacial topography (especially in the central east regions, Rippin, 2013), it is possible that such high GHF fluctuations do actually occur at such small spatial scales. Additional mechanisms have been suggested that influence the net heat flux at the base of the ice sheet. Gooch et al. (2016) suggest that during the retreat phase of the ice sheets, the vertical water discharge from sedimentary aquifers in the subglacial environment can add to the net heat budget at the base of the ice sheet. In Greenland, geophysical surveys have identified regions of saturated till at the bed (e.g., Christianson et al., 2014); however, the study of subglacial aquifers has gained little attention. The third mechanism to elevate the GHF is due to the 'vug-wave' fluid migration processes (Phipps Morgan & Holtzman, 2005); due to the loading and unloading during the glacial and inter-glacial phases, Stevens et al. (2016) show that molten magma at depth can migrate through faults and dyke emplacement which can substantially augment the basal heat flux. All these three mechanisms occur at a much smaller spatial scale than the GHF models presented here. Therefore, special attention should be dedicated to small-scale processes that can result in significant and short-scale variations of GHF.

Our results indicate that the lower elevation region of western Greenland, even with low GHF values of 10 mW m^{-2}, undergoes substantial basal thaw (Figs. 4.7b to 4.10b). This indicates that there is a very high certainty that these regions are almost entirely temperate. It is surprising, however, that radar data analysis does not show a continuous determination of basal water (see Jordan et al. (2018, Fig. 6) and Oswald et al. (2018, Fig. 11)). Our findings demonstrate that the extent of basal thaw in these regions is significantly larger than what is inferred from radar data. This confirms Jordan et al. (2018)'s note that their criterion for basal thaw is necessary but insufficient (and that their results only show "rapid spatial transitions" in basal condition). We

suggest that this region can serve as a proper location for improving the analysis of radar data, because according to the analysis presented here, it is likely extensively thawed at the bed.

4.4.2 Catchment-wide $\dot{M}_b$ estimates

The GHF models for Greenland analyzed in this study bear almost no resemblance to each other (Fig. 4.1). Without direct borehole measurements and some indirect geologic and glaciologic proxies (e.g. the onset location of the Northeast Greenland Ice Stream, NEGIS, or the possible trajectory of the Icelandic plume), there is no straightforward way to confirm or reject the current models. These GHF models undoubtedly lead to different spatial distributions of basal thaw in Greenland (e.g., Rogozhina et al., 2012). It is crucial, however, to investigate whether these different models and their 'modified' versions (which include the GHF_{pmp} estimates in this study) result in substantial differences in terms of the amount of basal water generated in Greenland.

In order to evaluate the impact of GHF differences and the calculated constraints on the net basal melt rate in Greenland, we calculate the annual rate of basal melt-water produced in each catchment of Greenland with a) all 5 GHF maps (as in Fig. 4.1 and U56), b) modified GHF models in Fig. 4.1 by setting the GHF values to GHF_{pmp} at the regions of disagreement (section 4.3.4) according to OSW dataset, and c) same as case b) but modified according to the distribution of JOR dataset. In other words, the 'modified' GHF maps are GHF_{mod}=max(GHF, GHF_{pmp}).

Comparison between the values of total basal melt rate show that although the spatial distribution of temperate bed may vary substantially depending on the GHF model, the total magnitude of basal melt-water remains relatively unchanged (Table 4.1). The net basal melt rate of GrIS using different GHF models is about 15-20 $km^3\ yr^{-1}$. This number is roughly 25 times smaller than the range of surface melt-water generated in Greenland (Fettweis et al., 2013, $\sim$400 GT yr^{-1} equivalent to $\sim$436 $km^3\ yr^{-1}$). However, it has important implications for estimating the continuous year-round discharge from the base of outlet glaciers.

Table 4.1: Basal melt rate in $km^3\ yr^{-1}$ for individual catchments of the GrIS. Three sets of basal melt rates are reported (first column). First the basal melt rate for each catchment using all GHF maps prior to any adjustment at locations of thawed bed. Second, the basal melt rates for all catchments with all GHF maps are reported after modifying the GHF at OSW thawed locations, and the third set of simulations are after modifying the GHF at JOR thawed points. The modified heat flux is defined as GHF_{mod}=max(GHF, GHF_{pmp}). Catchment boundaries are chosen similar to Csathó et al. (2014), and $\Sigma\dot{M}$ is the sum of basal melt rate in all catchments.

Simulation	GHF	JAX	CE	N	NE	NW	SE	SW	$\Sigma\dot{M}_b$
before GHF adjustment	magnetic	2.16	1.14	0.84	0.37	3.00	7.27	2.85	17.65
	Martos	2.38	0.70	0.91	0.78	3.69	6.86	2.76	18.09
	ML	2.15	0.33	0.9	0.85	3.57	5.09	1.38	14.27
	seismic	2.09	0.47	0.54	0.34	3.12	7.12	2.87	16.46
	U56	2.29	0.43	0.85	0.66	3.79	6.38	2.45	16.85
with GHF_{mod} at OSW	magnetic	2.17	1.09	0.88	0.35	2.96	7.26	2.87	17.60
	Martos	2.39	0.89	1.02	0.85	3.86	7.31	2.76	19.10
	ML	2.16	0.37	0.97	0.87	3.61	5.29	1.37	14.65
	seismic	2.10	0.50	0.60	0.40	3.18	7.14	2.87	16.81
	U56	2.30	0.46	0.89	0.68	3.82	6.44	2.46	17.06
with GHF_{mod} at JOR	magnetic	2.18	1.22	0.96	0.50	3.30	7.57	2.87	18.62
	Martos	2.39	0.90	1.02	0.86	3.86	7.31	2.76	19.10
	ML	2.16	0.62	1.04	3.68	3.78	5.82	1.44	18.56
	seismic	2.11	0.71	0.72	0.49	3.40	7.55	2.87	17.87
	U56	2.30	0.69	0.96	0.75	3.96	7.00	2.45	18.13

4.4.3 Modeling shortcomings

Throughout the iterative procedures in all the simulations of this study, the aim has been to keep the GrIS geometry intact. Because the iterations using Oswald et al. (2018) dataset involved fewer points, the geometry and surface velocity has been reconstructed relatively well (Fig. 4.4). However, the spatial extent of the basal thaw based on Jordan et al. (2018) is much larger. Therefore, the substantial adjustments to the GHF alter the geometry of the ice sheet; these alterations are more notable towards the margins and insignificant in the interior regions (Fig. 4.5). Due to thermo-mechanical coupling of the ice flow, local enhancement of GHF changes the flow and geometry, specifically in the low velocity regions (Pittard et al., 2016). Changes in the velocity profile of

the ice sheet alter the rate of advection from upstream, therefore altering the thermal field of the neighboring points. Therefore, it is not surprising that the GHF_{pmp} based on either OSW or JOR datasets varies depending on the initial choice of GHF map.

The effective resolution of JOR dataset is about 5 km, and the internal consistency method of OSW results are provided in 1 km spatial scale. Due to the huge computational cost of performing the iterative procedure in 5-10 km spatial resolution, we clustered the locations of basal thaw from the two datasets into 20 km spatial resolution. This clustering is an exaggeration of the extent of thaw for both basal water datasets. The determinations of temperate basal ice from the radar data could be associated to enhanced localized heat flux (e.g., Van der Veen et al., 2007) or a complex distribution of subglacial water (e.g., Schroeder et al., 2013; Chu et al., 2018). In order to reconstruct such small scale details of basal heat and direction of subglacial water flow, higher resolution models coupled with a dynamic hydrologic component must be considered (e.g. Dow et al., 2018).

Despite undeniable improvements of the numerical ice sheet modeling community, reconciling the differences between their results requires more effort. Specifically for modeling the basal thermal state of the GrIS, the ensemble results of SeaRISE models show sharp contrasts, despite applying similar initial and boundary conditions to the models. This is perfectly demonstrated in the synthesis of MacGregor et al. (2016, Fig. 3) where the SeaRISE ensemble models are used as one of the components to identify likely locations of frozen or thawed bed. Therefore, we urge the community for a more in-depth analysis of the causes of differences between the thermal component of the numerical ice sheet models with the aim of reconciling the sharp contrasts between models themselves to increase the confidence in the modeling the basal thermal state of ice sheets.

4.5 Conclusion

We use the locations of basal water in Greenland, detected by two radar datasets to constrain the GHF in Greenland using SICOPOLIS numerical model. The GHF at these locations is iteratively adjusted so that the basal temperature or basal melt rates become near zero, hence finding the

minimum GHF that requires to reach the bed to the melting point (GHF_{pmp}). We conduct the iterative simulations with different initial GHF models of Greenland to resolve the uncertainty associated with the initial basal thermal condition on the final constraints. Although there are locations whose GHF constraints differ depending on the initial GHF model, there are persistent regions where the constraints are anomalously high or low. The most prominent regions with anomalously low GHF_{pmp} values include a large part of the low-elevation regions of the western flank of the ice sheet, as well as in the northeast region, downstream of NEGIS.

We find several regions with GHF_{pmp} values as high as 100 mW m^{-2}. The largest region with high GHF_{pmp} is in the central-east of the ice sheet east of GISP2 and GRIP ice cores; in all simulations the estimated GHF_{pmp} is about 100-120 mW m^{-2}, but we suggest that due to the geologic history of this region such high GHF values are plausible.

Our results highlight sharp contrasts between low basal temperature readings from CC and Dye-3 ice cores and prediction of basal water by both radar datasets. We argue that the existence of water in close proximity to these ice cores cannot be explained by the spatial variability of GHF; we posit that such sharp contrasts can be better explained by the effect of elevated heat flux near the topographic edges (Van der Veen et al., 2007), the interplay between the glacial loading and the volcanism in the underlying crust (Stevens et al., 2016), or the discharge of groundwater aquifers into the subglacial environment and elevating the basal heat flux (Gooch et al., 2016). These mechanisms are not currently incorporated in GHF or glaciologic models and can help resolve the current discrepancies between modeled and observed basal thermal state of the GrIS. Finally, we show that despite all these difference in GHF maps and uncertainties in reconciling observations with our model, the net basal melt-water production does not significantly differ depending on the GHF model.

Chapter 5

Concluding Remarks and Future Work

5.1 Summary

Since 1955 when Gordon Robin presented his analytical solution for the 1D vertical energy conservation equation for ice sheets, it has been frequently used as a 'back-of-the-envelope' means for calculating ice temperatures. Modifications to the Robin (1955) solution have been suggested, for example, by Zotikov (1986) or Hindmarsh et al. (2009) that incorporate basal melt to the solution. However, the accuracy of the Robin solution had not been previously examined. In Chapter 2, we show that his solution substantially underestimates the temperature profile of ice sheets. Instead, we provide an alternative solution that produces more accurate temperature profiles in the interior of the ice sheets. We highlight the importance of strain heating on estimating the basal temperature and suggest a simple approach to include strain heating in the analytical solution. Finally, we compare the difference in basal temperature estimates from the analytical solution and a numerical 2D model and roughly prescribe the regions in Greenland and Antarctica where the new analytical solution can be applied.

We present the first geology-based machine learning-derived map of geothermal heat flux (GHF) in Greenland. The new map is based on the compilation of global GHF measurements and a large number of geologic and tectonic features that are related to GHF. The predicted GHF map captures the trajectory of the movement of the North American plate over the Icelandic plume by predicting a narrow swath of elevated heat flux in central-west Greenland. In addition, the new map suggests several locations with elevated GHF values including the central-west region of the GrIS and upstream of Jakobshavin Isbræ. Locations with high GHF are also predicted upstream

of a few other fast-flowing glaciers such as Nioghalvfjerdsfjorden and Petermann glaciers in the northeast and north Greenland, respectively. The elevated heat flux and fast flow of these glaciers suggests a possible link between enhanced basal melting, warm deformable ice, and high glacier speeds. The onset location of fast-flowing ice in both Greenland and Antarctica has been associated with regions of elevated heat flux and basal water (e.g. Fahnestock et al., 2001; Bell et al., 2007; Langley et al., 2014), consistent with our findings in Chapter 3.

Ice cores provide valuable information about the basal thermal condition of the GrIS. Apart from direct temperature readings at the bed, the GHF at ice core sites can be inferred from measuring the temperature gradient at the bottom layers. However, due to their extremely high financial costs and logistic constraints, there are only a few deep ice cores in Greenland. Therefore, radar-based observations are essential to infer information about the spatial distribution of basal thaw in Greenland. In Chapter 4, we use the results of two recent studies (that have used radar data to infer basal water) to constrain the GHF at thawed locations. We iteratively adjust the value of GHF at thawed locations in a large-scale numerical ice sheet model SICOPOLIS to reach the bed just to the pressure melting point. The estimated heat flux (GHF_{pmp}) is the minimum GHF that is required to keep the bed thawed.

Our estimates of GHF_{pmp} show substantial spatial variability in Greenland. The western part of the GrIS, in general, can be thawed with relatively small GHF values of around 10 mW m^{-2}. The GHF constraints are small in the northeastern part of the ice sheet, downstream of the Northeast Greenland Ice Stream (NEGIS). In contrast, we find several regions where GHF_{pmp} estimates are surprisingly high ($>$100 mW m^{-2}). In particular, near Camp Century and Dye-3 ice core sites where cold basal temperatures have been measured ($\sim -13^{\circ}$C), radar observations report the existence of basal water. Our estimates show that GHF must be at least 2 times greater than the inferred GHF at ice cores sites to thaw the bed.

The central-east region also has anomalously high GHF_{pmp} values. Our estimates show that GHF_{pmp} values greater than 100 mW m^{-2} are required to thaw the bed. Such anomalously high GHF values are not reported in almost any of the current GHF models for Greenland, and our

comparison shows that none of the current GHF models leads to such extensive thawed bed in the central-east region. We propose three major mechanisms that could lead to sharp local enhancements in the basal heat budget as an explanation for such high estimates.

5.2 Future Work

This dissertation poses several questions to our current understanding of the basal thermal state of the GrIS that require further investigation. First, from a modeling perspective, the analytical solution presented in Chapter 2 does not incorporate horizontal velocities. Therefore, it is applicable only in the low-velocity regions. Further work can be done to solve the 2D energy conservation equation using velocity components in the horizontal direction, obtained from the shallow ice approximation. The 2D solution can greatly simplify studying the sensitivity of ice sheets' temperature fields farther from the interior regions.

Our predicted GHF map in Greenland shows that several regions of high GHF are upstream of the fast flowing glaciers in Greenland. Associating the location of fast-flowing glaciers with regions of elevated heat flux is a widely-accepted theory in glaciology. However, little work has been done to examine the causality between these two processes. Therefore, further diagnostic modeling work must be pursued to simulate the effect of the produced basal melt-water on the ice flow. The modeling study must be coupled with a subglacial hydrologic model, in order to properly establish the relationship between elevated heat flux, basal melting, and fast flow of glaciers.

The final chapter of this dissertation reveals several issues with the current GHF models and radar analysis techniques that need further investigation. We find a consistent region in the entire west flank of Greenland that requires very low GHF values to be thawed at the base, implying that the region is likely extensively thawed. Given that radar picks of basal water are very scattered in this region, we propose that analysis of radar data can be further improved to provide a more contiguous basal water pick in this region. Finally, the striking inconsistency between all the GHF maps calls for additional field surveys and borehole measurements that are specifically designed to measure the GHF (e.g. Fisher et al., 2015). Without direct borehole measurements, none of the

GHF models can be either confirmed or rejected.

References

Abramowitz, M. & Stegun, I. A. (1964). *Handbook of mathematical functions: with formulas, graphs, and mathematical tables*, volume 55. Courier Corporation.

Adalgeirsdottir, G., Aschwanden, A., Khroulev, C., Boberg, F., Mottram, R., Lucas-Picher, P., & Christensen, J. (2014). Role of model initialization for projections of 21st-century Greenland ice sheet mass loss. *Journal of Glaciology*, 60(222), 782–794.

Amante, C. & Eakins, B. W. (2009). *ETOPO1 1 arc-minute global relief model: procedures, data sources and analysis*. US Department of Commerce, National Oceanic and Atmospheric Administration, National Environmental Satellite, Data, and Information Service, National Geophysical Data Center, Marine Geology and Geophysics Division Colorado.

Amore, P. (2005). Asymptotic and exact series representations for the incomplete gamma function. *EPL (Europhysics Letters)*, 71(1), 1.

Anandakrishnan, S., Blankenship, D., Alley, R., & Stoffa, P. (1998). Influence of subglacial geology on the position of a West Antarctic ice stream from seismic observations. *Nature*, 394(6688), 62–65.

Andersen, K., Azuma, N., Barnola, J., Bigler, M., Biscaye, P., Caillon, N., Chappellaz, J., Clausen, H., Dahl-Jensen, D., Fischer, H., et al. (2004). High-resolution record of Northern Hemisphere climate extending into the last interglacial period. *Nature*, 431(7005), 147.

Anderson, D. (2016). The Compleate Hot Spot. `http://www.mantleplumes.org/CompleateHotspot.html`. Accessed: 2016-08-29.

Aschwanden, A., Adalgeirsdottir, G., & Khroulev, C. (2013). Hindcasting to measure ice sheet model sensitivity to initial states. *The Cryosphere*, 7(4), 1083.

Aschwanden, A., Bueler, E., Khroulev, C., & Blatter, H. (2012). An enthalpy formulation for glaciers and ice sheets. *Journal of Glaciology*, 58(209), 441–457.

Balmino, G., Vales, N., Bonvalot, S., & Briais, A. (2012). Spherical harmonic modelling to ultra-high degree of Bouguer and isostatic anomalies. *Journal of Geodesy*, 86(7), 499–520.

Bamber, J., Griggs, J., Hurkmans, R., Dowdeswell, J., Gogineni, S., Howat, I., Mouginot, J., Paden, J., Palmer, S., Rignot, E., & Steinhage, D. (2013). A new bed elevation dataset for Greenland. *The Cryosphere*, 7(2), 499–510.

Bassin, C. (2000). The current limits of resolution for surface wave tomography in North America. *Eos Trans. AGU*.

Bell, R., Studinger, M., Shuman, C., Fahnestock, M., & Joughin, I. (2007). Large subglacial lakes in East Antarctica at the onset of fast-flowing ice streams. *Nature*, 445(7130), 904–907.

Bergman, T., Incropera, F., DeWitt, D., & Lavine, A. (2011). *Fundamentals of heat and mass transfer*. John Wiley & Sons.

Bindschadler, R., Nowicki, S., Abe-Ouchi, A., Aschwanden, A., Choi, H., Fastook, J., Granzow, G., Greve, R., Gutowski, G., Herzfeld, U., et al. (2013). Ice-sheet model sensitivities to environmental forcing and their use in projecting future sea level (the SeaRISE project). *Journal of Glaciology*, 59(214), 195–224.

Blatter, H. & Greve, R. (2015). Comparison and verification of enthalpy schemes for polythermal glaciers and ice sheets with a one-dimensional model. *Polar Science*, 9(2), 196–207.

Bondzio, J., Morlighem, M., Seroussi, H., Kleiner, T., Rückamp, M., Mouginot, J., Moon, T., Larour, E., & Humbert, A. (2017). The mechanisms behind Jakobshavn isbræ's acceleration and mass loss: a 3d thermomechanical model study. *Geophysical Research Letters*, 44(12), 6252–6260.

Boyce, W., DiPrima, R., & Haines, C. (1969). *Elementary differential equations and boundary value problems*, volume 9. Wiley, New York.

Brinkerhoff, D. & Johnson, J. (2015). Dynamics of thermally induced ice streams simulated with a higher-order flow model. *Journal of Geophysical Research: Earth Surface*, 120(9), 1743–1770.

Brinkerhoff, D. J. & Johnson, J. (2013). Data assimilation and prognostic whole ice sheet modelling with the variationally derived, higher order, open source, and fully parallel ice sheet model VarGlaS. *The Cryosphere*, 7, 1161.

Brooks, A. & Hughes, T. (1982). Streamline upwind/Petrov-Galerkin formulations for convection dominated flows with particular emphasis on the incompressible Navier-Stokes equations. *Computer methods in applied mechanics and engineering*, 32(1-3), 199–259.

Buchardt, S. L. (2009). *Basal melting and Eemian ice along the main ice ridge in Northern Greenland*. PhD thesis, University of Copenhagen.

Christianson, K., Peters, L., Alley, R., Anandakrishnan, S., Jacobel, R., Riverman, K., Muto, A., & Keisling, B. (2014). Dilatant till facilitates ice-stream flow in northeast Greenland. *Earth and Planetary Science Letters*, 401, 57–69.

Chu, W., Schroeder, D., Seroussi, H., Creyts, T., & Bell, R. (2018). Complex basal thermal transition near the onset of Petermann Glacier, Greenland. *Journal of Geophysical Research: Earth Surface*, 123(5), 985–995.

Clarke, G., Nitsan, U., & Paterson, W. (1977). Strain heating and creep instability in glaciers and ice sheets. *Reviews of Geophysics*, 15(2), 235–247.

Coffin, M., Gahagan, L., & Lawver, L. (1998). Present-day plate boundary digital data compilation. *University of Texas Institute for geophysics technical report*, 174(5).

Csathó, B., Schenk, A., van der Veen, C. J., Babonis, G., Duncan, K., Rezvanbehbahani, S., van den Broeke, M., Simonsen, S., Nagarajan, S., & van Angelen, J. (2014). Laser altimetry reveals

complex pattern of Greenland Ice Sheet dynamics. *Proceedings of the National Academy of Sciences*, 111(52), 18478–18483.

Cuffey, K. & Paterson, W. (2010). *The Physics of Glaciers*. Elsevier, Burlington, USA.

Cummings, E. (2016). Modeling the cryosphere with FEniCS. *arXiv preprint arXiv:1609.02190*.

Dahl-Jensen, D. (1989). Steady thermomechanical flow along two-dimensional flow lines in large grounded ice sheets. *Journal of Geophysical Research: Solid Earth*, 94(B8), 10355–10362.

Dahl-Jensen, D., Gundestrup, N., Gogineni, S., & Miller, H. (2003). Basal melt at NorthGRIP modeled from borehole, ice-core and radio-echo sounder observations. *Annals of Glaciology*, 37(1), 207–212.

Dahl-Jensen, D., Mosegaard, K., Gundestrup, N., Clow, G., Johnsen, S., Hansen, A., & Balling, N. (1998). Past temperatures directly from the Greenland Ice Sheet. *Science*, 282(5387), 268–271.

Dansgaard, W., Johnsen, S., Clausen, H., Dahl-Jensen, D., Gundestrup, N., Hammer, C., Hvidberg, C., Steffensen, J., Sveinbjörnsdottir, A., Jouzel, J., et al. (1993). Evidence for general instability of past climate from a 250-kyr ice-core record. *Nature*, 364(6434), 218.

Dansgaard, W., Johnsen, S., Møller, J., & Langway, C. (1969). One thousand centuries of climatic record from Camp Century on the Greenland ice sheet. *Science*, 166(3903), 377–380.

Dawes, P. (2009). The bedrock geology under the inland ice: the next major challenge for Greenland mapping. *Geological Survey of Denmark and Greenland Bulletin*, 17(5).

Dow, C., Werder, M., Babonis, G., Nowicki, S., Walker, R., Csathó, B., & Morlighem, M. (2018). Dynamics of active subglacial lakes in Recovery Ice Stream. *Journal of Geophysical Research: Earth Surface*, 123(4), 837–850.

Dyke, L. M., Hughes, A. L., Murray, T., Hiemstra, J. F., Andresen, C. S., & Rodés, Á. (2014). Evidence for the asynchronous retreat of large outlet glaciers in southeast Greenland at the end of the last glaciation. *Quaternary Science Reviews*, 99, 244–259.

Elith, J., Leathwick, J., & Hastie, T. (2008). A working guide to boosted regression trees. *Journal of Animal Ecology*, 77(4), 802–813.

Enderlin, E., Howat, I., Jeong, S., Noh, M., Van Angelen, J., & Van Den Broeke, M. (2014). An improved mass budget for the Greenland ice sheet. *Geophysical Research Letters*, 41(3), 866–872.

Erokhina, O., Rogozhina, I., Prange, M., Bakker, P., Bernales, J., Paul, A., & Schulz, M. (2017). Dependence of slope lapse rate over the Greenland Ice Sheet on background climate. *Journal of Glaciology*, 63(239), 568.

Ettema, J., Van den Broeke, M., Meijgaard, E., van, Berg, W., Box, J., & Steffen, K. (2010). Climate of the Greenland ice sheet using a high-resolution climate model–Part 1: Evaluation. *The Cryosphere*, 4(4), 511–527.

Fahnestock, M., Abdalati, W., Joughin, I., Brozena, J., & Gogineni, P. (2001). High geothermal heat flow, basal melt, and the origin of rapid ice flow in Central Greenland. *Science*, 294(5550), 2338–2342.

Fausto, R., Ahlstrøm, A., Van As, D., Bøggild, C., & Johnsen, S. (2009). A new present-day temperature parameterization for Greenland. *Journal of Glaciology*, 55(189), 95–105.

Fettweis, X., Franco, B., Tedesco, M., van Angelen, J. H., Lenaerts, J. T. M., van den Broeke, M. R., & Gallée, H. (2013). Estimating the Greenland ice sheet surface mass balance contribution to future sea level rise using the regional atmospheric climate model MAR. *The Cryosphere*, 7(2), 469–489.

Fisher, A., Mankoff, K., Tulaczyk, S., Tyler, S., Foley, N., et al. (2015). High geothermal heat flux measured below the West Antarctic Ice Sheet. *Science advances*, 1(6), e1500093.

Fowler, A. (1992). Modelling ice sheet dynamics. *Geophysical & Astrophysical Fluid Dynamics*, 63(1-4), 29–65.

Fox Maule, C., Purucker, M., & Olsen, N. (2009). Inferring magnetic crustal thickness and geothermal heat flux from crustal magnetic field models. *Danish Climate Centre Report*, (pp. 09–09).

Fretwell, P., Pritchard, H. D., Vaughan, D. G., Bamber, J. L., Barrand, N. E., Bell, R., Bianchi, C., Bingham, R. G., Blankenship, D. D., Casassa, G., Catania, G., Callens, D., Conway, H., Cook, A. J., Corr, H. F. J., Damaske, D., Damm, V., Ferraccioli, F., Forsberg, R., Fujita, S., Gim, Y., Gogineni, P., Griggs, J. A., Hindmarsh, R. C. A., Holmlund, P., Holt, J. W., Jacobel, R. W., Jenkins, A., Jokat, W., Jordan, T., King, E. C., Kohler, J., Krabill, W., Riger-Kusk, M., Langley, K. A., Leitchenkov, G., Leuschen, C., Luyendyk, B. P., Matsuoka, K., Mouginot, J., Nitsche, F. O., Nogi, Y., Nost, O. A., Popov, S. V., Rignot, E., Rippin, D. M., Rivera, A., Roberts, J., Ross, N., Siegert, M. J., Smith, A. M., Steinhage, D., Studinger, M., Sun, B., Tinto, B. K., Welch, B. C., Wilson, D., Young, D. A., Xiangbin, C., & Zirizzotti, A. (2013). Bedmap2: improved ice bed, surface and thickness datasets for antarctica. *The Cryosphere*, 7(1), 375–393.

Friedman, J., Hastie, T., & Tibshirani, R. (2001). *The Elements of Statistical Learning*, volume 1. Springer series in statistics Springer, Berlin.

Friedman, J. H. (2001). Greedy function approximation: a gradient boosting machine. *Annals of statistics*, (pp. 1189–1232).

Gautschi, W. (1998). The incomplete gamma functions since Tricomi. In *In Tricomi's Ideas and Contemporary Applied Mathematics, Atti dei Convegni Lincei, n. 147, Accademia Nazionale dei Lincei*: Citeseer.

Glen, J. (1955). The creep of polycrystalline ice. *Proceedings of the Royal Society of London. Series A. Mathematical and Physical Sciences*, 228(1175), 519–538.

Gogineni, S., Tammana, D., Braaten, D., Leuschen, C., Akins, T., Legarsky, J., Kanagaratnam, P., Stiles, J., Allen, C., & Jezek, K. (2001). Coherent radar ice thickness measurements over the Greenland ice sheet. *Journal of Geophysical Research: Atmospheres*, 106(D24), 33761–33772.

Goldstein, A., Kapelner, A., Bleich, J., & Pitkin, E. (2015). Peeking inside the black box: Visualizing statistical learning with plots of individual conditional expectation. *Journal of Computational and Graphical Statistics*, 24(1), 44–65.

Gooch, B., Young, D., & Blankenship, D. (2016). Potential groundwater and heterogeneous heat source contributions to ice sheet dynamics in critical submarine basins of East Antarctica. *Geochemistry, Geophysics, Geosystems*, 17(2), 395–409.

Gosnold, W. (2011). The global heat flow database. `http://www.heatflow.und.edu/index2.html`. Accessed: 2016-09-30.

Goutorbe, B., Poort, J., Lucazeau, F., & Raillard, S. (2011). Global heat flow trends resolved from multiple geological and geophysical proxies. *Geophysical Journal International*, 187(3), 1405–1419.

Greve, R. (1997). Application of a polythermal three-dimensional ice sheet model to the Greenland ice sheet: response to steady-state and transient climate scenarios. *Journal of Climate*, 10(5), 901–918.

Greve, R. (2005). Relation of measured basal temperatures and the spatial distribution of the geothermal heat flux for the Greenland Ice Sheet. *Annals of Glaciology*, 42(1), 424–432.

Greve, R. & Blatter, H. (2009). *Dynamics of ice sheets and glaciers*. Springer Science & Business Media.

Greve, R. & Blatter, H. (2016). Comparison of thermodynamics solvers in the polythermal ice sheet model SICOPOLIS. *Polar Science*, 10(1), 11–23.

Greve, R. & Herzfeld, U. (2013). Resolution of ice streams and outlet glaciers in large-scale simulations of the Greenland ice sheet. *Annals of Glaciology*, 54(63), 209–220.

Greve, R. & Hutter, K. (1995). Polythermal three-dimensional modelling of the Greenland ice sheet with varied geothermal heat flux. *Annals of Glaciology*, 21, 8–12.

Gundestrup, N. & Hansen, B. (1984). Bore-hole survey at Dye 3, south Greenland. *Journal of Glaciology*, 30(106), 282–288.

Guyon, I., Weston, J., Barnhill, S., & Vapnik, V. (2002). Gene selection for cancer classification using support vector machines. *Machine learning*, 46(1), 389–422.

Hanna, E., Huybrechts, P., Janssens, I., Cappelen, J., Steffen, K., & Stephens, A. (2005). Runoff and mass balance of the Greenland ice sheet: 1958–2003. *Journal of Geophysical Research: Atmospheres*, 110(D13).

Harig, C. & Simons, F. (2016). Ice mass loss in Greenland, the gulf of Alaska, and the Canadian Archipelago: Seasonal cycles and decadal trends. *Geophysical Research Letters*, 43(7), 3150–3159.

Harper, J., Hubbard, A., & Ruskeeniemi, T. (2011). The Greenland Analogue Project. Yearly report 2010. *Technical Report - Swedish Nuclear Fuel and Waste Management Co.*

Hartmann, J. & Moosdorf, N. (2012). The new global lithological map database GLiM: A representation of rock properties at the Earth surface. *Geochemistry, Geophysics, Geosystems*, 13(12).

Henriksen, N., Higgins, A., Kalsbeek, F., & Pulvertaft, T. (2009). Greenland from archaean to quaternary. *Geological Survey of Denmark and Greenland Bulletin*, 18, 1–13.

Hindmarsh, R. (1999). On the numerical computation of temperature in an ice sheet. *Journal of Glaciology*, 45(151), 568–574.

Hindmarsh, R. (2009). Consistent generation of ice-streams via thermo-viscous instabilities modulated by membrane stresses. *Geophysical Research Letters*, 36(6).

Hindmarsh, R., Gwendolyn, J., & Parrenin, F. (2009). A large-scale numerical model for computing isochrone geometry. *Annals of Glaciology*, 50(51), 130–140.

Hindmarsh, R. C. & Le Meur, E. (2001). Dynamical processes involved in the retreat of marine ice sheets. *Journal of Glaciology*, 47(157), 271–282.

Hjartarson, Á. (2015). Heat Flow in Iceland. *Proceedings World Geothermal Congress, Melbourne, Australia*.

Hooke, R. (1981). Flow law for polycrystalline ice in glaciers' comparison of theoretical predictions, laboratory data, and field. *Reviews of Geophysics and Space Physics*, 19(4), 664–672.

Hutter, K. (1983). *Theoretical glaciology: material science of ice and the mechanics of glaciers and ice sheets*, volume 1. Springer.

Iken, A. & Bindschadler, R. (1986). Combined measurements of subglacial water pressure and surface velocity of Findelengletscher, Switzerland: conclusions about drainage system and sliding mechanism. *Journal of Glaciology*, 32(110), 101–119.

Imbrie, J., Hays, J. D., Martinson, D. G., McIntyre, A., Mix, A. C., Morley, J. J., Pisias, N. G., Prell, W. L., & Shackleton, N. J. (1984). The orbital theory of pleistocene climate: Support from a revised chronology of the marine delta18 o record. In *Milankovitch and climate: Understanding the response to astronomical forcing*, volume 1 (pp. 269).

Jezek, K., Johnson, J., Drinkwater, M., Macelloni, G., Tsang, L., Aksoy, M., & Durand, M. (2015). Radiometric approach for estimating relative changes in intraglacier average temperature. *IEEE Transactions on Geoscience and Remote Sensing*, 53(1), 134–143.

Jordan, T., Williams, C., Schroeder, D., Martos, Y., Cooper, M., Siegert, M., Paden, J., Huybrechts, P., & Bamber, J. (2018). A constraint upon the basal water distribution and thermal state of the Greenland Ice Sheet from radar bed echoes. *The Cryosphere*, 12(9), 2831–2854.

Joughin, I., Smith, B., Howat, I., Scambos, T., & Moon, T. (2010). MEaSUREs Greenland ice sheet velocity map from InSAR data. *National Snow and Ice Data Center., Boulder, Colorado USA. doi: nsidc-0478.001*.

Kaban, M., Schwintzer, P., & Reigber, C. (2004). A new isostatic model of the lithosphere and gravity field. *Journal of Geodesy*, 78(6), 368–385.

Kobashi, T., Kawamura, K., Severinghaus, J., Barnola, J., Nakaegawa, T., Vinther, B., Johnsen, S., & Box, J. (2011). High variability of Greenland surface temperature over the past 4000 years estimated from trapped air in an ice core. *Geophysical Research Letters*, 38(21).

Langley, K., Tinto, K., Block, A., Bell, R., Kohler, J., & Scambos, T. (2014). Onset of fast ice flow in Recovery Ice Stream, East Antarctica: a comparison of potential causes. *Journal of Glaciology*, 60(223), 1007.

Langseth, M. G., Clark Jr, S. P., Chute Jr, J. L., Keihm, S. J., & Wechsler, A. E. (1972). Heat flow experiment. *Technical Report*.

Larour, E., Morlighem, M., Seroussi, H., Schiermeier, J., & Rignot, E. (2012a). Ice flow sensitivity to geothermal heat flux of Pine Island Glacier, Antarctica. *Journal of Geophysical Research: Earth Surface (2003–2012)*, 117(F4).

Larour, E., Seroussi, H., Morlighem, M., & Rignot, E. (2012b). Continental scale, high order, high spatial resolution, ice sheet modeling using the Ice Sheet System Model (ISSM). *Journal of Geophysical Research: Earth Surface (2003–2012)*, 117(F1).

Laske, G., Masters, G., Ma, Z., & Pasyanos, M. (2013). Update on CRUST1.0 1-degree global model of Earth's crust. In *Geophysical Research Abstracts*, volume 15 (pp. 2658).

Le Meur, E. & Huybrechts, P. (1996). A comparison of different ways of dealing with isostasy: examples from modelling the Antarctic ice sheet during the last glacial cycle. *Annals of Glaciology*, 23, 309–317.

Logg, A., Mardal, K., & Wells, G. (2012). *Automated solution of differential equations by the finite element method: The FEniCS book*, volume 84. Springer Science & Business Media.

MacAyeal, D. (1993). Binge/purge oscillations of the Laurentide ice sheet as a cause of the North Atlantic's Heinrich events. *Paleoceanography*, 8(6), 775–784.

MacAyeal, D. R. (1989). Large-scale ice flow over a viscous basal sediment: Theory and application to ice stream B, Antarctica. *Journal of Geophysical Research: Solid Earth*, 94(B4), 4071–4087.

MacGregor, J. A., Fahnestock, M. A., Catania, G. A., Aschwanden, A., Clow, G. D., Colgan, W. T., Gogineni, S. P., Morlighem, M., Nowicki, S. M., Paden, J. D., et al. (2016). A synthesis of the basal thermal state of the Greenland Ice Sheet. *Journal of Geophysical Research: Earth Surface*, 121(7), 1328–1350.

Mareschal, J. & Jaupart, C. (2004). Variations of surface heat flow and lithospheric thermal structure beneath the North American craton. *Earth and Planetary Science Letters*, 223(1), 65–77.

Martos, Y., Jordan, T., Catalan, M., Jordan, T., Bamber, J., & Vaughan, D. (2018). Geothermal heat flux reveals the iceland hotspot track underneath Greenland. *Geophysical Research Letters*.

Maus, S., Sazonova, T., Hemant, K., Fairhead, J., & Ravat, D. (2007). National Geophysical Data Center candidate for the world digital magnetic anomaly map. *Geochemistry, Geophysics, Geosystems*, 8(6).

Meierbachtol, T. W., Harper, J. T., Johnson, J. V., Humphrey, N. F., & Brinkerhoff, D. J. (2015). Thermal boundary conditions on western Greenland: Observational constraints and impacts on the modeled thermomechanical state. *Journal of Geophysical Research: Earth Surface*, 120(3), 623–636.

Mordret, A. (2018). Uncovering the Iceland Hot Spot Track Beneath Greenland. *Journal of Geophysical Research: Solid Earth*, 123(6), 4922–4941.

Morland, L. (1984). Thermomechanical balances of ice sheet flows. *Geophysical & Astrophysical Fluid Dynamics*, 29(1-4), 237–266.

Naslund, J., Jansson, P., Fastook, J. L., Johnson, J., & Andersson, L. (2005). Detailed spatially distributed geothermal heat-flow data for modeling of basal temperatures and meltwater production beneath the Fennoscandian ice sheet. *Annals of Glaciology*, 40(1), 95–101.

Nye, J. (1952). The mechanics of glacier flow. *Journal of Glaciology*, 2(12), 82–93.

Oswald, G. & Gogineni, S. (2008). Recovery of subglacial water extent from Greenland radar survey data. *Journal of Glaciology*, 54(184), 94–106.

Oswald, G., Rezvanbehbahani, S., & Stearns, L. (2018). Radar evidence of ponded subglacial water in Greenland. *Journal of Glaciology*, (pp. 1–19).

Palmer, S., Dowdeswell, J., Christoffersen, P., Young, D., Blankenship, D., Greenbaum, J., Benham, T., Bamber, J., & Siegert, M. (2013). Greenland subglacial lakes detected by radar. *Geophysical Research Letters*, 40(23), 6154–6159.

Pasyanos, M. E., Masters, T. G., Laske, G., & Ma, Z. (2014). LITHO1.0: An updated crust and lithospheric model of the Earth. *Journal of Geophysical Research: Solid Earth*, 119(3), 2153–2173.

Payne, A. (1995). Limit cycles in the basal thermal regime of ice sheets. *Journal of Geophysical Research: Solid Earth*, 100(B3), 4249–4263.

Petrunin, A., Rogozhina, I., Vaughan, A., Kukkonen, I., Kaban, M., Koulakov, I., & Thomas, M. (2013). Heat flux variations beneath central Greenland's ice due to anomalously thin lithosphere. *Nature Geoscience*, 6(9), 746–750.

Pettit, E. & Waddington, E. (2003). Ice flow at low deviatoric stress. *Journal of Glaciology*, 49(166), 359–369.

Phipps Morgan, J. & Holtzman, B. (2005). Vug waves: A mechanism for coupled rock deformation and fluid migration. *Geochemistry, Geophysics, Geosystems*, 6(8).

Pittard, M., Galton-Fenzi, B., Roberts, J., & Watson, C. (2016). Organization of ice flow by localized regions of elevated geothermal heat flux. *Geophysical Research Letters*, 43(7), 3342–3350.

Pollack, H., Hurter, S., & Johnson, J. (1993). Heat flow from the earth's interior: Analysis of the global data set. *Reviews of Geophysics*, 31(3), 267–280.

Portnov, A., Vadakkepuliyambatta, S., Mienert, J., & Hubbard, A. (2016). Ice-sheet-driven methane storage and release in the Arctic. *Nature communications*, 7, 10314.

Poupinet, G. & Shapiro, N. (2009). Worldwide distribution of ages of the continental lithosphere derived from a global seismic tomographic model. *Lithos*, 109(1), 125–130.

Raymond, C. (1983). Deformation in the vicinity of ice divides. *Journal of Glaciology*, 29(103), 357–373.

Reguzzoni, M., Sampietro, D., & Sansò, F. (2013). Global Moho from the combination of the CRUST2.0 model and GOCE data. *Geophysical Journal International*, 195(1), 222–237.

Rezvanbehbahani, S., Stearns, L. A., Kadivar, A., Walker, J. D., & van der Veen, C. (2017). Predicting the Geothermal Heat Flux in Greenland: A Machine Learning Approach. *Geophysical Research Letters*, 44(24), 12,271–12,279.

Rezvanbehbahani, S., van der Veen, C. J., & Stearns, L. A. (2019). An improved analytical solution for the temperature profile of ice sheets. *Journal of Geophysical Research: Earth Surface*.

Rignot, E., Mouginot, J., & Scheuchl, B. (2011). Ice flow of the Antarctic ice sheet. *Science*, 333(6048), 1427–1430.

Rippin, D. M. (2013). Bed roughness beneath the Greenland ice sheet. *Journal of Glaciology*, 59(216), 724–732.

Robin, G. (1955). Ice movement and temperature distribution in glaciers and ice sheets. *Journal of Glaciology*, 2(18), 523–532.

Rogozhina, I., Hagedoorn, J., Martinec, Z., Fleming, K., Soucek, O., Greve, R., & Thomas, M. (2012). Effects of uncertainties in the geothermal heat flux distribution on the Greenland Ice Sheet: An assessment of existing heat flow models. *Journal of Geophysical Research: Earth Surface*, 117(F2).

Rogozhina, I., Petrunin, A., Vaughan, A., Steinberger, B., Johnson, J., Kaban, M., Calov, R., Rickers, F., Thomas, M., & Koulakov, I. (2016). Melting at the base of the Greenland Ice Sheet explained by Iceland hotspot history. *Nature Geoscience*, 9(5), 366–369.

Sass, J., Nielsen, B. L., Wollenberg, H. A., & Munroe, R. J. (1972). Heat flow and surface radioactivity at two sites in South Greenland. *Journal of Geophysical Research*, 77(32), 6435–6444.

Schlegel, N., Larour, E., Seroussi, H., Morlighem, M., & Box, J. (2015). Ice discharge uncertainties in Northeast Greenland from boundary conditions and climate forcing of an ice flow model. *Journal of Geophysical Research: Earth Surface*, 120(1), 29–54.

Schroeder, D., Blankenship, D., & Young, D. (2013). Evidence for a water system transition beneath Thwaites Glacier, West Antarctica. *Proceedings of the National Academy of Sciences*, 110(30), 12225–12228.

Sclater, J., Jaupart, C., & Galson, D. (1980). The heat flow through oceanic and continental crust and the heat loss of the earth. *Reviews of Geophysics*, 18(1), 269–311.

Şengör, A. C. & Natal'in, B. A. (2001). Rifts of the world. *Geological Society of America Special Papers*, 352, 389–482.

Sergienko, O., Creyts, T., & Hindmarsh, R. (2014). Similarity of organized patterns in driving and basal stresses of Antarctic and Greenland ice sheets beneath extensive areas of basal sliding. *Geophysical Research Letters*, 41(11), 3925–3932.

Seroussi, H., Ivins, E. R., Wiens, D. A., & Bondzio, J. (2017). Influence of a West Antarctic

mantle plume on ice sheet basal conditions. *Journal of Geophysical Research: Solid Earth*. 2017JB014423.

Seroussi, H., Morlighem, M., Rignot, E., Khazendar, A., Larour, E., & Mouginot, J. (2013). Dependence of century-scale projections of the greenland ice sheet on its thermal regime. *Journal of Glaciology*, 59(218), 1024–1034.

Shapiro, N. & Ritzwoller, M. (2002). Monte-Carlo inversion for a global shear-velocity model of the crust and upper mantle. *Geophysical Journal International*, 151(1), 88–105.

Shapiro, N. & Ritzwoller, M. (2004). Inferring surface heat flux distributions guided by a global seismic model: particular application to Antarctica. *Earth and Planetary Science Letters*, 223(1), 213–224.

Siegert, M. (2000). Antarctic subglacial lakes. *Earth-Science Reviews*, 50(1), 29–50.

Solomon, S., Qin, D., Manning, M., Averyt, K., & Marquis, M. (2007). *Climate change 2007-the physical science basis: Working group I contribution to the fourth assessment report of the IPCC*, volume 4. Cambridge university press.

Steffen, K. & Box, J. (2001). Surface climatology of the Greenland ice sheet: Greenland Climate Network 1995–1999. *Journal of Geophysical Research: Atmospheres*, 106(D24), 33951–33964.

Stevens, N., Parizek, B., & Alley, R. (2016). Enhancement of volcanism and geothermal heat flux by ice-age cycling: A stress modeling study of Greenland. *Journal of Geophysical Research: Earth Surface*, 121(8), 1456–1471.

USGS (1997). Geologic Province and Thermo-Tectonic Age Maps. `https://earthquake.usgs.gov/data/crust/maps.php`. Accessed: 2016-09-30.

Van den Broeke, M., Bamber, J., Ettema, J., Rignot, E., Schrama, E., van de Berg, W., van Meijgaard, E., Velicogna, I., & Wouters, B. (2009). Partitioning recent Greenland mass loss. *Science*, 326(5955), 984–986.

Van den Broeke, M., Bamber, J., Lenaerts, J., & Rignot, E. (2011). Ice sheets and sea level: Thinking outside the box. *Surveys in Geophysics*, 32(4-5), 495–505.

Van den Broeke, M., Enderlin, E., Howat, I., Kuipers Munneke, P., Noël, B., Jan Van De Berg, W., Van Meijgaard, E., & Wouters, B. (2016). On the recent contribution of the Greenland ice sheet to sea level change. *The Cryosphere*, 10(5), 1933–1946.

Van der Veen, C. (2013). *Fundamentals of Glacier Dynamics*. Boca Raton FL : CRC Press.

Van der Veen, C., Leftwich, T., von Frese, R., Csatho, B., & Li, J. (2007). Subglacial topography and geothermal heat flux: Potential interactions with drainage of the Greenland ice sheet. *Geophysical Research Letters*, 34(12).

Van Liefferinge, B. & Pattyn, F. (2013). Using ice-flow models to evaluate potential sites of million year-old ice in Antarctica. *Climate of the Past*, 9(5), 2335–2345.

Van Liefferinge, B., Pattyn, F., Cavitte, M., Karlsson, N., Young, D., Sutter, J., & Eisen, O. (2018). Promising Oldest Ice sites in East Antarctica based on thermodynamical modelling. *The Cryosphere*, 12(8), 2773–2787.

Velicogna, I., Sutterley, T., & Van Den Broeke, M. (2014). Regional acceleration in ice mass loss from Greenland and Antarctica using GRACE time-variable gravity data. *Geophysical Research Letters*, 41(22), 8130–8137.

Vialov, S. (1958). Regularities of lacial shields movement and the theory of plastic viscous flow. *Physics of the Movements of Ice IAHS*, 47, 266–275.

Zhu, H., Petra, N., Stadler, G., Isaac, T., Hughes, T., & Ghattas, O. (2016). Inversion of geothermal heat flux in a thermomechanically coupled nonlinear Stokes ice sheet model. *The Cryosphere*, 10(4), 1477–1494.

Zotikov, I. (1986). *The thermophysics of glaciers*. Kluwer Academic Publishers, Norwell, MA.

Appendix A

Supplementary Information for Chapter 3

A.1 Model Description

In this section we describe the gradient boosted regression tree (GBRT) model used to produce the GHF predictions presented in the main text. Since GBRT is not a well-known technique in geospatial statistics, we also provide a brief overview of its inner workings.

A.1.1 Problem Setting

Our problem is a typical standard regression problem in which we wish to predict a continuous variable, here GHF, from a vector of continuous or categorical *features*. The *training data* is a collection of observations of the form $(\mathbf{x}, y)$, called *samples*, where $\mathbf{x} = (x_1, \ldots, x_p)$ is a feature vector belonging to a p-dimensional feature space and y is the quantity of interest for prediction. In our case, $\mathbf{x}$ contains p geologic features and y is the GHF value at a given latitude and longitude. Given n such observations:

$$\Big\{(\mathbf{x}_1, y_1), \ldots, (\mathbf{x}_n, y_n)\Big\},$$

we wish to find a *predictor* $f : \mathbb{R}^p \to \mathbb{R}$ relating feature vectors to the quantity of interest y. This is achieved by formulating the problem of finding f as an optimization problem over a pre-specified family, $\mathbb{F}$, of possible predictors. In other words, we seek an optimal (in a sense to be determined) function f in $\mathbb{F}$.

For a given predictor f we denote its predictions over the training data by

$$\widehat{\mathbf{y}} = (\hat{y}_1, \ldots, \hat{y}_n) := \big(f(\mathbf{x}_1), \ldots, f(\mathbf{x}_n)\big),$$

which we will refer to as the *prediction vector*. Goodness of fit is formulated in terms of a *loss function* $L : \mathbb{R}^n \to \mathbb{R}^+$ which assigns a measure of error $L(\widehat{\mathbf{y}})$ to the prediction vector with respect to observed values $\mathbf{y} = (y_1, \ldots, y_n)$. We will be using the common *sum of squares* loss function, also commonly used in linear regression, which is given by:

$$L(\widehat{\mathbf{y}}) = \sum_{k=1}^{n} |\hat{y}_k - y_k|^2.$$

Finally, our task for fitting a predictor f to the given samples is to solve the optimization problem:

$$\min_{f \in \mathbb{F}} L(\widehat{\mathbf{y}}) = \min_{f \in \mathbb{F}} \sum_{k=1}^{n} |y_k - f(x_k)|^2.$$

The description of a statistical model includes the specification of the family $\mathbb{F}$ of predictors together with an algorithm that finds the optimal predictor f in $\mathbb{F}$ with respect to L. In the remainder of this section we describe ordinary regression trees and GBRT as such models. For this discussion, we will assume a fixed set of n training samples $\{(\mathbf{x}_k, y_k)\}_{k=1}^n$ is given.

A.1.2 Regression Trees

A regression tree partitions the feature space into a collection of box-like regions D_i and assigns a constant value $\hat{y}_i$ to each region. In other words, each such region is the subset of the feature space constrained by conditions of the form $x_k > T$ or $x_k < T$ where each x_k is an individual feature. It is important to note that once a region D_i is chosen, the optimal constant value $\hat{y}_i$ is directly determined from the expression of the loss function L. For instance when using sum of squares loss, the optimal constant assignment to D_i is simply the average value of y in D_i.

Here, the predictor family $\mathbb{F}$ is the collection of all such piecewise constant functions. An

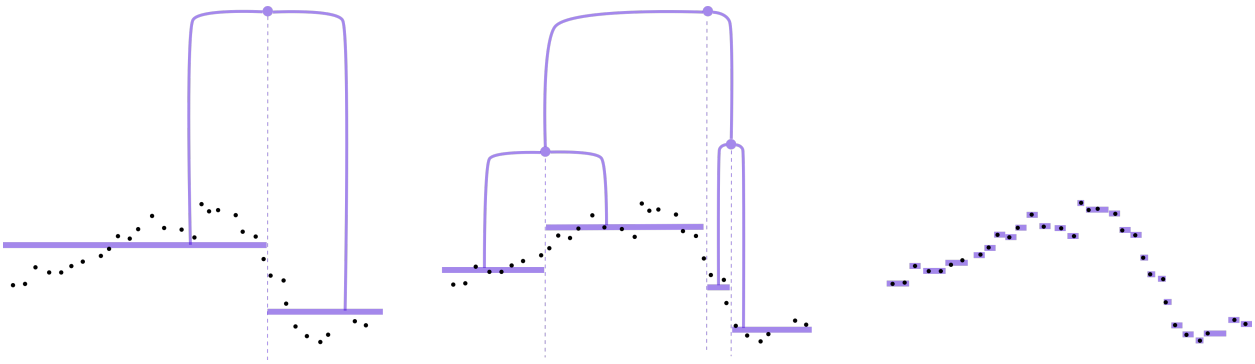

Figure A.1: Schematic depiction of a one dimensional regression tree (i.e. $\mathbf{x}$ contains a single feature) after one (left) and two (middle) iterations. Arbitrarily small training loss can be attained (right) by a regression tree which is overfit to training data.

individual predictor $f \in \mathbb{F}$ is identified by the specification of its box-like regions as well as the value it assigns to each region. In general, minimizing the loss function over the entire family $\mathbb{F}$ is intractable and instead, an approximating algorithm is typically employed which motivates its interpretation as a regression tree (RT; algorithm 1). The heuristic proceeds as follows: Starting with a single region $(\mathbb{R}^p, \hat{y})$ and until a certain depth is achieved, grow a tree by partitioning some region D by some condition $x_k < T$ and replacing the corresponding node in the tree with a feature comparison question node "$x_k > T$?" with two child nodes:

$$D_< = D \cap \{x_k < T\}, \quad D_> = D \cap \{x_k > T\}$$

At any time the constant regions of the predictor are simply the terminal nodes of the tree and are all candidates for being partitioned. The contribution of each such partition over feature k of a region D is a reduction in error given by

$$e^2(D,k,T) = L(\hat{y}_D) - [L(\hat{y}_{D_<}) + L(\hat{y}_{D_>})]$$

where each loss term $L(\cdot)$ is evaluated over its corresponding region $D, D_{k,<}, D_{k,>}$. Predictors produced by this heuristic can be viewed as decision trees in which each internal (non-terminal) node is a question of the form "$x_k > T$?". When a given predictor calculates the prediction for a

given feature vector $\mathbf{x} = (x_1, \ldots, x_p)$ it descends down a path, starting from the root and arriving at a terminal node, by answering the comparison question posed at each internal node and moving to either of its children based on the answer for the given feature vector $\mathbf{x}$. The terminal nodes are simply the regions D_i and are assigned constant values $\hat{y}_i$ (Figure A.1).

Since individual features are treated separately in Algorithm 1, it is clear that regression trees pose no difficulty when the feature set contains both continuous and categorical variables.

Algorithm 1 RT (Ordinary Regression Tree)

$f = \{(\mathbb{R}^p, \hat{y})\}$ ▷ The starting region is the entire feature space
while True **do**
  $D, k, T \leftarrow$ optimal choice maximizing the reduction $e^2(D, k, T)$ in error
  $D_<, D_> \leftarrow$ partition D along the x_k axis with threshold T
  $\hat{y}_<, \hat{y}_> \leftarrow$ optimal constants for regions $D_<, D_>$
  $D \leftarrow$ comparison question "$x_k > T$?"
  Children of $D \leftarrow (D_<, \hat{y}_<), (D_>, \hat{y}_>)$
  if depth$(f) > J$ **then** ▷ J is the maximum tree depth
   return f
  end if
end while

A.1.3 Boosted Regression

Boosting is a general heuristic in statistical learning which proposes combining multiple predictors, referred to as *weak learners*, into a stronger predictor (Friedman, 2001). Given a family $\mathbb{F}$, a boosted predictor F based on $\mathbb{F}$ is a linear combination of predictors in $\mathbb{F}$, that is $F = \alpha_1 f_1 + \ldots + \alpha_m f_m$ for some $f_i \in \mathbb{F}$ and $\alpha_i \in \mathbb{R}$. When the family $\mathbb{F}$ is closed under scalar multiplication (as is the case with regression trees), we can simplify the general form of a boosted predictor to $F = f_1 + \ldots + f_m$ for some $f_i \in \mathbb{F}$. One can describe the problem of training a boosted model in similar terms as before: we seek the optimal predictor F in the boosted predictor family

$$\text{span}(\mathbb{F}) = \left\{ F = f_1 + \ldots + f_m \,; m \in \mathbb{N},\ f_i \in \mathbb{F} \right\}$$

such that the training loss $L(\widehat{\mathbf{y}})$ of the prediction vector $\widehat{\mathbf{y}} = \big(F(\mathbf{x}_1), \ldots, F(\mathbf{x}_n)\big)$ is minimized. In a boosted regression tree model the underlying predictor family $\mathbb{F}$ consists of ordinary regression trees. However, there are many algorithms for approximating the optimal boosted predictor. GBRT (Algorithm 2) is one such algorithm which is shown to contain many earlier boosting algorithms as a special case. In gradient boosting with sum of squares loss, at each stage a weak learner f_i is fit to the current *residual* vector which is the difference between known values $\mathbf{y}$ and the current prediction vector $\hat{\mathbf{y}}$ produced by $f_1 + \ldots + f_{i-1}$.

Our statistical model can thus be summarized as follows; GBRT (Algorithm 2) is used to approximate the optimal boosted regression tree $f_1 + \ldots + f_M$, where f_i are regression trees of maximum depth J, that minimize the sum of squares loss over corresponding residuals r_i. Typical values for J are between 2 and 9 (Friedman et al., 2001, section 11.9.2). In all plots presented in the main text and here we have used $J = 4$ and $M = 1000$ (see Figure A.2) with the exception of Figure 5 of main text (feature importances) for which $J = 8$ was used to avoid a handful of features (limited by the number of internal nodes in the tree) controlling all partitions in all trees.

Algorithm 2 GBRT (Gradient Boosted Regression Tree with sum of squares loss)

$i \leftarrow 0$ ▷ number of weak learners trained so far

$\mathbf{r} \leftarrow \mathbf{y}$ ▷ n-dimensional vector of residuals

while $i < M$ **do** ▷ M is the number of weak learners to be trained

  $f \leftarrow \text{RT}(\mathbf{r})$ ▷ train a RT (weak learner) with $\left\{ (\mathbf{x}_1, r_1), \ldots, (\mathbf{x}_n, r_n) \right\}$

  $f_i = \nu f$ ▷ regularization via shrinkage (see section A.1.4)

  $i \leftarrow i + 1$

  $\mathbf{r} \leftarrow \mathbf{r} - \Big(f_i(\mathbf{x}_1), \ldots, f_i(\mathbf{x}_n) \Big)$ ▷ update residuals

end while

return $f_1 + f_2 + \ldots + f_M$

Boosting has proved to be a fruitful strategy in various settings for multiple reasons. First, by extending the family of predictors from $\mathbb{F}$ to span($\mathbb{F}$), it allows for lower bias and variance. For instance, if $\mathbb{F}$ is the very limited family of step functions (i.e regression trees of depth 1), the extended class span($\mathbb{F}$) can approximate any function arbitrarily closely. However, this comes with the risk of overfitting which is mitigated through regularization and controlled using cross-validation (see section A.1.4). Furthermore, through the statistical power of averaging, boosting has been shown to increase robustness to noise (see section A.1.6).

A.1.4 Controlling for Overfitting

A crucial difference between optimization problems and statistical modelling is the risk of overfitting. In fact, typically one can find predictors that drive the total training loss to zero (Figures A.1 and A.2). Therefore, the total loss of a predictor on training data is not a good measure of error since it evaluates a predictor based on samples for which it has already been optimized. Instead, the standard procedure is to use a cross-validation scheme in which all available samples are split randomly to a *validation* set

$$V = \left\{ \left(\mathbf{x}_k^{(v)}, y_k^{(v)} \right) \right\}_{k=1}^{m}$$

and a *training* set

$$T = \left\{ \left(\mathbf{x}_k^{(t)}, y_k^{(t)} \right) \right\}_{k=1}^{n-m}.$$

To evaluate a given model (i.e. a predictor class $\mathbb{F}$), one "trains the model" on T, that is, the optimal predictor $f \in \mathbb{F}$ is obtained by minimizing the loss on the training set:

$$\min_{f \in \mathbb{F}} \sum_{k=1}^{n-m} \left\| f\left(\mathbf{x}_k^{(t)} \right) - y_k^{(t)} \right\|^2$$

which is then evaluated on the validation set V by comparing its predictions $f\left(\mathbf{x}_k^{(v)} \right)$ to known values $y_k^{(v)}$ for $k = 1, \ldots, m$. We report two measures of error for any predictor on the validation set

V. The main measure of error is normalized Root Mean Square Error (RMSE) which is a standard scale-invariant measure of error and is consistent with the sum of squares loss function L used to train both GBRT and linear regression. Normalized RMSE is defined to be:

$$\text{Normalized RMSE} = \frac{1}{\langle y_k^{(v)} \rangle_k} \sqrt{\left\langle \left| f\left(\mathbf{x}_k^{(v)}\right) - y_k^{(v)} \right|^2 \right\rangle_k},$$

where $\langle \cdot \rangle_k$ indicates the average of a quantity over different values of the specified index. Therefore, for instance, a normalized RMSE of 0.15 can be interpreted roughly as an average 15% error in predictions. As a more intuitively accessible but less interpretable measure of error we also report r^2 of linear correlation between the m predicted values $\{\hat{y}_k^{(v)}\}_{k=1}^m$ and known true values $\{y_k^{(v)}\}_{k=1}^m$.

A.1.5 Regularization

The standard scheme for constraining the effects of overfitting (also known as *regularization*) for regression trees is to place an upper bound J on individual tree depth. In gradient boosted trees, two additional regularization strategies are typically simultaneously used: **1**) an upper bound M on the number of descent steps (discussed above) and **2**) *shrinkage* which is used to scale down the contributions calculated in each gradient descent step by a parameter $0 < \nu \leq 1$ (line 5 of Algorithm 2). A choice of $\nu = 1$ implies no shrinkage, i.e. non-regularized gradient descent, and smaller values of ν slow down the march towards arbitrarily small training losses, hence limiting the risk of overfitting. Here we have used $\nu = 0.05$ (Friedman et al., 2001, section 11.9.2.).

A.1.6 Stability

An important desired characteristic of a statistical model is its *stability*, namely its robustness to noise. This is crucial in the case of predicting GHF in Greenland; the GHF 'measurements' in Greenland, specifically at ice core locations, are often inferred using Monte Carlo simulations or estimated by matching modeled and measured basal temperatures. Therefore, it is valid to assume

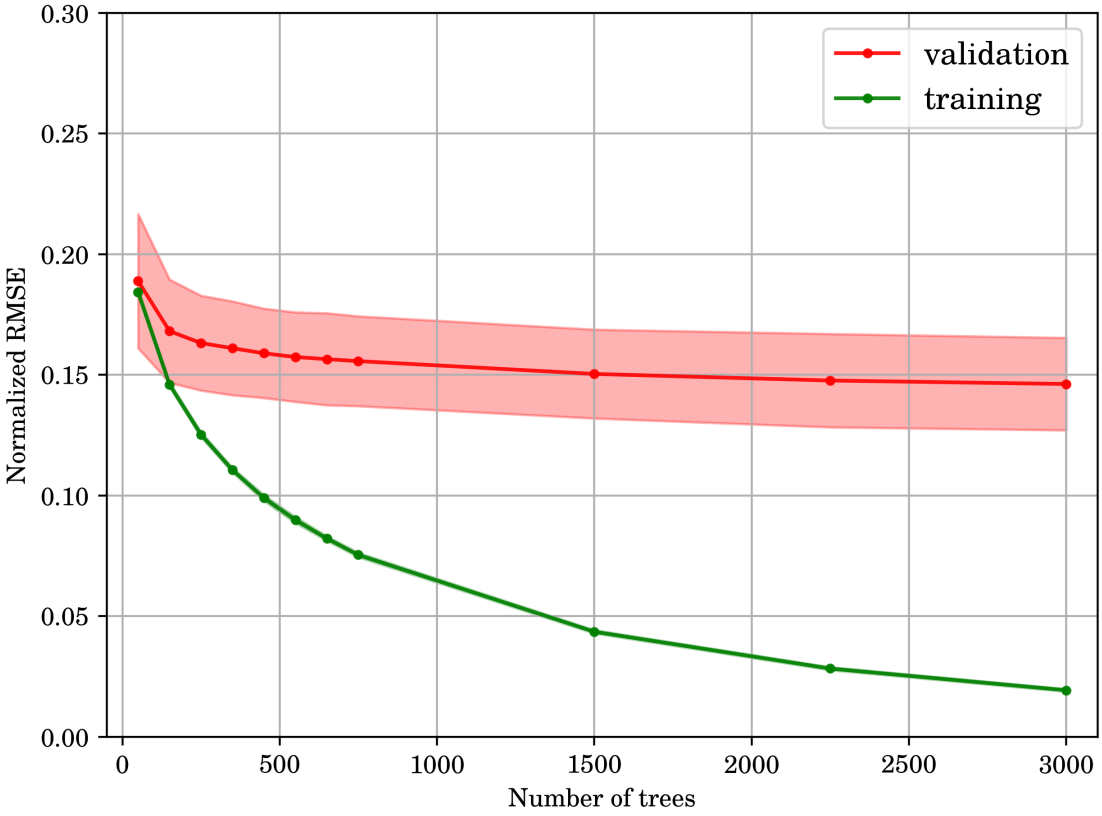

Figure A.2: Testing the possibility of overfitting by GBRT. Normalized RMSE of GBRT over training (green) and validation (red) samples is shown for 50 random ROIs (thin lines) and averaged across ROIs (thick lines) as the number of trees (model complexity) increases (x-axis). Overfitting occurs when training loss continues to decrease but validation error increases as model complexity increases. This plot shows that GBRT with the parameters used here is immune to overfitting. Furthermore, validation error does not decrease significantly beyond 1000 trees which justifies our choice of 1000 estimators for all reported results.

that the GHF inferences in Greenland are highly noisy. We wish our statistical model to be such that small perturbations in known labels $y_1, \ldots, y_n$ does not lead to large perturbations in the trained predictor. This is another domain where boosted regression trees are superior to ordinary regression trees: single trees are known to be unstable while boosted trees tend to be fairly stable as shown in section A.2.2 (see Friedman et al., 2001, section 10.13.1 and Table 10.1).

A.2 Evaluation of GHF Predictions with Limited Local Data

A.2.1 Evaluation of Prediction Error

Our end goal is to predict GHF in Greenland with limited local data, that is, with limited training samples within the ROI. To better capture the performance of predictors with limited local data, we extended the cross-validation scheme described in section A.1.4 with the following parameters:

1. The center $\mathbf{C}$ of ROI specified as a latitude-longitude pair.

2. The radius R of ROI.

3. The density ρ_{ROI} of training samples in the ROI:

$$\rho_{ROI} := \#\left\{(\mathbf{x}_k^{(t)}, y_k) \in T \text{ such that } \mathbf{x}_k^{(t)} \text{ within distance } R \text{ of } \mathbf{C}\right\} \Big/ \pi R^2$$

Given a choice of $\mathbf{C}, R$, and ρ_{ROI}, the training set T contains all samples outside the ROI together with a random collection of n_{ROI} samples within ROI such that:

$$\frac{n_{ROI}}{\pi R^2} \approx \rho_{ROI}$$

Once training-validation partitions are produced, each model (GBRT, linear regression, or the baseline constant predictor) is evaluated exactly as described in section A.1.4 and resulting measures of error (normalized RMSE and r^2) are averaged over all training-validation partitions.

We evaluate the performance of each model with varying ρ_{ROI} and ROI radius R. To assess the effect of ρ_{ROI} we fix the radius to $R = 1300$ km (matching the ROI radius of Greenland) the results of which are shown in Figure 4 of the main text. To assess the effect of R we fix ROI density to $\rho_{ROI} = 11.3 \times 10^{-6}\text{km}^{-2}$ (matching ROI density of Greenland) the results of which are shown in Figure A.3.

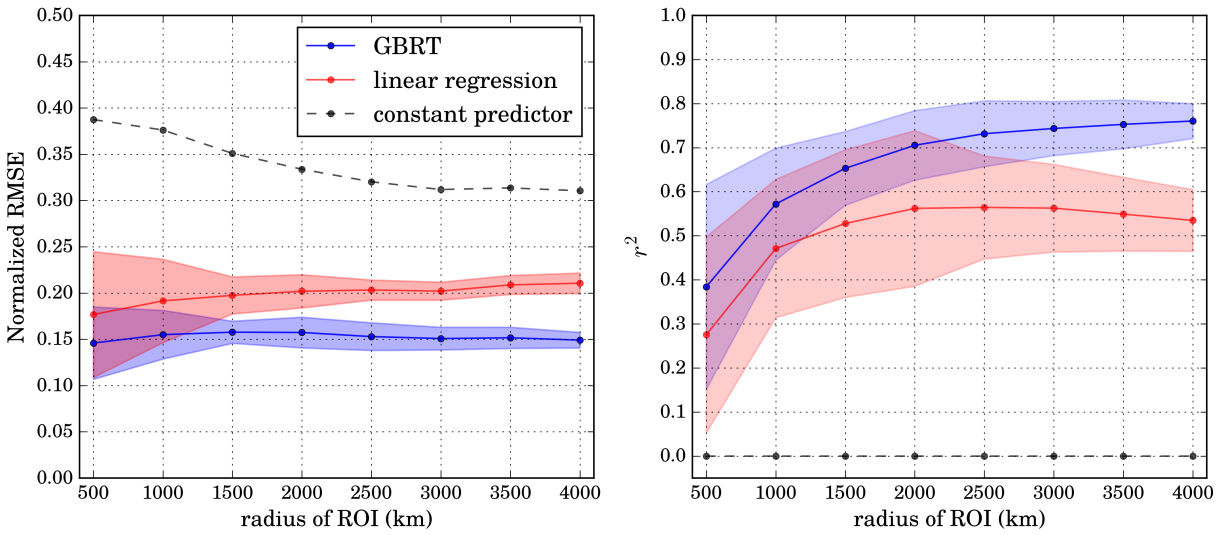

Figure A.3: Performance of GBRT (solid blue lines), linear regression (solid red lines), and constant predictor (dashed black lines) for different values of ROI radius. For each radius the three models are evaluated using the cross validation procedure described in text on 50 randomly chosen ROIs with $\rho_{ROI} = 11.3 \times 10^{-6}$ km^{-2}. Two measures of error are reported for each model and each radius: normalized RMSE (left) and r^2 of linear correlation between GHF and $\widehat{GHF}$ (right), both averaged over the 50 ROIs. As ROI radius increases linear regression predictions deteriorate in quality as indicated by higher normalized RMSE values (left) and smaller values of r^2 (right). In contrast, GBRT predictions maintain their normalized RMSE (left) and show increasing linear correlation with true GHF values (right). The blue and red regions show the standard deviation of the 50 ROIs for GBRT and linear regression, respectively.

A.2.2 Evaluation of Stability

Due to uncertainties associated with GHF inferences in Greenland, we investigate the stability of GBRT by assessing the sensitivity of its predictions when increasingly large perturbations are applied to GHF values in the training stage. We repeat a similar procedure as described above but with the addition of random noise to training GHF values. Here, we fix the parameter values $R = 1300$ km and ρ_{ROI}=11.3 $\times 10^{-6}$km^{-2} (corresponding to Greenland ROI values). We then consider $N = 50$ randomly chosen ROI centers and for each center train the model by adding increasing amounts of random noise η to GHF values. The noise signal is zero-mean Gaussian with varying standard deviation (and hence varying mean absolute value). The *relative noise amplitude*

$0 \leq A \leq 1$ is defined to be:

$$A = \frac{\mathbb{E}[|\eta|]}{\langle y_k^{(t)} \rangle}$$

where the numerator is the expected absolute value of Gaussian noise signal η and the denominator is the average value of y in the training set T (the extreme case $A = 0$ corresponds to unperturbed training data). For each value of A, the standard deviation of the zero-mean Gaussian noise is set such that the mean absolute value of noise $\mathbb{E}[\eta|]$ takes the required value of $A\langle y_k^{(t)} \rangle$:

$$\text{Var}[\eta] = \frac{\pi(A\langle y_k^{(t)} \rangle)^2}{2}$$

To quantify the effect of noise a baseline predictor f_0 is obtained from noise-free training data, namely with $A = 0$. Then, for each relative noise amplitude value A a predictor f_A is obtained from proportionally noisy data:

$$T_A = \left\{ \left(\mathbf{x}_k^{(t)}, y_k^{(t)} + \eta_k \right) \right\}_{k=1}^{n-m}$$

where:

$$\eta_k \sim \mathcal{N}\left(0, \frac{\pi(A\langle y_k^{(t)} \rangle)^2}{2}\right)$$

The noise-induced perturbation in predictions for each ROI is measured through the normalized root mean square difference between f_0 and f_A:

$$\frac{1}{\langle y_k^{(v)} \rangle_k} \sqrt{\left\langle \left| f_A\left(\mathbf{x}_k^{(v)}\right) - f_0\left(\mathbf{x}_k^{(v)}\right) \right|^2 \right\rangle_k}$$

which is then averaged over all N ROIs (Figure A.4).

Our analysis clearly demonstrate that GBRT is a stable model in the sense that small perturbations in training GHF values do not lead to large perturbations or 'blow-ups' in GHF predictions (Figure A.4).

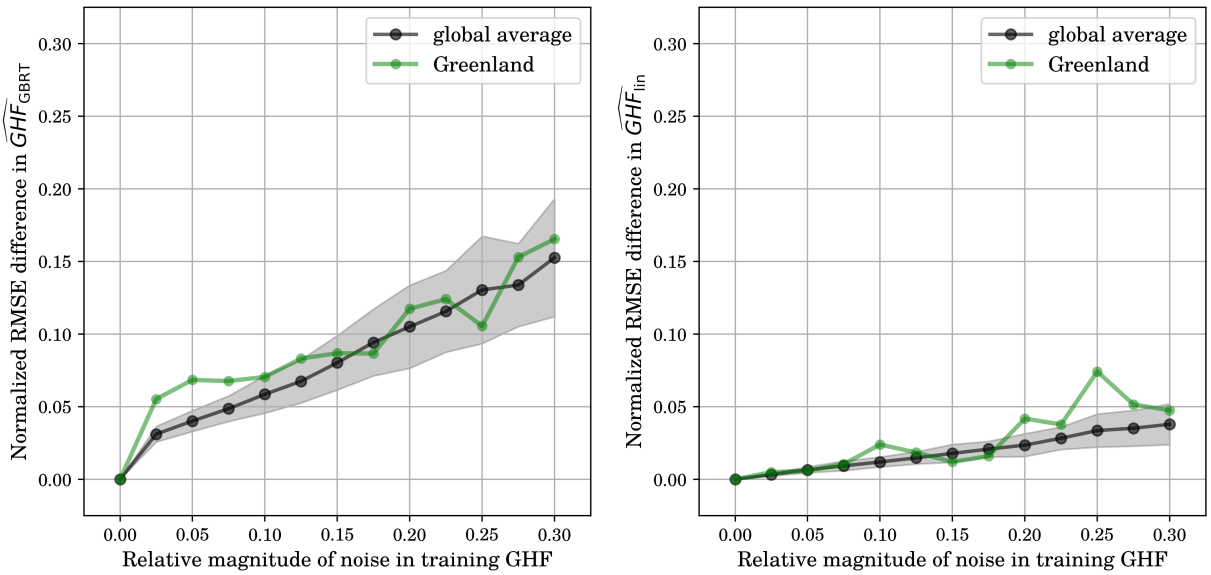

Figure A.4: Sensitivity of GBRT (left) and linear regression (right) to perturbations in training GHF. For each ROI, Gaussian noise signals with increasing variance (and hence increasing mean absolute value) are added to training GHF values and the resulting GHF predictions are compared to noise-free GHF predictions on validation samples. Relative magnitude of noise is proportional to the standard deviation as well as the mean absolute value of the applied Gaussian noise. This procedure is repeated for 50 randomly chosen ROIs (thin grey lines) with radius 1300 km and $\rho_{ROI} = 11.3 \times 10^{-6}$ km^{-2}, averaged over ROIs (black line), and repeated for Greenland (green line). This plot demonstrates the stability of GBRT predictions from noisy training data; namely, that perturbations in training GHF lead to comparable, or smaller, perturbations in predicted GHF.

A.3 Interpretation and Feature Importances

A natural question in interpreting predictive statistical models is whether it is possible to gain an understanding of those features on which variations in GHF depends the most as well as the nature of these dependencies. Also, a geologic interpretation may require reducing the large number of features to a smaller subset of features that can predict the GHF with similar accuracy of what is already obtained. Alternatively, one might merely wish to assign a measure of relative importance in the predictions to each feature. The extent to which one can progress in either approach is generally limited by three issues. First, the number of subsets of features to be evaluated as candidates for 'influential features' grows exponentially with the number of features. This poses a prohibitively demanding computational task unless the model is simple enough (e.g. linear regression) such that

contributions of different features are readily decomposable. Second, when using any statistical model, linear or not, one is prone to misinterpreting the relevance of subsets of features with latent (or hidden) correlations among themselves. Finally, although the relevance of each feature can be gauged through some variation of the amount of variance it explains, these measures are more difficult to interpret in additive models like GBRT since such models are essentially averages of simpler predictors (e.g. GBRT predictions are averages across predictions of individual regression trees).

A.3.1 Relative feature importances

At each partitioning step while training a single regression tree, the contribution of the chosen feature to the reduction in loss is $e^2(D,k,T)$ (see line 3 of Algorithm 1). One can thus define a measure of importance I_k for feature k in tree j defined as the sum of all reductions in error provided by feature k:

$$I_k^2(f_j) = \sum_{D,k,T} e^2(D,k,T)$$

where the sum is over all internal nodes D of tree f_j that partition over x_k with threshold T. This, when summed over all trees f_j and normalized such that $\sum_k I_k = 1$, is refered to as the *relative feature importance* vector for GBRT (Friedman et al. (2001, section 10.13) and Friedman (2001, section 8))

$$\overline{I_k^2} = \frac{\langle I_k^2 \rangle}{\sum_k \langle I_k^2 \rangle},$$

where the averages are over j indexing individual trees f_j. This is exactly what is plotted in Figure A.5.

A.3.2 Further work

One technique that is more robust to potentially hidden correlations among features is to view partial dependence or conditional expectation plots of the predicted variable, here the GHF, against feature subsets of interest (Friedman, 2001; Goldstein et al., 2015). The partial dependence of GHF

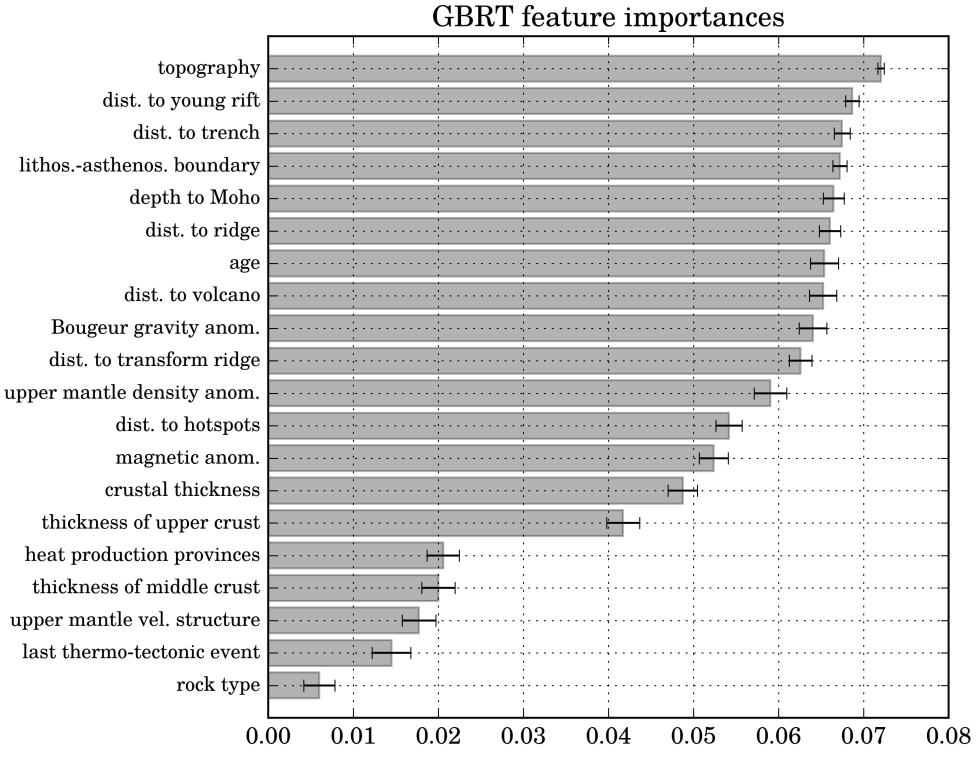

Figure A.5: Relative importance of different features in the trained GHF prediction model, averaged over 50 random ROI with radius 1300 km and $\rho_{ROI} = 11.3$ per 10^6 km^2. The importance of each feature in each ROI is the average reduction in prediction error over all regression trees provided by that feature (see section 3.1 of Supplementary Material for details). All values above are normalized such that the sum of relative importances is 1 and error bars show the standard deviation across the 50 ROIs.

on a single feature is a function (and not merely a single number) that shows for each value of the feature of interest the average value of GHF over all values of all other features. Partial dependence of the GHF on all subsets of size k can uncover interactions of order at most k among the features (Friedman, 2001). However, partial dependences can only be visually examined for prohibitively small subsets of features.

Alternatively, one can limit the exponentially large number of feature subsets by a greedy heuristic known as recursive feature elimination where in each round the least important feature (according to the relative importances described above) is excluded and the model is retrained using the remaining subsets until a small number of predictive features remain (Guyon et al., 2002).

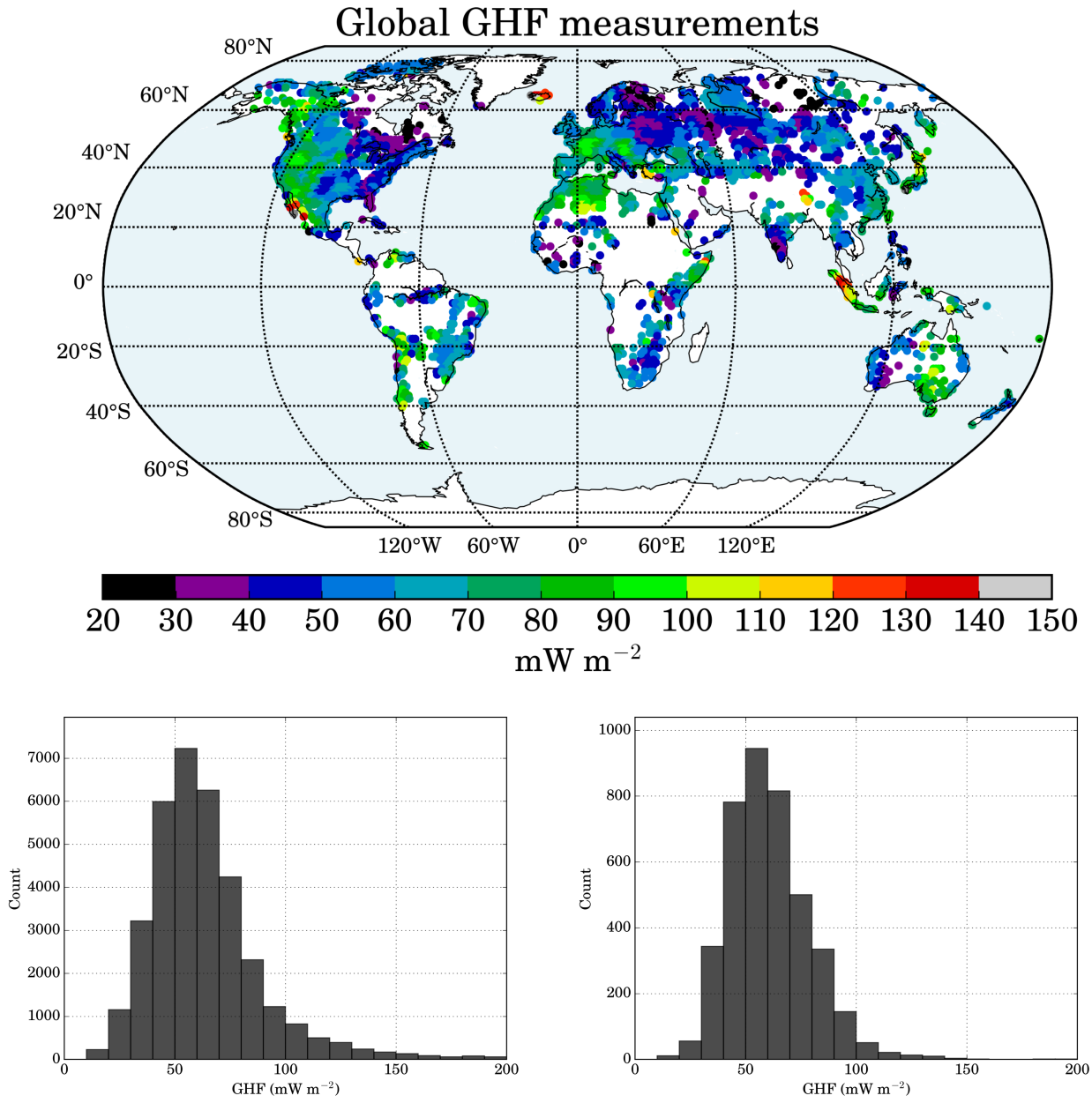

Figure A.6: Spatial distribution of global GHF point measurements (top map) averaged in 1 degree latitude-longitude cells. The corresponding histogram is shown in bottom right and the histogram of all the GHF measurements before averaging is shown the bottom left.

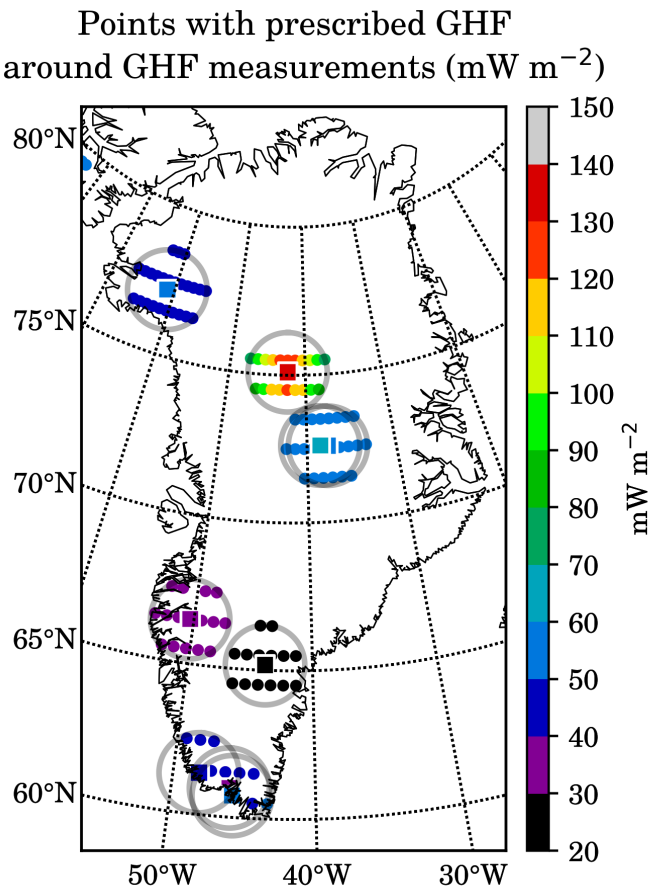

Figure A.7: Location and magnitude of the prescribed GHF values in Greenland that are included in the training set. The circles contain the points within 150 km away from GHF measurements whose GHF are prescribed with the Gaussian distribution around ice core measurements.

A.4 Data

A.4.1 Distribution of global GHF measurements

The 35,000 points measurements of GHF on the continents are averaged into 1 by 1 degree latitude-longitude cells. A low-pass filter is applied to the data to remove the short-scale spatial variability of data. Figure A.6 shows the spatial distribution of smoothed points, as well as histograms before and after the averaging and smoothing are applied.

Table A.1: GHF measurements or inferences in Greenland. The location of the GAP Project is visually chosen from georeferencing Meierbachtol et al. (2015, Fig. 1). and the average value of 31 mW m^{-2} is used. Superscripts *i* and *b* denote ice-core and borehole measurements, respectively.

Borehole Name	Latitude (°N)	Longitude (°W)	GHF (mW m^{-2})	Reference
[i]GRIP	72.58	-37.64	51.3	Dahl-Jensen et al. (1998)
[i]GISP2	72.60	-38.50	60	Petrunin et al. (2013)
[i]NorthGRIP	75.10	-42.32	90 & 135 & 160	Dahl-Jensen et al. (2003); Greve (2005)
[i]Dye 3	65.18	-43.82	20	Greve (2005)
[i]Camp Century	77.18	-61.13	50	Greve (2005)
[b]SASS1	61.40	-48.16	43	Sass et al. (1972)
[b]SASS2	60.98	-45.98	32	Sass et al. (1972)
[b]Langseth	60.73	-45.75	51	Langseth et al. (1972)
[b]GAP Project[1]	66.50	-50.33	34.8 & 27.2	Meierbachtol et al. (2015); Harper et al. (2011)

A.4.2 Available GHF measurements in Greenland

In total 9 measurements of GHF are available in Greenland that are listed in Table S1. The map of the measurements and the additional points added with the Gaussian kernel around the points is shown in Figure A.7.

A.4.3 Rock type conversions

Table S2 shows the conversion of global lithology map to rock-type. Hartmann & Moosdorf (2012) do not include rock type of Greenland bedrock, therefore we use the map of geologic provinces of Dawes (2009), modified by Dyke et al. (2014) to identify the rock-types in Greenland. We use GEUS geologic map of the coasts of Greenland (Henriksen et al., 2009) to interpret the rock-types associated with Dawes (2009) geologic provinces (Table S3).

The geologic basins from Dawes (2009) do not indicate the general rock type. Therefore, we generalized the rock types by assigning the similar rock type provided in maps of exposed coastal rocks provided by GEUS (Henriksen et al., 2009).

Table A.2: Conversion of Hartmann & Moosdorf (2012) lithology to general rock type

Hartmann & Moosdorf (2012) lithology	Rock type
Unconsolidated Sediments (SU)	Sedimentary
Siliciclastic Sedimentary Rocks (SS)	Sedimentary
Mixed Sedimentary Rocks (SM)	Sedimentary
Carbonate Sedimentary Rocks (SC)	Sedimentary
Pyroclastics (PY)	Volcanic
Evaporites (EV)	Sedimentary
Metamorphic Rocks (MT)	Metamorphic
Acid Plutonic Rocks (PA)	Volcanic
Intermediate Plutonic Rocks (PI)	Volcanic
Basic Plutonic Rocks (PB)	Volcanic
Acid Volcanic Rocks (VA)	Volcanic
Intermediate Volcanic Rocks (VI)	Volcanic
Basic Volcanic Rocks (VB)	Volcanic

Table A.3: Conversion of Dawes (2009) suggested Greenland geologic provinces, modified by Dyke et al. (2014), to general rock type.

Dawes (2009) geologic provinces	Rock type
Caledonian Belt	Metamorphic
Cambrian to Silurian Basins	Sedimentary
Devonian to Paelogene Basins	Sedimentary
Ellesmerian Fold Belt	Sedimentary
Ketilidian Ellesmere Inglefied Paleoproterozoic	Volcanic
North Atlantic Craton	Metamorphic
Paleogene Volcanics	Volcanic
Proterozoic Basins	Sedimentary
Proterozoic Mobile Belts	Metamorphic
Victoria Melville Archaean	Metamorphic